Single-Molecule Detection in Electrochemical Nanogap Devices

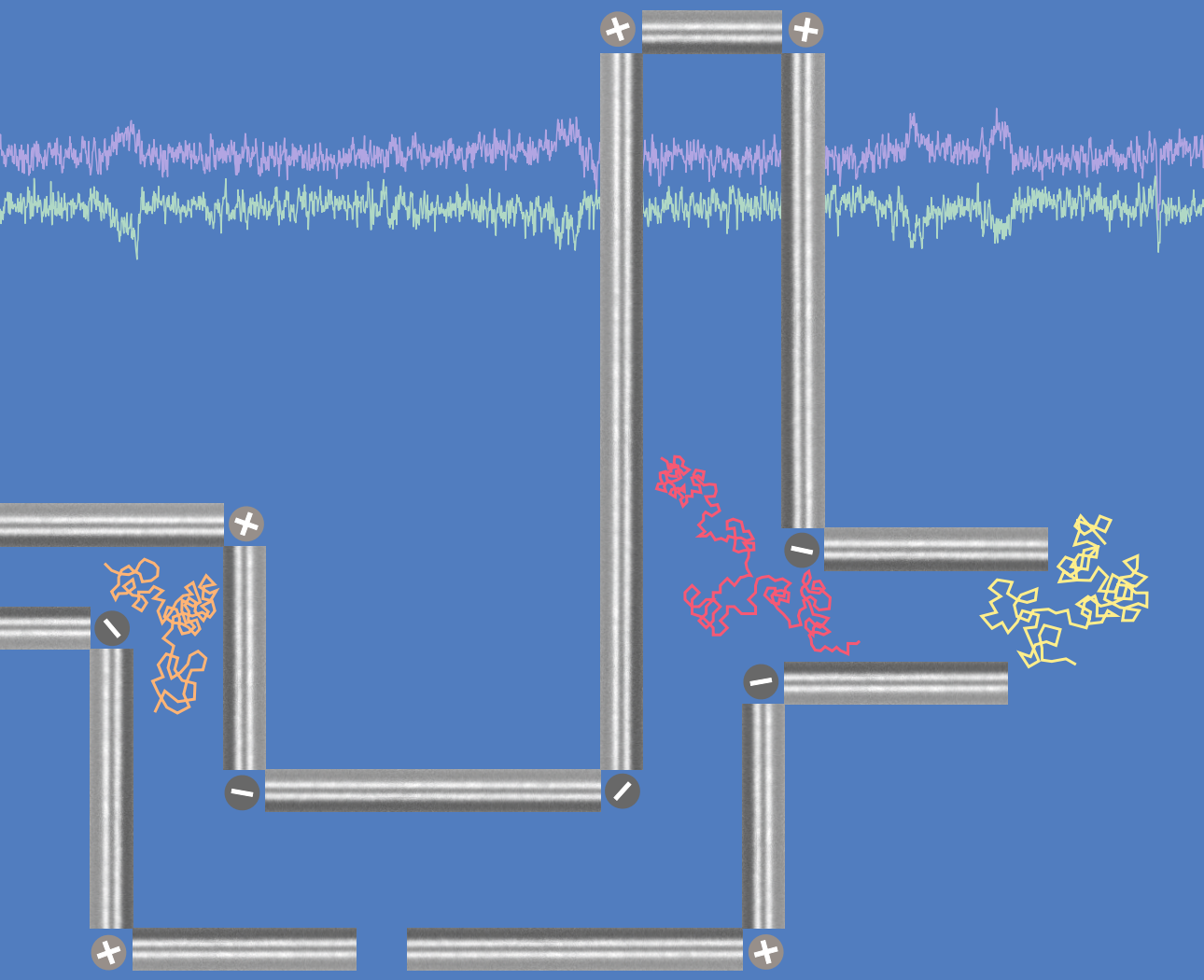

Shuo Kang

Single-Molecule Detection in Electrochemical Nanogap Devices

Shuo Kang

The graduation committee consists of:

Chairman:	Prof. dr. G. van der Steenhoven	University of Twente
Secretary:	Prof. dr. G. van der Steenhoven	University of Twente
Promotor:	Prof. dr. S. G. Lemay	University of Twente
Members:	Dr. ir. H. V. Jansen	University of Twente
	Prof. dr. ir. J. C. T. Eijkel	University of Twente
	Prof. dr. D. A. M. Vanmaekelbergh	University of Utrecht
	Dr. O. H. Elibol	Intel Corporation
	Prof. dr. B. Wolfrum	RWTH Aachen University
		Forschungszentrum Jülich

This research was supported by Nederlandse Organisatie voor Wetenschappelijk Onderzoek (NWO) and carried out at the Nanoionics group, MESA+ Institute for Nanotechnology, University of Twente, The Netherlands.

Title: Single-Molecule Detection in Electrochemical Nanogap Devices

Author: Shuo Kang

ISBN: 978-90-365-3636-3

SINGLE-MOLECULE DETECTION IN ELECTROCHEMICAL NANOGAP DEVICES

PROEFSCHRIFT

ter verkrijging van

de graad van doctor aan de Universiteit Twente

op gezag van de rector magnificus

prof. dr. H. Brinksma

volgens besluit van het College voor Promoties

in het openbaar te verdedigen

op vrijdag 28 maart 2014 om 16.45 uur

door

Shuo Kang

geboren op 30 juli 1983

te Changchun, China

This dissertation is approved by:

Prof. dr. Serge G. Lemay (promotor)

Contents

Chapter 1

Introduction

This chapter presents a short, general introduction to single-molecule techniques, including the motivations for measuring individual molecules and an overview of several popular approaches including optical methods, force microscopy and electrical methods. Single-molecule detection based on electrochemical methods in general and nanogaps in particular are also briefly reviewed. In addition an introduction to the reversible adsorption of redox species is included as it is a recurring theme throughout this thesis.

1.1 Single-molecule detection

Single-molecule measurements can provide information that is unobtainable with ensemble measurements, such as molecular-scale heterogeneities that are averaged out by measurements over a large sample population. For example, enzyme molecules with identical primary sequences exhibit slight differences in conformation and turnover rate. This can be due to random errors taking place in the transcription and translation processes, but it can also result from the vagaries of the folding process. That is, not all the enzymes of the same type are perfectly identical, yet in a measurement such as X-ray diffraction or mass spectrometry one merely gets an averaged result with a converged spectrum. On the other hand, it has become possible to track the positions and distributions of single particles in dynamic samples at high spatial and temporal resolutions,[1] which have permitted understanding the underlying functioning mechanisms of several biomolecular systems in detail.[2] From a sensor application point of view, single-molecule resolution is the fundamental limit for detection: such sensitivity allows low-concentration assays relevant for, e.g., early stage diagnostics. Since the first single-molecule measurement demonstrated in 1961 by Rotman,[3] who sprayed a solution containing the enzyme β-galactosidase and a fluorogenic substrate over a silicone oil preparation to create droplets in oil and observed individual enzyme molecules through fluorescence, single-molecule studies were reported with an exponentially increasing frequency[4] using widely varying techniques based on different operation principles.

Optical methods have probably become the most mature approach for single-molecule detection,[5–9] even though they usually require the target molecules to be labelled. The label most commonly takes the form of a fluorescent dye molecule[10] or a quantum dot[11] that absorbs and re-emits photons efficiently so that a higher signal is obtained compared to relying on the intrinsic optical properties of the analyte molecule. Figure 1.1 a demonstrates a real-time single-molecule DNA sequencing technique based on labeling deoxyribonucleoside triphosphates (dNTPs) with four distinguishable fluorescent dies.[12] Alternatively, an enzyme can be used to amplify the signal which generates many copies of a detectable product from a target analyte, or that can replicate the analyte itself. For example, using the polymerase chain reaction (PCR) to duplicate single nucleic acid molecules has been applied in many detection schemes.[13, 14]

Force microscopy, in which forces are measured when a long (bio)polymer is extended between two attachment sites, has also developed rapidly.[6, 15] This category of techniques includes tools such as optical tweezers,[16] magnetic tweezers,[17] and atomic force microscopy (AFM).[18] Optical tweezers manipulate a bead attached to a polymer molecule using the dielectric forces exerted by a laser beam focused on the bead. The restoring force on the bead is proportional to its displacement from its equilibrium position. Figure 1.1 b shows the schematic of an

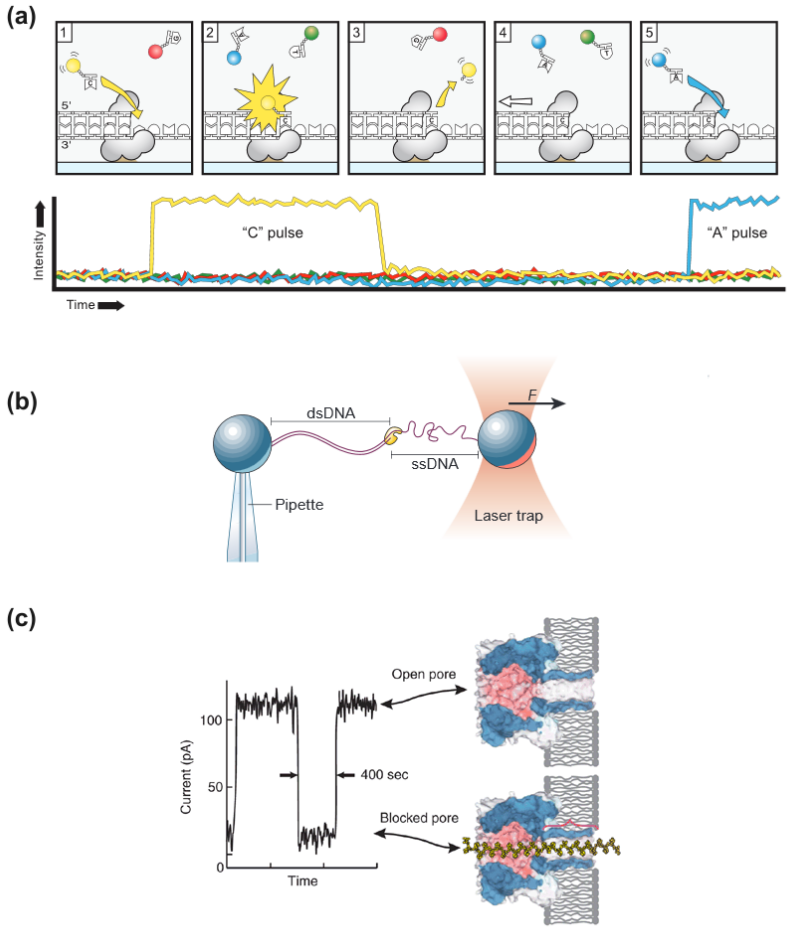

Figure 1.1: (a) Schematics of real-time DNA sequencing from single polymerase molecules using four distinguishable fluorescently labeled deoxyribonucleoside triphosphates (dNTPs). When a phospholinked nucleotide forms a cognate association with the template in the polymerase active site, an elevation of the fluorescence output on the corresponding color channel could be detected. Adapted with permission from American Association for the Advancement of Science: Turner *et al.*, *Science*, 2009, *323*, 133-138. (b) A DNA molecule is stretched between beads held in a micropipette and a force-measuring optical trap. The measured extension is the sum of contributions from the single-stranded DNA (ssDNA) and double-stranded DNA (dsDNA) segments. Reprinted by permission from Macmillan Publishers Ltd: Wuite *et al.*, *Nature*, 2000, *404*, 103-106, Copyright 2000. (c) Detection based on ionic current blockage through a nanopore. A typical trace of the ionic current amplitude (left) through an α-hemolysin pore clearly differentiates between an open pore (top right) and one blocked by a strand of DNA. Reprinted with permission from Macmillan Publishers Ltd: Branton *et al.*, *Nat. Biotechnol.*, 2008, *26*, 1146-1153, Copyright 2008.

experimental setup that employed this technique to investigate the effect of template tension on a DNA polymerase activity.[19] In magnetic tweezers, a superparamagnetic bead attached to the polymer is instead controlled by a magnetic force exerted by an externally imposed magnetic field gradient. In AFM, molecules are attached to the tip of a cantilever that can function both as a scanning probe and as a force transducer.

Electrical methods have been used to detect the passage of single molecules through a single ion channel[20] or nanopore[21, 22] by measuring the change in conductance of the electrolyte media. The conductance is decreased by blockage of the channel or the pore, as illustrated in Figure 1.1 c. The magnitude of the decrease is related to the molecule's size, while the duration of the decrease is related to the translocation speed of the molecule. Nanopores have been proposed as a potential enabling technology for next-generation DNA sequencing.[23] Both biological pores formed by protein channels embedded in lipid bilayer membranes or nanometre-sized apertures fabricated in thin-film membranes have been demonstrated.[24–26] Another electrical transduction mechanism is field-effect detection such as is used in ion-sensitive field-effect transistors (ISFET).[27] This approach has so far had little applicability at the single-molecule level, however.

1.2 Electrochemical detection of single molecules

Electrochemical single-molecule detection based on redox cycling was first claimed by Fan and Bard.[28, 29] A nanogap formed by approaching a wax-shrouded Pt-Ir tip to within ∼10 nm of a conductive substrate was employed, as shown in Figure 1.2 a. At redox-cycling potentials and analyte concentrations where device occupancy was of order unity, large relative fluctuations having a step-like character were observed, which were interpreted as being caused by individual molecules stepping in and out of the detection region.

Devices for single-molecule detection with a similar configuration were reported by Sun and Mirkin in an independent work.[30] Here solution was trapped in a nanogap that was formed by placing a disk-like recessed Pt nanoelectrode shrouded in glass into a Hg bath, as shown in Figure 1.2 b. Large variations of the diffusion-limited current during cyclic voltammetry were observed at concentrations corresponding approximately to single-molecule occupation of the device, and these variations were attributed to different numbers of redox molecules being trapped in the detection volume.

A rather different concept for single-molecule detection was presented in works studying the current passing through a molecular junction between a STM tip and a conducting planar surface,[31–33] as demonstrated in Figure 1.2 c. Under the conditions that the bridge molecule is redox active and the formal oxidation-reduction potential of its redox moiety lies near or between the potentials of the

electrodes, electrons start to hop from one electrode onto the molecule and reside in one of its well-defined electronic states for some time before finally hopping to the second electrode. This corresponds to the bridge molecule being reduced by the first electrode and subsequently oxidized by the second electrode.

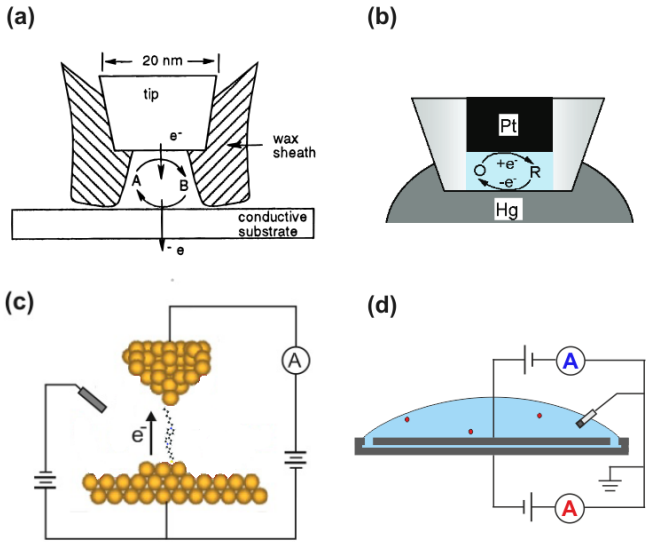

Figure 1.2: (a) Electrochemical single-molecule detection with a nanoelectrode encased in wax and positioned near a metallic surface. Reprinted with permission from Fan and Bard, *J. Am. Chem. Soc.*, 1996, *118*, 9669-9675. Copyright 1996 American Chemical Society. (b) Recessed glass-encased nanoelectrode immersed in mercury for single-molecule detection. Reprinted with permission from Sun *et al.*, *J. Am. Chem. Soc.*, 2008, *130*, 8241-8250. Copyright 2008 American Chemical Society. (c) A redox-active tunneling junction formed between a Au STM tip and a Au surface. (d) Schematic of the nanogap device employed in the research introduced in this book.

1.3 Single-molecule detection in nanogaps

The term "nanogap" has been generally used to represent a nanometric gap formed by a pair of metal substrates for molecular detection. A variety of methods including micro/nanofabrication,[34] nanoparticles,[35] electromigration,[36] electroplating,[37] etc. have been demonstrated to create nanogap structures, and a corresponding range of detection mechanisms has been employed for ultra-sensitive detection experiments such as redox cycling, surface-enhanced Raman scattering (SERS),[38, 39] field-effect,[40] resistive[41] and capacitive sensing.[42]

In this book we demonstrate the use of microfabricated nanogaps to detect

individual molecules by redox cycling, as sketched in Figure 1.2 d. The device consists of two electrodes with a length in the range of 10 to 100 μm and a width of several microns embedded in the ceiling and floor of a nanofluidic channel with a height of ~50 nm. Redox molecules enter and exit the detection region between the two electrodes through entrance holes located at the two ends of the channel. We prove that this approach is capable of detecting individual molecular tags in aqueous solution with single-molecule resolution. Combined with the inherent advantage that this form of transducer can be integrated with microfluidics and microelectronics, this detecting scheme may enable cost-effective, massively parallel analysis and diagnostics platforms.

1.4 Adsorption

Non-specific adsorption of macromolecules is a well-known problem in sensitive molecular detection,[43] where non-specifically adsorbed molecules contribute a background offset to the detected signal and thus decrease the detection sensitivity. In particular, methods aimed at detecting single molecules can lose this capability due to adsorption.

Perhaps surprisingly, small outer-sphere redox molecules such as ferrocene derivatives are also found to reversibly adsorb to electrodes.[44, 45] Especially in miniaturized systems with high surface-to-volume ratio, adsorption can cause the performance of devices to deviate from ideality and can even dominate some device properties: for example, adsorption is one of the main factors reducing signal levels in single-molecule redox-cycling measurements.[46] However, reversible adsorption is a very complex process dependent on a variety of factors such as the electronic structure of the metal-solution interface, the nature of the supporting electrolyte and of the adsorbate, and in many cases the potential of the electrode. Better understanding of adsorption and effective methods to control it are needed, and some steps in this direction are included in this thesis.

1.5 Ouline of the thesis

This thesis reports single-molecule detection experiments and analysis based on microfabricated electrochemical nanogap devices. We begin with preliminary works to characterize and understand the behavior of the measurement system, including how redox couples with different diffusion coefficients and reversible adsorption of analyte species influence the response of the devices.

Chapter 2 reviews microfabricated electrochemical systems, including micro/nanoelectrodes, redox-cycling devices, as well as electrochemical sensors integrated with microfluidics and CMOS electronics.

Chapter 3 reports how the mass-transport-limited current generated in nanogaps is controlled by the diffusion coefficient of both the reduced and oxidized forms of the redox-active species and the redox state of molecules in the bulk solution outside the gap. This includes numerical, analytical and experimental results.

Chapter 4 shows that reversible adsorption of analyte molecules is the main factor limiting the response time of nanogap sensors, based on both experimental and theoretical studies.

Chapter 5 investigates reversible adsorption of outer-sphere analyte molecules at electrodes in nanogap devices for different redox molecules, anionic species and temperatures.

Chapter 6 demonstrates the single-molecule detection of three common redox mediators at physiological salt concentrations based on nanogaps fabricated in a self-aligned approach. This is the first report of single-molecule electrochemical detection in water in a nanofluidic device.

Chapter 7 reports the first study ever to characterize mass transport with single-molecule resolution based on an electrochemical method. The first-passage times of individual redox molecules is probed using nanogaps, and their statistical distribution is compared with analytical predictions.

References

[1] Schmidt, T., Schutz, G. J., Baumgartner, W., Gruber, H. J. and Schindler, H., Imaging of Single Molecule Diffusion, *PNAS*, **1996**, *93*, 2926-2929.

[2] Visscher, K., Schnitzer, M. J. and Block, S. M., Single Kinesin Molecules Studied with a Molecular Force Clamp, *Nature*, **1999**, *400*, 184-189.

[3] Rotman, B., Measurement of Activity of Single Molecules of Beta-D-Galactosidase, *PNAS*, **1964**, *47*, 1981-1991.

[4] Moerner, W. E., New Directions in Single-Molecule Imaging and Analysis, *PNAS*, **2007**, *104*, 12596-12602.

[5] Walt, D. R., Optical Methods for Single Molecule Detection and Analysis, *Anal. Chem.*, **2013**, *85*, 1258-1263.

[6] Walter, N. G., Huang, C. Y., Manzo, A. J. and Sobhy, M. A., Do-it-yourself Guide: How to Use the Modern Single-Molecule Toolkit, *Nat. Methods*, **2008**, *5*, 475-489.

[7] Roy, R.; Hohng, S. and Ha, T., A Practical Guide to Single-Molecule FRET, *Nat. Methods*, **2008**, *5*, 507-516.

[8] Nie, S. and Emory, S. R., Probing Single Molecules and Single Nanoparticles by Surface-Enhanced Raman Scattering, *Science*, **1997**, *275*, 1102-1106.

[9] Kneipp, K., and Kneipp, H., Single Molecule Raman Scattering, *Appl. Spectrosc.*, **2006**, *60*, 322A-334A.

[10] Weiss, S., Fluorescence Spectroscopy of Single Biomolecules, *Science*, **1999**, *283*, 1676-1683.

[11] Michalet, X., Pinaud, F. F., Bentolila, L. A., Tsay, J. M., Doose, S., Li, J. J., Sundaresan, G., Wu, A. M., Gambhir, S. S. and Weiss, S., Quantum Dots for Live Cells, *in vivo* Imaging, and Diagnostics, *Science*, **2005**, *307*, 538-544.

[12] Eid, J., Fehr, A., Gray, J. and *et al.*, Real-time DNA Sequencing from Single Polymerase Molecules, *Science*, **2009**, *323*, 133-138.

[13] Jarvius, J.; Melin, J., Goransson, J., Stenberg, J., Fredriksson, S., Gonzalez-Rey, C., Bertilsson, S. and Nilsson, M., Digital Quantification Using Amplified Single-Molecule Detection, *Nat. Methods*, **2006**, *3*, 725-727.

[14] Saiki, R. K., Gelfand, D. H., Stoffel, S., Scharf, S. J., Higuchi, R., Horn, G. T., Mullis, K. B. and Erlich, H. A., Primer-directed Enzymatic Amplification of DNA with a Thermostable DNA-Polymerase, *Science*, **1997**, *239*, 487-491.

[15] Neuman, K. C. and Nagy, A., Single-Molecule Force Spectroscopy: Optical Tweezers, Magnetic Tweezers and Atomic Force Microscopy, *Nat. Methods*, **2008**, *5*, 491-505.

[16] Moffitt, J. R., Chemla, Y. R., Smith, S. B. and Bustamante, C., Recent Advances in Optical Tweezers, *Annu. Rev. Biochem.*, **2008**, *77*, 205-228.

[17] Gosse, C. and Croquette, V., Magnetic Tweezers: Micromanipulation and Force Measurement at the Molecular Level, *Biophys. J.*, **2002**, *82*, 3314-3329.

[18] Rief, M., Oesterhelt, F., Heymann, B. and Gaub, H. E., Single Molecule Force Spectroscopy on Polysaccharides by Atomic Force Microscopy, *Science*, **1997**, *275*, 1295-1297.

[19] Wuite, G. J. L., Smith S. B., Young M., Keller D. and Bustamante, C., Single-molecule Studies of the Effect of Template Tension on T7 DNA Polymerase Activity, *Nature*, **2000**, *404*, 103-106.

[20] Bezrukov, S. M., Vodyanoy, I. and Parsegian, V. A., Counting Polymers Moving through a Single-ion Channel, *Nature*, **1994**, *370*, 279-281.

[21] Wang, H. and Branton, D., Nanopores with a Spark for Single-molecule Detection, *Nat. Biotechnol.*, **2001**, *19*, 622-623.

[22] Li, W., Bell, N. A. W., Hernandez-Ainsa, S., Thacker, V. V., Thackray, A. M., Bujdoso, R. and Keyser, U. F., Single Protein Molecule Detection by Glass Nanopores, *ACS Nano*, **2013**, *7*, 4129-4134.

[23] Branton, D., Deamer, D, W., and Marziali, A., The Potential and Challenges of Nanopore Sequencing, *Nat. Biotechnol.*, **2008**, *26*, 1146-1153.

[24] Soni, G. V. and Meller, A., Progress toward Ultrafast DNA Sequencing Using Solid-State Nanopores, *Clin. Chem.*, **2007**, *53*, 1996-2001.

[25] Healy, K., Nanopore-based Single-molecule DNA Analysis, *Nanomedicine-UK*, **2007**, *2*, 459-481.

[26] Howorka, S., Cheley, S. and Bayley, H., Sequence-specific Detection of Individual DNA Strands Using Engineered Nanopores, *Nat. Biotechnol.*, **2001**, *19*, 636-639.

[27] Schöning, M. J. and Poghossian, A., Recent Advances in Biologically Sensitive Field-effect Transistors(BioFETs), *Analyst*, **2002**, *127*, 1137-1151.

[28] Fan, F. R. F. and Bard, A. J., Electrochemical Detection of Single Molecules, *Science*, **1995**, *267*, 871-874.

[29] Fan, F. R., Kwak, J. and Bard, A. J., Single Molecule Electrochemistry, *J. Am. Chem. Soc.*, **1996**, *118*, 9669-9675.

[30] Sun, P. and Mirkin, M. V., Electrochemistry of Individual Molecules in Zeptoliter Volumes, *J. Am. Chem. Soc.*, **2008**, *130*, 8241-8250.

[31] Xu, B. Q. and Tao, N. J., Measurement of Single-molecule Resistance by Repeated Formation of Molecular Junctions, *Science*, **2003**, *301*, 1221-1223.

[32] Li, C., Pobelov, I., Wandlowski, T., Bagrets, A., Arnold, A.and Evers, F., Charge Transport in Single Au-Alkanedithiol-Au Junctions: Coordination Geometries and Conformational Degrees of Freedom, *J. Am. Chem. Soc.*, **2008**, *130*, 318-326.

[33] Pobelov, I. V., Li, Z. and Wandlowski, T., Electrolyte Gating in Redox-Active Tunneling Junctions - An Electrochemical STM Approach, *J. Am. Chem. Soc.*, **2008**, *130*, 16045-16054.

[34] Chen, X., Guo, Z., Yang, G. M., Li, J., Li, M. Q., Liu, J. H. and Huang, X. J., Electrical Nanogap Devices for Biosensing, *Mater. Today*, **2010**, *13*, 28-41.

[35] Lim, D. K., Jeon, K. S., Kim, H. M., Nam, J. M. and Suh, Y. D., Nanogap-engineerable Raman-active Nanodumbbells for Single-molecule Detection, *Nat. Mater.*, **2010**, *9*, 60-67.

[36] Park, H., Lim, A. K. L., Alivisatos, A. P., Park, J. and McEuen, P. L., Fabrication of Metallic Electrodes with Nanometer Separation by Electromigration, *Appl. Phys. Lett.*, **1999**, *75*, 301-303.

[37] Morpurgo, A. F., Marcus, C. M. and Robinson, D. B., Controlled Fabrication of Metallic Electrodes with Atomic Separation, *Appl. Phys. Lett.*, **1999**, *74*, 2084-2086.

[38] Natelson, D., Li, Y. J. and Herzog, J. B., Nanogap Structures: Combining Enhanced Raman Spectroscopy and Electronic Transport, *Phys. Chem. Chem. Phys.*, **2013**, *15*, 5262-5275.

[39] Cortés, E., Etchegoin, P. G., Le Ru, E. C., Fainstein, A., Vela, M. E. and Salvarezza, R. C., Monitoring the Electrochemistry of Single Molecules by Surface-Enhanced Raman Spectroscopy, *J. Am. Chem. Soc.*, **2010**, *132*, 18034-18037.

[40] Im, H. S., Huang, X. J., Gu, B. and Choi, Y. K., A Dielectric-modulated Field-effect Transistor for Biosensing, *Nat. Nanotechnol.*, **2007**, *2*, 430-434.

[41] Liang, X. G. and Chou, S. Y., Nanogap Detector inside Nanofluidic Channel for Fast Real-time Label-free DNA Analysis, *Nano. Lett.*, **2008**, *8*, 1472-1476.

[42] Yi, M. Q., Jeong, K. H. and Lee, L. P., Theoretical and Experimental Study Towards a Nanogap Dielectric Biosensor, *Biosens. Bioelectron.*, **2005**, *25*, 1320-1326.

[43] Roach, L. S., Song, H. and Ismagilov, R. F., Controlling Nonspecific Protein Adsorption in a Plug-based Microfluidic System by Controlling Interfacial Chemistry Using Fluorous-phase Surfactants, *Anal. Chem.*, **2005**, *77*, 785-796.

[44] Zevenbergen, M. A. G., Singh, P. S., Goluch, E. D., Wolfrum, B. L. and Lemay, S. G., Electrochemical Correlation Spectroscopy in Nanofluidic Cavities, *Anal. Chem.*, **2009**, *81*, 8203-8212.

[45] Singh, P. S.c Chan, H. S. M.c Kang, S. and Lemay, S. G., Stochastic Amperometric Fluctuations as a Probe for Dynamic Adsorption in Nanofluidic Electrochemical Systems, *J. Am. Chem. Soc.*, **2011**, *133*, 18289-18295.

[46] Kang, S., Nieuwenhuis, A. F., Mathwig, K., Mampallil, D. and Lemay, S. G., Electrochemical Single-molecule Detection in Aqueous Solution Using Self-aligned Nanogap Transducers, *ACS Nano*, **2013**, *7*, 10931-10937.

Chapter 2

Microfabricated Electrochemical Systems

This Chapter reviews the development of electrochemical measurement systems fabricated with micromachining technology. This set of techniques enables the down-scaling of the dimensions of experimental elements with high controllability and repeatability, and further provides the possibility of integrating detection electrodes, fluidic control and even integrated circuits onto a single chip to form a highly compact analytical platform. The chapter is organized in order of increasing complexity of device structures, starting with methods for the fabrication of individual electrodes and arrays, followed by more complex devices with further improved sensitivity and concluding with a discussion of electrochemical systems integrated with microfluidics and/or microelectronics.

The contents of this chapter are to be published by Taylor & Francis as chapter 16 in the book *Nanoelectrochemistry* edited by S. Amemiya and M. V. Mirkin.

2.1 Introduction

The terms *microfabrication* and *micromachining* represent a broad set of techniques for systematically creating solid-state structures on the micro- and nanometer scales. Primarily developed by the semiconductors industry as an enabler for cheaper and more complex microelectronics circuitry, the resulting capabilities have since been exploited throughout most other areas of science and technology. In particular, microfabrication, having first become a workhorse of solid-state physics research, has become increasingly common in a variety of "wet" fields ranging from biophysics and neuroscience to environmental sensing and bioanalytical applications. Lithographic approaches are particularly well matched to the demands of electroanalytical methods due to the latter's emphasis on solid-state electrodes, electrical signals, and a growing interest in micro- and nanoscale systems and processes.

Microfabrication techniques offer several broad benefits when compared to alternative methods for fabricating miniaturized electrochemical measurement systems:

- Harnessing the well-developed, systematic fabrication protocols developed in the context of microelectronics leads in principle to highly reproducible results for the size and geometry of nanostructures. This is notoriously difficult to achieve on the nanometer scale using alternative approaches based on more *ad hoc* protocols.

- This reproducibility in turn greatly facilitates characterization since a battery of tools can be brought to bear on a series of nominally identical structures, even when some of these tools are mutually exclusive and/or destructive to the structures. This is again in contrast to approaches where each (nanoscale) system is individually realized, and thus needs to be separately characterized; in these cases, electrochemical measurements themselves are often the only source of characterization available.

- Once a measurement system is developed, the marginal costs associated with large-scale production become relatively low. To fully appreciate the full extent of this point, note that standard CMOS technology allows integrating millions of functional components on a mass-produced chip at a cost of only a few dollars.

- For sufficiently complex geometries, there are often no alternative clever "tricks" available and brute-force lithography-based methods are the only option.

- Individual devices can be easily integrated with each other as well as with other electronic and/or fluid handling components. This is particularly relevant in the context of so-called lab-on-a-chip applications. At the extreme

limit of integration, a complete measurement system can be integrated on a single chip with a liquid sample as input and digital data as output.

Offsetting these benefits are several complications and limitations introduced by microfabrication:

- Specialized equipment is required which is not available in all laboratories. This is particularly true of the high-end lithography equipment employed in several common approaches for patterning thin-film materials at the submicron level.
- There are experimental issues to which widely accepted solutions have been developed in conventional systems, but that cannot easily be replicated in microfabricated devices. Probably the best example is the difficulty of polishing most microfabricated electrodes, a common procedure with macro- and ultramicroelectrodes.
- The extensive processing involved in microfabrication largely precludes working with advanced materials such as, for example, single crystals.

These limitations and some of the approaches that have been explored to mitigate them will be addressed further below in the context of specific examples.

We note that the development of microfabricated electrochemical systems over the last 30 years has largely progressed in an evolutionary rather than revolutionary manner. But whereas many of the basic motivations, principles and approaches have remained relatively unchanged, their realization has become increasingly sophisticated and their performance has continually improved as a result of new insights and more advanced fabrication methods. This is illustrated in Figure 2.1, which contrasts two setups – one early and one recent – for redox-cycling measurements. Figure 2.1 a shows a measurement cell based on microfabricated interdigitated electrodes (discussed further below in section 2.4.1). The critical dimension of the microfabricated structure, namely, the spacing between the electrodes, was 50 μm. Figure 2.1 b shows the corresponding arrangement for a recent nanofluidic thin-layer cell (discussed in section 2.4.3). Here the electrode spacing is 50 nm, leading to a thousand-fold increase in diffusive fluxes. Both cells allow for convective transport, with the caveat that this requires a more sophisticated polydimethylsiloxane (PDMS) microfluidic interface in the case of the nanodevice.

The present chapter focuses on summarizing the evolution and the current status of microfabrication-based approaches for the realization of electroanalytical systems. In keeping with the general theme of this book, we focus primarily on nanoscale systems where possible. In areas where little work has reached this level of miniaturization we instead discuss the state of the art at the micrometer scale. We assume that the reader has some familiarity with basic lithography-based fabrication methods and dwell only briefly on the general methods. For a more

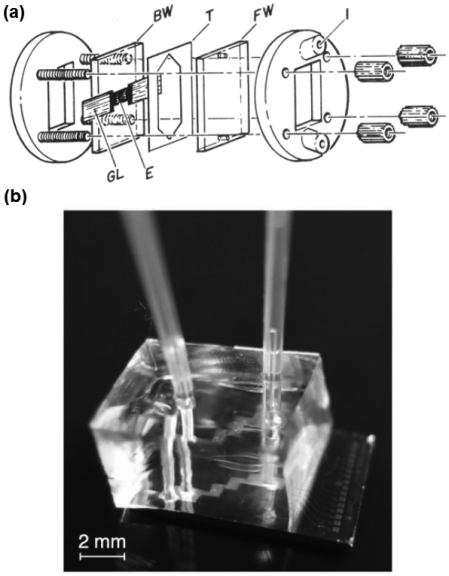

Figure 2.1: (a) Schematic drawing of assembly of interdigitated electrodes (E) microfabricated on a quartz substrate with electrical contacts (GL) and liquid chamber (T + BW + FW). BW, back window; FW, front window; GL, gold leaf contact, I, injection port; T, Teflon spacer. Adapted with permission from Sanderson *et al.*, *Anal. Chem.*, 1985, *57*, 2388-2393. Copyright 1985 American Chemical Society. (b) Photograph of a microfabricated electrochemical nanofluidic device; the contact pads and wires to individual electrodes are visible on the bottom right. Microfluidic channels molded in the transparent PDMS block allow delivering fluid to the electrochemical device. Reprinted from Mathwig *et al.*, *Micromachines*, 2013, *4*, 138-148.

general introduction we refer the uninitiated reader to a recent tutorial overview.[1] Here we instead concentrate on aspects of direct relevance to electrochemical methods or to the specific works being reviewed. The chapter is further organized in order of increasing complexity of the structures being discussed, starting with methods for the fabrication of individual electrodes and concluding with a brief discussion of systems in which electrochemical probes are fully integrated with microelectronics on the same chip.

2.2 Ultramicroelectrodes and ultramicroelectrode arrays

Ultramicroelectrodes (UMEs)[2, 3] offer several advantageous features compared to their macroscopic counterparts including a true steady-state diffusion-limited

current, small IR drops from solution resistance and short RC response times. Originally aimed at precise measurements of diffusion coefficients, interest in UMEs was further stoked by attempts at probing electroactive species inside brain tissue, which necessitated small, non-perturbing probes.[4, 5] Classical methods for fabricating UMEs were largely based on micrometer-diameter wires that were either selectively insulated or encased in glass micro-pipettes. These methods were used successfully in producing high-quality monolithic UMEs that were suitable for intra- and extra-cellular stimulation and recording;[6, 7] indeed, similar electrodes are still in use today. It however proved more challenging to employ these approaches to fabricate bundles of closely-spaced microelectrodes to monitor neural activity at a number of nearby sites simultaneously. In the 1970s, micromachining technology was thus introduced to fabricate arrays of (separately addressable) microelectrodes for both *in vitro* and *in vivo* experiments.[8–12] Arrays of identical UMEs connected in parallel can also be beneficial in other applications since faradaic currents at UMEs are relatively small: wiring many electrodes together amplifies the magnitude of the current while retaining the beneficial features of UMEs.[13]

An early work was presented by Thomas and co-workers,[8] who fabricated a miniature microelectrode array to monitor the bioelectric activity of cultured heart cells. A glass coverslip was used as a substrate on which a 200 nm thick nickel film was deposited and then defined by lithography. Afterwards gold was electroplated onto the nickel pads and a photoresist layer was coated and patterned to reveal only the gold electrodes. The remaining resist then functioned as a passivation layer. Finally a glass ring was affixed to the insulated array with bees' wax, creating a culture chamber, and platinum black was electrochemically deposited on the electrodes.

As an example of a miniaturized tool for *in vivo* neural recordings, a twenty-four channel microelectrode array fabricated based on thin-film technology was developed by Kuperstein and Whittington.[14] In this work Mo foil was used as a temporary substrate on which to build structures. KTFR photoresist, Au and another layer of KTFR resist were deposited and patterned in succession, thereafter the Mo foil was electrolytically etched away in an aqueous solution of 5% KOH, 5% $K_3Fe(CN)_6$, and 1% liquid Woolite (the latter atypical reagent playing the role of "low foaming, nonionic, water soluble, and alkali resistant surfactant compound"[15]). In this manner a probe consisting of arrays of Au recording sites sandwiched between two KTFR resist layers was generated, each of the recording site having an area of 120 μm^2 and being separated from neighboring sites by a gap of 85 μm. Finally platinum black was plated onto the recording sites of the probe.

During the same period, a multicathode polarographic oxygen electrode with several cathodes connected in parallel in a single package was demonstrated by Siu and Cobbold.[16] The device consisted of circular Au cathodes surrounded by a

continuous Ag/AgCl anode created with thin-film technology. Electrical contact between the anode and cathodes was maintained *via* a salt bridge formed by an electrolyte-containing membrane that covered the surface of the electrodes. The membrane also functioned as a protection layer to prevent the electrodes being contaminated in the meantime.

In the following decades microfabricated UMEs and UME arrays became increasingly widespread, as reviewed by Feeney and Kounaves.[17] An advantage of the added flexibility provided by micromachining started to be exploited by fashioning sets of electrodes from different materials. For example, Glass *et al.*[18] fabricated a multi-element microelectrode array for environmental monitoring including 66 working electrodes on a 2-inch silicon wafer with a variety of electrode materials including Pt, Au, V, Ir, and carbon deposited and defined by separate lithography steps. Different electrode materials displayed somewhat different responses to a given compound in voltammetric measurements, in principle increasing the selectivity compared with using a single electrode material.

In recent years designs for UMEs and UME arrays continue to evolve. For example, works based on microfabricated diamond UMEs and arrays are increasingly common, motivated by this material's attractive properties as an electrode that include mechanical stability, chemical inertness, low background currents, wide potential window and resistance to electrode fouling.[19] Individual electrodes fabricated with focused ion beam[20] and arrays fabricated with thin-film technology[21, 22] were demonstrated.

Instead exploiting the advantages of a high degree of integration, addressable electrode arrays with each sensing pixel wired via multiplexing circuitry to a potentiastat were developed for sensing and imaging.[23, 24] For instance, a multianalyte microelectrode detection platform capable of discriminating between multiple protein and DNA analytes simultaneously was demonstrated.[25] The electrodes were selectively functionalized with enzymes, antibodies, DNA and peptide probes using an electrically addressable deposition procedure.

A method for fabricating 3D electrode structures was demonstrated by Sanchez Molas *et al.*[26] to effectively extend the electrode surface area. In this case the motivation for creating such structures originated from biofilm-based microbial fuel cell applications. High-aspect-ratio micropillars were formed by micromachining a silicon wafer with deep reactive ion etching (DRIE), the radius of the pillars being 5 - 10 μm with a separation of 20-100 μm in between and a height of 5-125 μm. A multi-layer of Ti/Ni/Au was sputtered onto the structure surface to ensure the metallization of both the vertical walls and the bottom surface between the pillars.

2.3 Nanoelectrodes and nanoelectrode arrays

In recent years considerable attention has shifted to nanoscale electrodes and integrated systems.[27–30] With this further downscaling, the intrinsic advantages of UMEs such as small ohmic drops and fast response times are further amplified. Mass transport also becomes so efficient that even fast electrochemical reactions become increasingly limited by the rate of heterogeneous electron transfer, allowing ultrafast electron-transfer kinetics to be studied. Furthermore, because the electrode size becomes comparable to the thickness of the electrical double layer and to the size of macromolecular analytes, new mass-transport phenomena have been predicted and new analytical applications can be considered, respectively.[31]

The challenge of fabricating and characterizing nanometer-scale electrodes is however substantial compared to microelectrodes. In particular, the ability to project a sharp image of a small feature onto the substrate in photolithography is limited by the wavelength of the light that is used and the ability of the reduction lens system to capture enough diffraction orders from the illuminated mask.[32] Even though the most advanced optical immersion lithography tools currently allow features of ∼40 nm to be realized in integrated-circuits processing, the necessary equipment is very specialized and mostly targeted at semiconductors research and manufacturing. Most readily-accessible optical-lithography equipment in universities and research laboratories instead has a much more modest practical resolution of ∼1 μm. Consequently, a broad range of alternative approaches has been explored for micromachining nanoscale electrochemical systems. These include lithographic methods with higher resolution such as e-beam, nanoimprint and nanosphere lithography; electrode materials prepared by bottom-up approaches; and a number of one-of-a-kind solutions for creating specific structures.

2.3.1 Tip-based nanoelectrodes

The bulk of the approaches employed for pioneering studies of nanoelectrodes were evolved from methods for preparing UMEs and/or tips for scanning electrochemical microscopy (SECM).[33, 34] Broadly speaking, these methods rely on preparing sharp conducting wires or tips and covering all but the apex with an insulating material including wax,[35–37] polyimide,[38] electrophoretic paint[39–46] or glass.[47–53] Because the electrodes are prepared individually, these approaches have historically tended to exhibit limited reproducibility. This prompted some authors to explore micromachining-based approaches for fabricating tip-based electrodes.

Thiébaud *et al.*[54] developed tip-like electrodes based on a fully controlled lithographic process. Atomically faceted, 47 μm high tips were carved out of a ⟨100⟩ silicon wafer by anisotropic etching in KOH. The silicon was then suc-

cessively coated with thin films of silicon dioxide, platinum and silicon nitride. Following a final lithography step, the nitride was etched away from the apex of the tip to leave a Pt tip exposed with a height as small as 2 μm. In an alternative hybrid approach, Qiao *et al.*[55] first etched tungsten wires to yield tips with diameters below 100 nm and insulated these wires using electrophoretic paint. The focused ion beam (FIB) technique was then employed to selectively remove the insulating paint and sculpt the Pt tip apex to the desired shape. Tips with dimensions 100-1000 nm were realized in this manner.

Despite their potential benefits in terms of control and characterization, however, these approaches have not proven competitive compared to the more accessible classic approaches for fabricating tip electrodes.

2.3.2 Top-down fabrication of nanoelectrodes

Despite the limited resolution of optical lithography, this method has been employed to create nanoelectrodes by incorporating non-standard microfabrication steps. For example, Menke and co-workers[56] combined top-down lithography and electrodeposition to generate band electrodes with a width of 40-50 nm in a process coined lithographically patterned nanowire electrodeposition (LPNE). The process flow for the fabrication is shown in Figure 2.2. By under-cutting nickel bands which were covered with a layer of photoresist, a trench was formed and nanowires were grown by electrodeposition in the trench along the edge of the nickel bands. The height of the nanowires was determined by the thickness of the nickel bands and the width by controlling the deposition process. A hydrogen gas detector consisting of Pd nanowires fabricated using this method was demonstrated,[57] and the method was also improved by adding further processing steps to fabricate arrays of nanowires.[58] To overcome the restrictions imposed on the array density by the limited resolution of photolithography, repeated alternating deposition of nanowire electrodes and nickel bands was performed, the array being generated when all the nickel bands were simultaneously released in a subsequent step.

Another method for beating the resolution limitations of optical lithography was demonstrated by Heo and co-workers,[59] who derived a carbon linear nanoelectrode array from optical-lithography-defined polymer microstructures. Photosensitive polymer SU-8 was coated and patterned on a 6-inch passivated silicon wafer and subsequently pyrolyzed at 900 °C in vacuum. During the pyrolysis process, the SU-8 was carbonized and the dimension of the structures shrank by approximately 60% in width and 90% in height, as shown in the scanning electron microscope (SEM) images of Figure 2.3. The pyrolysis process was reported to be controllable such that the final dimensions of the carbon electrodes were predictable.

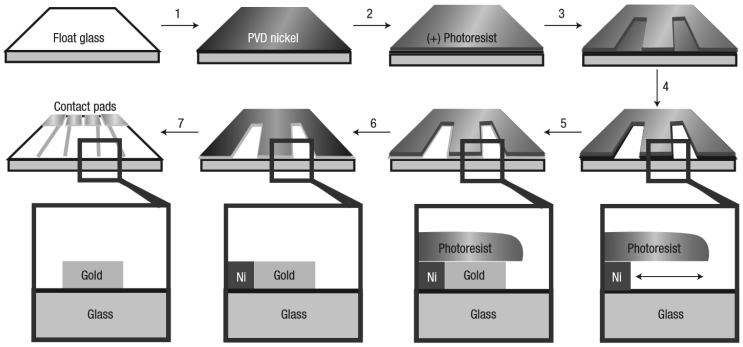

Figure 2.2: Process flow for lithographically patterned nanowire electro-deposition. Reprinted by permission from Macmillan Publishers Ltd.: Menke *et al.*, *Nat. Mater.*, 2006, *5*, 914-916. Copyright 2006 Nature Publishing Group.

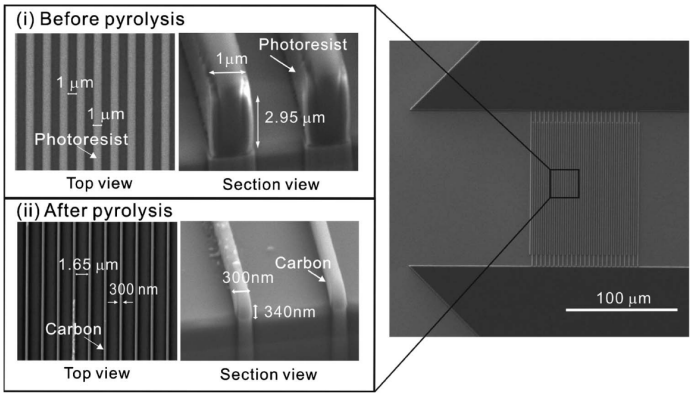

Figure 2.3: SEM images of nanoscale carbon electrodes pyrolized from SU-8 microstructures. Reproduced from Heo *et al.*, *J. Electrochem. Soc.*, 2011, *158*, J76-J80, by permission of The Electrochemical Society.

Despite these successes of optical-lithography-based approaches, patterning of nanoscale structures is more typically carried out using a workhorse of nanoscience and nanotechnology, electron-beam lithography (EBL). This tool, which was developed in the early 1970s,[60] employs a focused beam of electrons to write arbitrary two-dimensional patterns on a surface covered with an electron-sensitive resist. Apart from these differences, the whole range of thin-film technologies can be combined with EBL with only minor adjustments to the processes compared with optical lithography. It is a serial patterning technology rather than simultaneous patterning as in optical lithography, rendering the process more time-consuming and therefore costly, but this is compensated by the feature that

resolutions in the range 10-100 nm can be achieved with EBL, depending on the specific equipment employed.

A variety of nano-electrochemical systems fabricated with EBL has been demonstrated.[61–67] As an early example Niwa and co-workers[68] reported electrode arrays with sub-micron dimensions. Electrochemical analysis based on EBL-generated individual Au nanowires was reported by Dawson.[66] A catalytic signal from fewer than 50 enzyme molecules immobilized on an EBL-patterned nanoelectrode was also reported.[64]

Another technique used to pattern nanostructures from thin films is FIB milling, which operates in a fashion analogous to a scanning electron microscope (SEM) except that a finely focused beam of ions (usually gallium) is used instead of electrons. A FIB can be operated at low beam currents for imaging or high beam currents for site-specific sputtering or milling. A disadvantage is that this is also a serial method, individual structures needing to be prepared separately. One way to use FIB to generate electrodes is to first deposit a metal and an insulating layer, then drilling holes through the insulating layer to uncover the electrodes.[69–71] With this method recessed electrodes located at the bottom of truncated conical pores result.[69]

Alternatively, it is also possible to generate electrodes by first creating nanoscale holes through thin insulating membranes, then filling these holes from one side of the membrane with a conducting material to create electrode structures on the other side of the membrane. This approach is conceptually descended from earlier protocols to create nanoelectrode ensembles by depositing metal in a porous host membrane such as polycarbonate.[72] Besides FIB milling, a focused electron beam from a transmission electron microscope can also be used to drill individual nanopores.[73–76] An advantage of the latter approach is that a nanometer-resolution image of each nanopore can simultaneously be obtained. Since the diameter of the finished electrodes is dictated by that of the original pores, this provides an independent characterization of the electrode size. Krapf *et al.* demonstrated electrodes as small as 2 nm using this approach.[75]

High-throughput, high-resolution lithographic methods have also been developed. Nanoimprint lithography[77] creates patterns by mechanical deformation of a so-called imprint resist which typically consists of a monomer or polymer formulation cured by heat or UV light during the imprinting. A master stamp provides the pattern to be imprinted; while this stamp must first be created using another lithography method, it is not significantly degraded by the imprinting process and can be re-used over an extended period of time. A challenge of this technique is that the process is strongly dependent upon the pressure, temperature, time control, and even the geometry of the stamp. Nonetheless, electrode arrays created by nanoimprint lithography have been demonstrated and suggested for low-cost sensor production.[62, 78, 79]

Another, much simpler and low-cost alternative for fabricating electrodes is nanosphere lithography,[80–84] in which self-assembled monolayers of spheres are used as masks instead of selectively exposed polymer layers. For example, Valsesia *et al.*[81] spin-coated polystyrene beads with a diameter of 500-1000 nm onto a Au-coated substrate, forming a monolayer of hexagonally-packed beads whose surface coverage could be adjusted by tuning the spin-coating acceleration. With a treatment in oxygen plasma the size of the beads was reduced by half. Afterwards a layer of silicon oxide was deposited and lifted off by mechanically removing the beads in an ultrasonic bath. The resulting recessed Au spots with dimensions in the range of 50-120 nm and surrounded by silicon oxide were then used as templates to electrochemically grow polypyrrole nanopillars electrodes.

Diamond nanoelectrode ensembles and arrays were created by Hees *et al.*[83] using nanosphere lithography and EBL, respectively. In the first approach a substrate coated with a trimethylboron-doped nanocrystaline diamond (NCD) film was immersed in an ultrasonic bath with suspended SiO_2 spheres having a radius of 500 nm and a concentration of $\sim 10^{-7}$ cm^{-3}. The spheres adhered to the surface in a random pattern. An insulating NCD layer was then deposited onto the surface and lifted off by removing the SiO_2 beads with hydrofluoric acid (HF), creating recessed boron-doped diamond electrodes surrounded by an insulating NCD layer. The radius of the electrodes was about 175 nm and the average distance between them was 10 μm. In the second approach all the process steps were identical except that EBL-patterned plasma-enhanced chemical vapor deposition (PECVD) SiO_2 was used instead of SiO_2 beads for lifting off the passivation NCD film. Electrode arrays following regular hexagonal patterns were formed in this manner. SEM images of the electrodes and arrays fabricated with both methods are shown in Figure 2.4. Based on these arrays changes in electron-transfer rates were observed to change when switching the NCD surface termination from hydrogen to oxygen; this subtle effect was not observed based on macroscopic planar diamond electrodes.

2.3.3 Nanowire-based nanoelectrodes

In the approaches described so far, micro- and nanoscale electrodes were created by patterning thin conductive and/or insulating films into the desired geometry. An alternative bottom-up approach is to first synthesize electrode materials with nanoscopic dimensions, then to interface these materials to external interconnects to enable electrochemical measurements. Wire-shaped objects with nanometer-scale diameters and micrometer-scale lengths are particularly well suited for this approach: the long lengths make it relatively straightforward to pattern interconnects using relatively low-resolution lithography, while the small diameters mean that the materials effectively function as nanoscale band electrodes.[85]

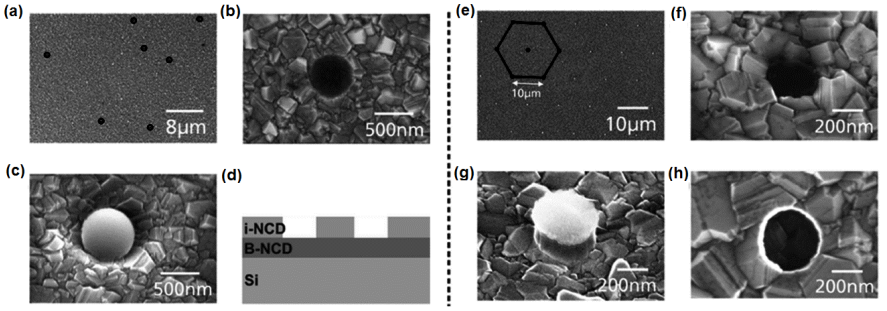

Figure 2.4: SEM images and schematic cross-section of diamond nanoelectrode ensembles fabricated with nanoshpere lithography (a-d) and arrays fabricated with electron-beam lithography (e-h). (a) Overview of randomly distributed electrodes. (b) SiO_2 sphere after deposition of insulating diamond. (c) Final boron-doped NCD electrode after removal of SiO_2. (d) Schematic cross-section of fabricated electrodes. (e) Overview of electrodes distributed in hexagonal pattern. (f) Structured SiO_2 island on boron-doped NCD layer. (g) Insulating diamond grown around SiO_2. (h) Final recessed diamond electrode. Adapted with permission from Hees *et al.*, *ACS Nano*, 2011, *5*, 3339-3346. Copyright 2011 American Chemical Society.

This approach is perhaps best illustrated by the use of single-wall carbon nanotubes (SWNTs) as electrode materials. SWNTs are cylindrically-shaped carbon macromolecules. They can be readily deposited on a substrate or, often preferably for device applications, grown by CVD from catalyst particles that can be deposited according to lithographically defined patterns on a solid substrate. The diameter and length distribution varies substantially depending on the growth method, but diameters of 1-3 nm and lengths of a few μm are typical and readily achievable. In a common approach, the nanotubes are first deposited or grown on the substrate, metal interconnects are added to make contact to one or more nanotube, and a passivation layer is deposited and patterned so as to cover the electrodes but leave (part of) the nanotubes exposed. Since the sidewalls are electrochemically active,[86] each individual nanotube functions as a band nanoelectrode. But because the geometry of the nanotube(s) and passivation can be controlled, a greater range of electrode geometries can also be created. In particular, Dumitrescu *et al.*[87, 88] showed that a relatively sparse network of randomly oriented, interconnected SWNTs can effectively function as a two-dimensional array of nanoelectrodes with overlapping diffusion fields: the total diffusion-limited current at a disk-shaped network electrode was shown to be equivalent to that to an UME of the same shape and size, but the current density at the surface of the SWNTs was much higher than at the corresponding UME. Alternatively, exposing only the sidewall of an individual SWNT leads to a near-ideal cylindrical electrode with a radius of $\sim$1 nm.[89] Finally, exposing only the end allows forming a point-like electrode with the same radius.[90] In cases where a different electrode material is needed, it was also shown that SWNTs can also be modified with

metal nanoparticles by electrodeposition. In these applications the SWNTs serve both as a template for deposition and as interconnects between the nanoparticles and external wiring. Paralleling the work on bare SWNTs, such deposition has been employed to create 2D (networks), 1D (wires) and 0D (single particles) nanoparticle electrodes.[90–92]

Similar approaches have been applied to a broad range of other 1D nanostructures. For example, Dawson *et al.*[93] demonstrated electrodes based on Au nanowires with a rectangular (∼210 nm × 250 nm) cross-section created by nanoskiving.[94] This method is based on first forming a block consisting of thick epoxy layers separated by a Au film. Thin slices of this block are then sectioned off in a plane perpendicular to the layers. Finally the epoxy is dissolved, leaving only Au nanowires available for contacting *via* lithographically defined external wires. Other examples of individual nanowires that have been investigated as electrochemical nanoelectrodes include multi-walled carbon nanotubes,[95] carbon nanofibers,[96] vanadium oxide nanowires and Si/amorphous-Si core/shell nanowires,[97] mesoporous ZnO nanofibers[98] and platinum nanowires prepared by laser pulling.[99]

2.3.4 Electrodes for electrochemical AFM

Another area where microfabricated electrodes have played a significant role is in the preparation of advanced scanning probes, in particular modified cantilevers for atomic force microscopy (AFM) with electrochemical functionality. In AFM, a sharp point mounted at the end of a flexible cantilever is scanned along a surface and the deflection of the cantilever or its resonance amplitude is used as feedback signal to control the height of the cantilever. Sub-nanometer resolution can be achieved in the height direction, while the lateral resolution is largely determined by the sharpness of the tip being employed; micromachining is commonly used for manufacturing sharp, reproducible cantilever and tip structures. Several authors have explored the possibility of modifying cantilevers to incorporate one or more electrodes in AFM tips.[100–104] In this way local electrochemical measurements can be performed while AFM feedback is employed for imaging and tip positioning.

As an early example, silicon nitride cantilevers were modified by patterning a ring electrode immediately around the apex of the AFM tip.[100, 101] This was achieved by coating the original silicon nitride cantilever with Au and an insulating silicon nitride layer, then milling the apex of the tip to create a sharp silicon nitride point (made from the original cantilever material) surrounded by a ring of exposed gold. The sharp nitride tip provides imaging capabilities and stability comparable to those of the original cantilever, while the ring electrode, contacted *via* the Au film, permits electrochemical measurements. In an alternative approach, Burt *et al.*[102] attached a metal nanowire to the end of an AFM tip. The wire, which was fabricated by coating a single-walled carbon nanotube

template, was insulated and then cut to create a Au disk nanoelectrode. This geometry results in a flat tip which reduces AFM resolution but has the benefit of allowing SECM measurements with simultaneous AFM imaging. More recent developments in this area include needle-shaped, individually addressable dual tips[103] and insulating diamond tips with integrated boron-doped diamonds electrodes.[104] In most approaches to AFM tip modification, the FIB technique has been the method of choice to precisely sculpt the complex geometry of the critical region near and at the apex of the tip.

2.4 Redox-cycling and generation-collection

In the micro- and nanoelectrode arrays discussed above, the motivation for creating a multi-electrode system is most often to amplify the faradaic current while retaining the beneficial properties of the individual miniature electrodes. The constituting electrodes thus function essentially independent of each other. Redox-cycling and generator-collector approaches instead exploit the interplay between redox reactions taking place at two or more electrodes. Establishing an effective coupling between electrodes requires careful control of electrode geometry and placement, a challenge that plays to the strengths of microfabrication techniques.

In generator-collector systems, the product of a reaction taking place at a generator electrode is detected at a second, so-called collector electrode. A natural figure of merit is the collection efficiency, which corresponds to the fraction of generated molecules that are collected. In redox cycling, both electrodes instead share both roles of generator and collector, as chemically reversible species are repeatedly reduced at one electrode and oxidized at the other. The geometries required for efficient redox cycling tend to be more restrictive than for generation-collection, since in this case the collection efficiency should be high for both halves of the cycle. A common figure of merit in redox cycling is the amplification factor, which essentially corresponds to the average number of times that each molecule is cycled before it exits the detection domain. Consistent with intuition, both the collection efficiency and the amplification factor tend to increase as the distance between the electrodes is reduced due to more effective mass transport.[3] Generator-collector and redox-cycling systems are thus natural candidates for miniaturization to the nanoscale.

At this time, three main classes of devices are undergoing the most extensive development toward nanoscale applications: interdigitated electrodes (IDEs),[59, 68, 105–111] recessed ring-disk (RRD) electrodes[84, 112–117] and nanogaps,[118–130] as summarized in Figure 2.5.

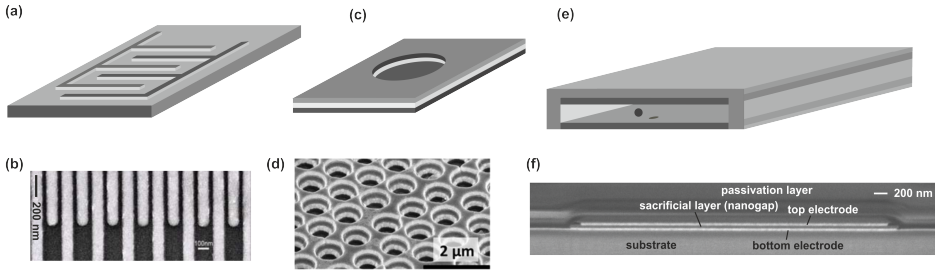

Figure 2.5: Schematic drawings (a, c, e) and scanning electron microscope images (b, d, f) of interdigitated electrodes, recessed ring-disk electrodes and nanogaps, respectively. (b) Top view of interdigitated electrodes, adapted from Ueno *et al.*, *Electrochem. Commun.*, 2005, *7*, 161–165, Copyright 2005, with permission from Elsevier. (d) View from an angle of a recessed ring-disk electrode array, adapted with permission from Ma *et al.*, *Anal. Chem.*, 2013, *85*, 9882–9888. Copyright 2013 American Chemical Society. (f) View from an angle of the cross-section of a nanogap, reprinted with permission from Kang *et al.*, *ACS Nano*, 2013, *7*, 10931–10937. Copyright 2013 American Chemical Society.

2.4.1 Interdigitated electrodes

The most widely reported redox-cycling device configuration, illustrated in Figure 2.5 a and 2.5 b, is the interdigitated electrode (IDE) or, equivalently, interdigited array (IDA).[59, 68, 105–111] It consists of two co-planar, interpenetrating comb-shaped electrodes. Because the two electrodes can be realized simultaneously by patterning a single layer of conducting material, this geometry is conceptually straightforward from a fabrication point of view. By the same token, the smallest achievable electrode spacing is set by the lateral resolution of the lithographic process employed. IDEs with electrode spacing ranging from microns down to tens of nanometers were correspondingly demonstrated using optical,[107, 131, 132] e-beam[61] and nanoimprint lithography.[78, 79] Amplification factors up to $\sim 10^2$ are typically reported with these structures.

In a pioneering article, Sanderson and Anderson[105] reported co-planar interdigitated electrodes fabricated by depositing and defining a layer of Au (1000-2000 Å) with 200-400 Å Cr as adhesion layer on a quartz substrate with photolithography and subsequent wet etching. Each electrode was 0.5 cm long and 50 μm wide, separated from the adjacent electrodes by a gap of 50 μm. Two strips of gold leaves were placed onto the metal pads to make electrical contacts. A liquid cell was formed by clamping the quartz substrate and a Teflon spacer between two quartz windows with quick-tightened screws, as indicated in the schematic drawing shown in Figure 2.1 a; amplification of the faradaic current by redox cycling was successfully observed in this system. Several years later, further downscaled electrode arrays with feature sizes ranging from 0.75 to 10 μm fabricated using both optical and electron-beam lithography were reported by Niwa and coworkers.[68] A layer of spin-on glass was coated onto wafers as passivation and the

electrodes and contact pads were uncovered by etching through this passivation layer using reactive ion etching (RIE).

Besides electrode spacing, the signal amplification provided by IDEs also depends on the width and the aspect ratio of the electrodes.[133] Electrodes with a relatively large height-to-width ratio were shown to generate a higher amplification factor than planar electrodes, as the short linear diffusion path created between the electrode side walls increases the diffusive flux. Dam and co-workers[108] reported intentionally vertically-faced IDEs. Trenches were first created by DRIE on a silicon wafer, after which the electrode material (Pt together with a Ti adhesion layer) was deposited onto the side walls of the trenches by evaporation under a 45° incident angle. While the minimum separation between the electrodes was only 2 μm, a relatively high amplification factor of 60-70 was nonetheless achieved with this device because of the advantageous three-dimensional geometry.

Another method introduced by Goluch *et al.*,[109] for achieving higher amplification factors is to encase an IDE inside a fluidic channel, thus minimizing the loss of analyte molecules to the bulk solution above the IDE and increasing the average number of cycles undergone per molecule. Calculations indicate that the increase becomes most pronounced once the height of the channel becomes comparable to or smaller than the lateral electrode finger spacing. By embedding an IDE with a finger spacing of 250 nm in a series of parallel, 75 nm tall fluidic channels, an amplification factor of 110 was obtained. This was used to show that the confined IDE was capable of detecting paracetamol, a chemically reversible species, in the presence of a large excess of (irreversible) ascorbic acid. More recently, Heo and co-workers reported an amplification factor of 1100 in devices combining vertical face and confinement in a microchannel.[133]

At a higher degree of parallelization (albeit not of miniaturization), an addressable interdigitated electrode array fabricated on a single glass substrate and consisting of 32 rows and 32 columns of electrodes forming 1024 addressable sensing pixels was reported by Ino and co-workers.[110, 111] The electrodes were defined by sputtered Ti/Pt and the gap between the fingers were 12 μm; each sensing pixel was located at the bottom of a microwell which was formed by photoresist SU-8 and had a dimension of 100 μm $\times$ 100 μm $\times$ 7 μm. Redox signals at each of the 1024 pixels could be acquired within 1 min, based on which a two-dimensional map of the distributions of electrochemical species could be obtained.

2.4.2 Recessed ring-disk electrodes and arrays

An alternative to the IDE is the coplanar ring-disk electrode, which consists of a central disk-shaped electrode surrounded by a second, ring-shaped electrode.[134–136] A further refinement of this structure which is particularly suitable for microfabrication is the recessed ring-disk electrode,[84, 112–117](Figure 2.5 c and

2.5 d), in which the two electrodes are placed on different planes. That is, a disk-shaped electrode forms the bottom of a recessed pit while the ring electrode is located at the rim, also forming part of the side walls of the pit. Most such devices are fabricated by etching cylindrical cavities through the first two layers of a metal/insulator/metal stack, the two metal layers thus becoming the electrodes. An important advantage of this approach compared to IDEs is that the size of the gap between the two electrodes is determined by the thickness of the insulating layer, which does not depend on the resolution of the lithographic method employed and which can be straightforwardly controlled down to nm resolution.

A theoretical analysis focusing on the current collection efficiency and the transient response for this device geometry was provided by Menshykau and co-workers.[115, 116] It was concluded, with support from some experiments, that, in the operation mode where the disk acted as generator electrode and the ring as collector electrode, the current collecting efficiency, which depends on the recess depth and size of the collector ring, could reach 90%.

An interesting work in which RRD electrodes were characterized by both cyclic voltammetry and scanning electrochemical microscopy was provided by Neugebauer and co-workers.[114] Structures with a vertical space between the bottom and rim electrodes of about 200 nm and ring-electrode diameters varying between 200 and 800 nm were created with nanosphere lithography. Electrochemical activity images of single RRD electrodes in good agreement with the ring dimensions were captured, and it was demonstrated how the potential of the unbiased top electrode was influenced by the ratio of the oxidized and reduced form of the redox couples.

In a recent proof-of-concept for sensor applications, Ma and co-workers[84, 117] reported a RRD electrode array in which the distance between the two electrodes was ∼100 nm. Cavities were created with nanosphere lithography through deposited layers of $Au/SiN_x/Au/SiO_2$. The cavities had a radius of about 230 nm, as defined by the size of the polystyrene spheres; an SEM image of the array is demonstrated in Figure 2.5 d. The collection efficiency was 98%. The arrays were also confined in a nanochannel; as a result the detection selectivity for $Ru(NH_3)_6{}^{3+}$ in the presence of ascorbic acid was increased by a factor of 7 compared to an array in the absence of confinement.

2.4.3 Nanogaps

Collection efficiency is further improved in a nanogap consisting of two parallel micrometric metal electrodes separated by a thin liquid layer,[118–130]as illustrated in Figure 2.5 e and 2.5 f. Conceptually, this configuration represents a direct downscaling of classic thin-layer cells. But whereas thin-layer cells with micron-scale spacing can be fabricated simply by sandwiching a thin spacer material between

two flat electrodes, microfabrication mostly relies on a so-called sacrificial layer approach. A bottom electrode, a sacrificial layer made of a different material and a top electrode are deposited and patterned on top of each other and passivated with an insulating layer. The resulting structure is illustrated in Figure 2.5 f, which shows a SEM image of the cross section of a nanogap device from the authors' laboratory. At least one access hole is then opened through the insulating layer to make contact to the sacrificial layer. In a final step the sacrificial layer is selectively etched away *via* the access hole(s) using a wet or isotropic dry etch, leaving a thin-layer-cell structure with an electrode spacing determined by the thickness of the sacrificial layer before its removal. The nanogap geometry thus shares with RRDs the benefit that the electrode spacing is set by the thickness of a thin film, which can be accurately controlled, rather than by the resolution of the lithographic method employed. Indeed, nanogaps with spacing 40-65 nm have been demonstrated using micron-resolution optical lithography.[122, 125, 127] A potential pitfall of this geometry is that any residual strain in the top electrode can cause it to deform slightly; because of the small spacing between the electrodes, even minor buckling can result in a significant relative change in the electrode spacing. This problem was encountered in some early designs in which the electrodes had a square geometry,[118] but was later alleviated through the use of a thin rectangular electrodes[120] or judicious choices of materials.[122, 125]

Because of the confined geometry of nanogap devices, the collection efficiency can in certain cases approach 100%, corresponding to a lower bound of $\sim 10^4$ for the amplification factor.[120] Largely thanks to this high degree of amplification, the detection of single molecules by redox-cycling electrochemistry was realized in nanogap devices.[123, 127] The ability to form arrays of separately addressable nanogap detectors was further exploited in a chip-based recording system enabling *invitro* measurements of individual neurotransmitter release events from neurons cultured directly on the chip.[137]

A strategy for further downscaling nanogaps to the sub-10 nm range was demonstrated by McCarty and co-workers,[130] who employed a combination of optical and molecular lithography to minimize the gap size. In their approach, a single- or multilayered molecular film was grown selectively on a first electrode followed by the deposition and patterning of a second electrode, so that the space between the two electrodes was controlled by the thickness of the molecular resist. This molecular layer thus fulfilled the function of sacrificial layer described above. The resulting nanogaps took the form of 2 μm long, 50 nm deep crevices between the two electrodes. Gap sizes as small as 4 nm were reported and successfully employed in redox-cycling experiments. The crevice geometry is open to bulk solution in a manner reminiscent of IDEs, for which these devices could provide a higher-performance substitute; the formation of sealed channel structures with higher collection efficiencies can also be envisioned with additional processing steps.

An alternative strategy for further downscaling nanogaps is to decrease the spacing between the electrodes by controlled electrodeposition of additional material on the electrode surfaces.[124] This approach has been employed extensively to create closely separated electrodes, in particular with the aim of measuring the electronic properties of molecules trapped between the electrodes.[138–140] These applications however tend to focus on sharp, point-like electrodes that lead to low collection efficiencies. Applying it to parallel planar electrodes would require electrodeposition under conditions in which mass transport is not limiting in order to achieve a uniform decrease of the electrode spacing. To our knowledge this has not been realized to date, however.

2.5 Electrochemistry and microfluidics integration

Microfluidic systems,[141–143] also referred to as "lab-on-chip" or "micro-total-analysis systems", consist of fluid handling elements such as valves, mixers and pumps integrated on a microchip. In general such miniaturized platforms offer several advantages including the ability to analyze small volume samples, reduction in reagent consumption and a consequent reduction in the amount of waste to be disposed, increased speed of analysis as well as potential for parallelization. Electrochemical detection is well suited for these applications as it is more readily integrated with fluidics elements than, for example, optical systems. Indeed, numerous integrated microfluidic electrochemical analytical systems have been reported in the last decade.[144–154]

In the early stages of development, the use of relatively complex silicon- and glass-based micromachining technology developed for integrated circuits (IC) was explored to fabricate microfluidic chips.[143] More recently the focus has shifted toward simpler techniques, micro/nanofluidic channels being created directly by lithography or molding using low-cost polymers such as polycarbonate (PC),[155] PDMS,[145, 156, 157] olefin copolymer (COC)[158] and SU-8.[159, 160] Among these materials, PDMS has been the most employed for its gas permeability, deformability and ability to quickly produce prototype devices. It however has important drawbacks including in particular analyte absorption and low solvent resistance. COC is a popular alternative for environmental lab-on-a-chip applications due to its high chemical resistance and minimal water adsorption. SU-8, a form of photoresist, is available in a wide range of viscosities, making it suitable to form thick layers and high-aspect-ratio structures. It can be directly spin-coated onto substrates and patterned lithographically, making it particularly convenient for integration with electronic components. Depending on the choice of materials, either the microfluidics are fabricated directly onto a substrate on which electrochemical components have already been defined, or the fluidic and electrochemical structures are formed on independent substrates that are bonded together afterwards.

In vitro experiments on living cells have benefited directly from fluidics integration. As discussed in section 2.2, early approaches relied on glass rings or pierced petri dishes being glued onto electrode substrates to create culture chambers. It is now instead relatively straightforward to build arrays of independent chambers addressable with individual electrodes. For instance a microwell device fabricated with SU-8 and PDMS for targeting single cells to detect quantal exocytosis – the burst release of intracellular transmitter molecules – was reported by Liu and co-workers.[161] Transparent nitrogen-doped diamond-like-carbon (DLC:N)/indium-tin-oxide (ITO) films were defined on glass slides using photolithography and thin-film etching as electrodes in order to allow visualization of cells immobilized on the electrodes using a conventional inverted microscope. DLC:N was reported to promote cell adhesion and to exhibit good electrochemical properties. SU-8 was then coated and patterned on the slides to form microwells as well as to insulate inactive areas of the conductive film, following which a poly(ethylene glycol) film was grafted to the surface of the SU-8 to inhibit protein adsorption and cell adhesion. Finally a PDMS gasket was cut and bonded to the substrate to confine a drop of solution containing cells to the middle of the device where 40 working electrodes were located. Single cells were targeted to the electrodes by functionalizing the electrodes with poly(L-lysine). Amperometric responses from individual cells could be recorded unambiguously without interference from nearby extraneous cells, and multiple recordings from the same electrode demonstrated that the device can be cleaned and reused without significant degradation of performance. This showed the potential of this platform as an alternative to carbon-fiber microelectrodes, which are extensively used to study quantal exocytosis of electroactive transmitters, with the additional advantage of increased throughput.

As another example, a disposable polymer-based protein immunosensor was demonstrated by Zou and co-workers.[158] Images, a schematic sketch and the fabrication process of the device are illustrated in Figure 2.6. A 3-inch blank cyclic olefin copolymer (COC) wafer with an ultra-smooth surface prepared by plastic injection molding was used as substrate. A gold IDE and contact pads were defined with e-beam lithography and lift-off after the COC wafer was coated with 10 nm Cr layer to render it compatible with lithography. Microfluidic channels were also fabricated in a second COC substrate using the same technique, except that here a Ni mold defined by a combination of lithography and electroplating was used, as shown in the right column of Figure 2.6 c. After drilling holes for fluidic connections in the microfluidic chip using a micro drill and growing a self-assembled monolayer of alkanethiols on the gold electrode surfaces, the two substrates were thermally bonded, generating a reaction chamber with a volume of 0.2 μl.

An example of a higher level of multi-functional integration was reported by Ferguson *et al.*,[162] who combined in a microfluidic electrochemical DNA sensor the functionalities of polymerase chain reaction (PCR), single-stranded DNA

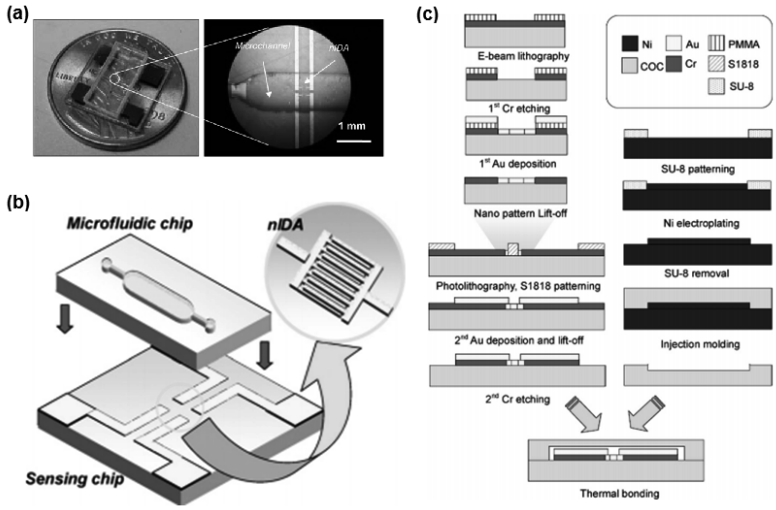

Figure 2.6: (a) Optical images, (b) schematic sketch of assembly and (c) fabrication process for a microfluidic protein immunosensor based on nanoscale IDEs. Reprinted from Zou *et al.*, *Sens. Actuators*, *A*, 2007, *136*, 518-526. Copyright (2006), with permission from Elsevier.

generation and sequence-specific electrochemical detection. The architecture and fabrication process of the device are shown in Figure 2.7. The detection system incorporated counter, (quasi-)reference and working electrodes that were defined by photolithography and lift-off. DNA probes were immobilized on the gold working electrodes *via* thiol chemistry. In parallel, a liquid chamber was fabricated by bonding a glass chip to a UV-ozone treated PDMS sheet in which fluidic channels had been cut, and fluidic vias were generated by drilling through the glass chip with a mill equipped with a diamond bit. The exposed side of the PDMS was then bonded to the chip to complete the integration. During use, liquid was pumped into the chamber through eyelets affixed to the vias with epoxy. Comparing with traditional methods, this disposable device was argued to minimize both the sample loss and the likelihood of contamination as the fluid pathways were contained within a sterile system.

Fragoso and co-worker reported a system to electrochemically detect breast cancer markers[155] which was realized by high-precision milling of PC sheets forming two distinct sections, a detection zone incorporating an electrode array and a fluid storage zone. The detection zone was divided into separate microfluidic chambers for samples and calibrators, and the fluidic storage zone was split into five reservoirs to store the reagents and sample. The solutions in the separate reservoirs were actuated by applying pressure through a syringe pump and steered to the detection zone *via* two integrated valves. The detection of proteic cancer markers in patient serum samples were demonstrated with detection limits below

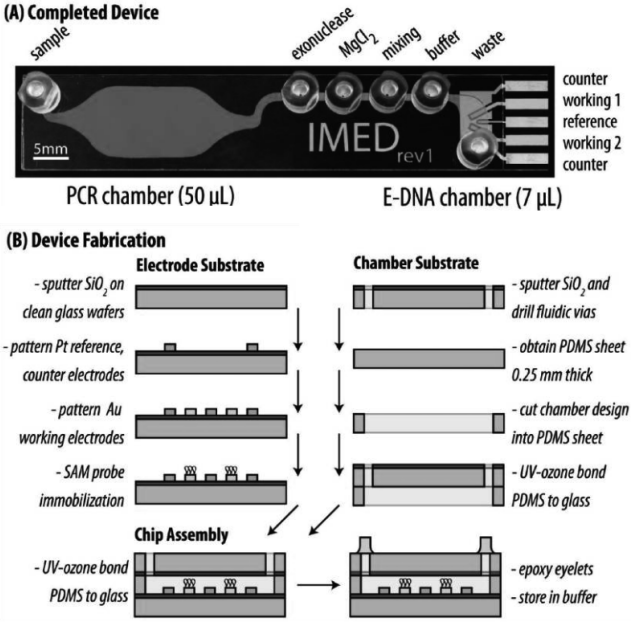

Figure 2.7: (A) Architecture and (B) fabrication process of a microfluidic electrochemical DNA sensor. Reprinted from Ferguson *et al.*, *Anal. Chem.*, 2009, *81*, 6503-6508. Copyright (2009), with permission from American Chemical Society.

10 ng mL^{-1}.

Nanogap devices can also be interfaced to fluidic systems. Under typical conditions the fluidic resistance of the nanochannel is so high that negligible flow takes place within the device; in this case the fluidics merely serve to bring a sample to the device, but analyte mass transport inside the device remains purely diffusive.[122, 163] When sufficient pressure is applied between access points to the detection region, on the other hand, advective flows can develop along the surface of the electrodes. Figure 2.1 b shows such a device reported by Mathwig and Lemay[128] in which microfluidic channels created in PDMS were interfaced to a nanochannel containing two separately addressable nanogap transducers. Record-low flow rates at the pL/min level could be measured from analyte time-of-flight measurements between the two electrochemical transducers.

Besides the benefits such as low consumption resulting from miniaturizing the fluidic components, phenomena specific to micro- and nanofluidic systems can also be harnessed to enhance electrochemical response.[1] For example, Wang *et al.* introduced a pre-concentrating device that could be integrated with an electrochemical detector to study homogeneous enzyme reaction kinetics.[164] The negatively charged enzymes were concentrated *via* the exclusion-enrichment effect

in a nanochannel[165] before being detected electrochemically near the outlet of the channel. In another example, Branagan and co-workers induced an electroosmotic flow (EOF) through a nanocapillary array membrane to enhance the delivery rate of analyte to annular nanoband electrodes embedded in the membrane.[166] An array of cylindrical nanochannels was created by focused ion beam milling through Au/polymer/Au/polymer membranes and subsequently sandwiched between two axially separated microchannels. The generated EOF enhanced the steady-state current by a factor >10 compared to a comparable structure without convective transport.

It is important to note that many electrochemical micro/nanofluidic systems still rely on macroscopic reference electrodes that are inserted in a solution reservoir external to the microfluidic system. This is because integrating a reliable, long-lived and stable microfabricated reference electrode in miniaturized fluidic systems remains a challenge.[167] The main problem is the rapid dissolution of the (small) electrode volume, which leads to short lifetimes. Though pseudo-reference electrodes – usually in the form of patterned metal thin films – can be used as a replacement, a true reference is often highly desirable. Analogues to conventional macroscopic liquid-junction reference electrodes have been demonstrated[168–170] in the form of encapsulated thin-film Ag/AgCl electrodes located in a dedicated compartment filled with reference electrolyte of constant Cl^- activity. Incorporating such a device however represents significant added complexity of design and fabrication. To form Ag/AgCl layers, an Ag film is normally deposited on a Au or Pt backbone layer in a first step, after which AgCl is formed by passing a current through the Ag layer in a solution with Cl^-.[170] Suzuki *et al.*[168] demonstrated an approach to fabricate a liquid-junction Ag/AgCl reference electrode using a resin sheet mainly formed by poly(ethylene glycol) as the liquid junction and screen-printed paste prepared from a mixture of KCl and 2-propanol as the electrolyte layer. Poly(vinylpyrrolidone) was added into the electrolyte layer to suppress the dissolution of AgCl, after which the electrode could maintain a stable potential level within ±1 mV for longer than 100 h. In another work Huang *et al.*[169] demonstrated a gel-coated Ti/Pd/Ag/AgCl electrode in which an agarose-stabilized KCl-gel membrane was introduced to serve both as a polymer-supported solid reference electrolyte and as ionic bridge for the electrode. The variation of the cell potential was less than 2 mV over pH 4-10 and insensitive to changes in the concentration of Cl^- (about 0.02-0.25 mV/pKCl).

2.6 CMOS integrated electrochemical systems

By virtue of being inherently electrical in nature, electrochemical sensors are particularly well suited for integration with microelectronics compared to sensors based on other detection principles. While still in relatively early stages of development, such integration could open significant opportunities in applications

such as high throughput screening, point-of-care (POC) diagnosis and implantable devices with flexibility, scalability and low cost.

Complementary metal-oxide-semiconductor (CMOS) electronics provide the backbone of most commercial integrated circuits including microprocessors, microcontrollers, image sensors, etc. Several CMOS-based potentiostats have been reported. A great deal of flexibility in circuit topology is provided by CMOS, such that it is possible to design integrated circuitry with full potentiostat functionality and a range of operation modes approaching that of table-top instruments.[171] For particular applications, however, it is often more practical to design more specialized electronics that implement a single electrochemical measurement technique of interest.[172–174] For example, Martin *et al.*[175] reported a custom integrated system for anodic stripping voltammetry (ASV) in which the detection circuit architecture was co-optimized with the electrode design to minimize parasitics, cancel solution matrix effects and improve the dynamic range of the system. Alternatively, the relative ease with which addressable arrays can be implemented using CMOS electronics provides an ideal platform for parallelized assays. This is dramatically illustrated by multiplexed microarrays functionalized with user-dialed probes *via* local, electronically-controlled functionalization[176, 177] or DNA synthesis.[178, 179] Such systems have been used for example for DNA hybridization,[176, 179–181] protein arrays[178] and a range of immunoassays.[177, 180]

The electrode materials most commonly employed in electrochemistry span a wide range including gold, platinum, palladium, carbon, graphite and silver, all of which share the feature of being incompatible with CMOS manufacturing equipment and processes. Electrodes must therefore be formed subsequently to the completion of any CMOS circuitry, in the so-called post-CMOS processing stage. During this stage high temperatures or intense plasmas that can destroy the circuits must be avoided. Martin and co-workers[175, 182] reported integrated sensing systems for environmental monitoring with two sets of seven Au working electrodes which were selectable *via* an electronic multiplexer, in addition to two sets of Pt auxiliary electrodes and Ag/AgCl reference electrodes. The post-CMOS processing started with the deposition and lift-off of a Ti/TiN/Ti/Pt layer stack in which the two Ti layers were applied as adhesion promoters and the TiN layer was used as a diffusion barrier between the top-level CMOS metallization and the Pt sensing electrode. Cr/Au and Ti/Ag electrodes were deposited and defined separately in the following steps. Subsequently, the Ag/AgCl reference electrodes were created from the Ag surfaces by submersion of the chip in 1 mM $FeCl_3$ for 2 min.

Another consideration is that it is in general more demanding to package CMOS-based chemical sensors. The chips must be packaged in such a way that the electrical components and interconnects are protected from contact with liquid, otherwise contaminants from solution may cause the properties of the transistors to drift over time. In specific case such as protein-based sensors, aggressive

electrode cleaning by piranha following organic solutions are required for reliable self-assembly of nanostructured bio-interfaces, so the packaging material must withstand this strong corrosiveness. SU-8, polyimide, epoxy and parylene are the most commonly used passivation material in the reported CMOS electrochemical microsystems.[173] In a microsystem for *in situ* detection of heavy metals in rain water,[175] SU-8 was used to form a dam-like structure between the bonding pads and the sensor sites. Packaging was accomplished by fixing the device onto a printed circuit board (PCB) by epoxy, making electrical connections by wirebonding and then encapsulating the wires in a two-coat epoxy process. It was concluded that, using this packaging strategy, the passivation had a lifetime greater than 100 days in saturated salt solutions and the properties of the electronics exhibited only minor drift after soaking in a 100 mM NaCl solution for more than 35 days.

A long-lasting, parylene-packaged, wire-bonded chip that survived a harsh piranha electrode cleaning process was demonstrated by Li and co-workers.[173] The post-CMOS fabrication began with the evaporation and wet etching of Ti/Au to form electrodes, and in the following step polyimide was spin-coated on the chip and patterned to uncover the electrodes and bonding pads. Afterwards the chip was wire-bonded to a packaging board and the assembly was coated with 5 μm parylene, following which the parylene was patterned to uncover the electrode sites using RIE in oxygen with a layer of crystal adhesive as the mask. This highlights the strengths of parylene as passivation material for CMOS-integrated bionsensors: high chemical resistance in addition to biocompatibility, biostability, low cytotoxicity, relatively simple chemical vapor deposition methods with low process temperatures, and easy etching in O_2 plasmas.[173]

To achieve a higher level of integration by incorporating microfluidics with CMOS electrochemical sensors and realize a complete lab-on-CMOS system, problems caused by topographical conflicts also need to be solved. The first issue is the size disparity between conventional CMOS chips and microfluidic components, such as channels, valves, pumps, etc.: the former typically occupy a few square millimeters, while microfluidic structures require significantly more area. The other inconvenience is the non-flat morphologies formed through the use of wire bonding or flip-chip bonding, which are the standard packaging techniques employed in the semiconductor industry to form electrical interconnections between CMOS chips and PCBs. These methods lead to uneven surfaces due to wires protruding out of the surface of the chip, which is itself at a different height than the surrounding board. However, a smooth surface without bumps or steps is usually a necessary starting point to create the microfluidic systems described above.

To address these issues, Huang and Mason[183] recently introduced an integration scheme in which the CMOS chip was embedded into a micro-machined silicon carrier as the packaging board, as shown in Figure 2.8. Both the CMOS chip and the carrier were first pressed onto a wax-coated glass handling wafer with the

front side of the chip facing the handling wafer. The assembly was then placed in a 150 °C chamber to allow the wax to melt, evening out the vertical position of the chip and carrier and attaching the chip to the handling wafer. Following this procedure, epoxy was applied to fill the gap between the chip and the carrier. Afterwards the glass handling wafer was released by softening the wax at 100 °C, and the wax remaining on the assembly was cleaned off. Polyimide was then coated onto the surface to smoothen it, metal wires for electrical interconnections were added by thin-film deposition and lithography, and a passivation layer consisting of silicon oxide/nitride/oxide was deposited at 100 °C using PECVD. Finally microfluidic structures with open channels made of SU-8 resist and covered by a glass cap were incorporated. Tubing was inserted laterally into the taper joint located at the sidewall of the SU-8 layer to enable high density world-to-chip microfluidic interconnections. The integrated device and schematic of the microfluidic circuits are shown in Figure 2.8b. The simultaneous fluidic and electrical operation of the lab-on-CMOS device was demonstrated by detecting a diluted Toluidine Blue O (TBO) sample.

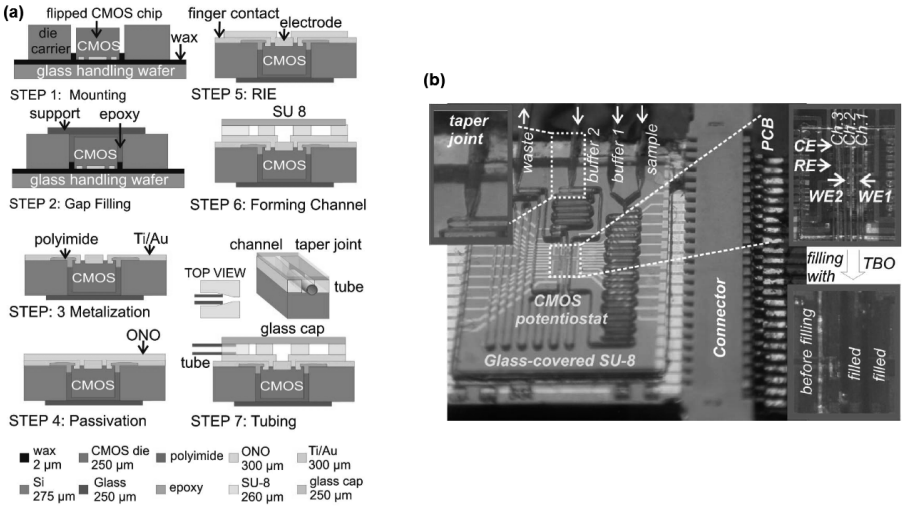

Figure 2.8: (a) Schematics of process flow for integrating microfluidics and CMOS electrochemical sensors. (b) The integrated device and schematic of the microfluidic circuits. The insets show: (upper left) the taper joint, (upper right) the three microfluidic detection channels across the CMOS potentiostat with on-chip electrodes and (lower right) the microfluidic channels being filled by TBO. Reprinted from Huang *et al.*, *Lab Chip*, 2013, *13*, 3929-3934 with permission from The Royal Society of Chemistry.

A method based on a similar concept was reported by Uddin and co-workers.[184] 3 mm × 3 mm × 260 μm CMOS chips were placed on a resist-coated oxidized silicon wafer and used as the mask to pattern the resist. The pattern was then transferred to the oxide layer and subsequently to the silicon wafer by RIE and DRIE,

respectively, so that cavities with approximately the same size as the CMOS chips were generated in this wafer. The wafer was then placed on a handle substrate and the CMOS chips were placed face-down inside the cavities of the wafer with the help of a flip-chip bonder. Another wafer coated with benzocyclobutene (BCB) was then placed on top of the CMOS chips and the cavity wafer and the whole stack was placed in a wafer bonding machine with pressure and elevated temperature (250 °C). As a result, the CMOS chips and the cavity wafer were bonded to the wafer coated with BCB. In the next step the handle substrate was removed from the front side of the CMOS chips, and spin-on glass was coated onto the surface to fill in the gap between the chip and the cavity wafer. Access to the contact pads was opened by RIE through the spin-on glass, and metal interconnects between the chip and the carrier were created by evaporation and lift-off. Up to this step the process was done on the wafer scale, after which the wafer was diced into individual chips. Measurements with the packaged chip showed that the post-integration processing did not affect the CMOS device parameters. A hybrid CMOS/microfluidic system was completed by placing the embedded chip on an acrylic stage and securing it mechanically by fastening an acrylic microfluidic channel on top with screws. A PDMS gasket was used to achieve a tight seal between chip and fluidic channel.

2.7 Summary and Outlook

This chapter reviewed the development of electrochemical measurement systems fabricated with micromachining technology. This set of techniques enables the systematic down-scaling of the dimensions of experimental elements to explore electrochemistry in new regimes and to enhance sensitivity and selectivity in sensor applications. Lithography-based techniques provide the opportunity to build arrays of components with high controllability and repeatability. Additionally, the flexibility to integrate detecting electrodes, microfluidics and even integrated circuits onto a single chip that includes the functionalities of sensing, fluidic handling and signal processing potentially creates new opportunities: while not going to replace existing instrumentation for classic measurements, the low costs, low sample and reagent volumes, low power consumptions and possibility of massive parallelization open the door to new classes of electrochemical analytical methods. One can envision fully integrated microfluidics-based electrochemical measurement systems implemented on top of CMOS electronics to provide high-throughput biomedical analytical platforms, point-of-care diagnostic tools, implantable devices, as well as portable and disposable food- and environment-monitoring sensors. Although a variety of difficulties remain, such as integration of reference electrode and effective packaging of the compact systems, the rapid pace of development means that such systems could become a practical reality on a relatively short time scale.

References

[1] Rassaei, L., Singh, P. S. and Lemay, S. G., Lithography-based Nanoelectrochemistry, *Anal. Chem.*, **2011**, *83*, 3974-3980.

[2] Wightman, R. M., Microvoltammetric Electrodes, *Anal. Chem.*, **1981**, *53*, 1125A-1134A.

[3] Bard, A. J. and Faulkner, L. R., *Electrochemical Methods: Fundamentals and Applications*, Wiley: New York, **2001**.

[4] Adams, R. N., Probing Brain Chemistry with Electroanalytical Techniques. *Anal. Chem.*, **1976**, *48*, 1126A-1138A.

[5] Ponchon, J. L., Cespuglio, R., Gonon, F., Jouvet, M. and Pujol, J. F., Normal Pulse Polarography with Carbon-fiber Electrodes for *in vitro* and *in vivo* Determination of Catecholamines, *Anal. Chem.*, **1979**, *51*, 1483-1486.

[6] McCreery, R. L., Dreiling, R. and Adams, R. N., Voltammetry in Brain-tissue - Quantitative Studies of Drug Interactions, *Brain Res.*, **1974**, *73*, 23-33.

[7] Adams, R. N., *In vivo* Electrochemical Recording A New Neurophysiological Approach, *Trends Neurosci.*, **1978**, *1*, 160-163.

[8] Thomas, C. A., Jr., Springer, P. A., Loeb, G. E., Berwald-Netter, Y. and Okun, L. M., A Miniature Microelectrode Array to Monitor the Bioelectric Activity of Ccultured Cells, *Exp. Cell Res.*, **1972**, *74*, 61-66.

[9] May, G. A., Shamma, S. A. and White, R. L., Tantalum on Sapphire Microelectrode Array, *IEEE Trans. Electron Devices*, **1979**, *26*, 1932-1939.

[10] Prohaska, O., Olcaytug, F., Womastek, K. and Petsche, H., Multielectrode for Intracortical Recordings Produced by Thin-film Technology, *Electroencephalogr. Clin. Neurophysiol.*, **1977**, *42*, 421-422.

[11] Gross, G. W., Simultaneous Single Unit Recording in Vitro with a Photoetched Laser Deinsulated Gold Multimicroelectrode Surface, *IEEE Trans. Biomed. Eng.*, **1979**, *26*, 273-279.

[12] Pine, J., Recording Action-potentials from Cultured Neurons with Extracellular Micro-circuit Electrodes, *J. Neurosci. Meth.*, **1980**, *2*, 19-31.

[13] Thormann, W., Vandenbosch, P. and Bond, A. M., Voltammetry at Linear Gold and Platinum Microelectrode Arrays Produced by Lithographic Techniques, *Anal. Chem.*, **1985**, *57*, 2764-2770.

[14] Kuperstein, M. and Whittington, D. A., A Practical 24 Channel Microelectrode for Meural Recording *in vivo*, *IEEE Trans. Biomed. Eng.*, **1981**, *28*, 288-293.

[15] Kern, W. and Shaw, J. M., Electrochemical Delineation of Tungsten Films for Microelectronic Devices, *J. Electrochem. Soc.*, **1971**, *118*, 1699-1704.

[16] Siu, W. and Cobbold, R. S. C., Characteristics of a Multicathode Polarographic Oxygen Electrode, *Med. Biol. Eng.*, **1976**, *14*, 109-121.

[17] Feeney, R. and Kounaves, S. P., Microfabricated Ultramicroelectrode Arrays: Developments, Advances, and Applications in Environmental Analysis, *Electroanalysis*, **2000**, *12*, 677-684.

[18] Glass, R. S., Perone, S. P. and Ciarlo, D. R., Application of Information-theory to Electroanalytical Measurements Using a Multielement Microelectrode Array, *Anal. Chem.*, **1990**, *62*, 1914-1918.

[19] Compton, R. G., Foord, J. S. and Marken, F., Electroanalysis at Diamond-like and Doped-diamond Electrodes, *Electroanalysis*, *15*, **2003**, 1349-1363.

[20] Hu, J. P., Holt, K. B. and Foord, J. S., Focused Ion Beam Fabrication of Boron-doped Diamond Ultramicroelectrodes, *Anal. Chem.*, **2009**, *81*, 5663-5670.

[21] Soh, K. L., Kang, W. P., Davidson, J. L. and *et al.*, Diamond-derived Microelectrodes Array for Electrochemical Analysis, *Diamond Relat. Mater.*, **2004**, *13*, 2009-2015.

[22] Simm, A. O., Banks, C. E., Ward-Jones, S. and *et al.*, Boron-doped Diamond Microdisc Arrays: Electrochemical Characterisation and Their Use as a Substrate for the Production of Microelectrode Arrays of Diverse Metals (Ag, Au, Cu) *via* Electrodeposition, *Analyst*, **2005**, *130*, 1303-1311.

[23] Zoski, C. G., Simjee, N., Guenat, O. and Koudelka-Hep, M., Addressable Microelectrode Arrays: Characterization by Imaging with Scanning Electrochemical Microscopy, *Anal. Chem.*, **2004**, *76*, 62-72.

[24] Lin, Z., Takahashi, Y., Kitagawa, Y. and *et al.*, An Addressable Microelectrode Array for Electrochemical Detection, *Anal. Chem.*, **2008**, *80*, 6830-6833.

[25] Polsky, R., Harper, J. C., Wheeler, D. R. and Brozik, S. M., Multifunctional Electrode Arrays: Towards a Universal Detection Pplatform, *Electroanalysis*, **2008** *20*, 671-679.

[26] Sanchez-Molas, D., Esquivel, J. P., Sabate, N., Munoz, F. X. and del Campo, F. J., High Aspect-ratio, Fully Conducting Gold Micropillar Array Electrodes: Silicon Micromachining and Electrochemical Characterization, *J. Phys. Chem. C*, **2012**, *116*, 18831-18846.

[27] Wehmeyer, K. R., Deakin, M. R. and Wightman, R. M., Electroanalytical Properties of Band Electrodes of Submicrometer Width, *Anal. Chem.*, **1985**, *57*, 1913-1916.

[28] Arrigan, D. W. M., Nanoelectrodes, Nanoelectrode Arrays and Their Applications, *Anal. Chem.*, **2004**, *129*, 1157-1165.

[29] Huang, X. J., O'Mahony, A. M. and Compton, R. G., Microelectrode Arrays for Electrochemistry: Approaches to Fabrication, *Small*, **2009**, *5*, 776-788.

[30] Oja, S. M., Wood, M. and Zhang, B., Nanoscale Electrochemistry, *Anal. Chem.*, **2013**, *85*, 473-486.

[31] Murray, R. W., Nanoelectrochemistry: Metal Nanoparticles, Nanoelectrodes, and Nanopores, *Chem. Rev.*, **2008**, *108*, 2688-2720.

[32] Okazaki, S., Resolution Limits of Optical Lithography, *J. Vac. Sci. Technol. B*, **1991**, *9*, 2829-2833.

[33] Zoski, C. G., Ultramicroelectrodes: Design, Fabrication, and Characterization, *Electroanalysis*, **2002**, *14*, 1041-1051.

[34] Cox, J. T. and Zhang, B., Nanoelectrodes: Recent Advances and New Directions, *Annu. Rev. Anal. Chem.*, **2012**, *5*, 253-272.

[35] Nagahara, L. A., Thundat, T. and Lindsay, S. M. 1989. Preparation and Characterization of STM Tips for Electrochemical Studies, *Rev. Sci. Instrum.*, **1989**, *60*, 3128-3130.

[36] Mirkin, M. V., Fan, F. R. F. and Bard, A. J., Scanning Ectrochemical Microscopy .13. Evaluation of the Tip Shapes of Nanometer Size Microelectrodes, *J. Electroanal. Chem.*, **1992**, *328*, 47-62.

[37] Fan, F. R. F., Kwak, J. and Bard, A. J., Single Molecule Electrochemistry, *J. Am. Chem. Soc.*, **1996**, *118*, 9669-9675.

[38] Sun, P., Zhang, Z. Q., Guo, J. D. and Shao, Y. H., Fabrication of Nanometer-sized Electrodes and Tips for Scanning Electrochemical Microscopy, *Anal. Chem.*, **2001**,*73*, 5346-5351.

[39] Slevin, C. J., Gray, N. J., Macpherson, J. V., Webb, M. A. and Unwin, P. R., Fabrication and Characterisation of Nanometre-sized Platinum Electrodes for Voltammetric Analysis and Imaging, *Electrochem. Commun.*, **1999**, *1*, 282-288.

[40] Conyers, J. L. and White, H. S., Electrochemical Characterization of Electrodes with Submicrometer Dimensions, *Anal. Chem.*, **2000**, *72*, 4441-4446.

[41] Macpherson, J. V. and Unwin, P. R., Combined Scanning Electrochemical-Atomic Force Microscopy, *Anal. Chem.*, **2000**, *72*, 276-285.

[42] Gray, N. J. and Unwin, P. R., Simple Procedure for the Fabrication of Silver/Silver Chloride Potentiometric Electrodes with Micrometre and Smaller Dimensions: Application to Scanning Electrochemical Microscopy, *Analyst*, **2000**, *125*, 889-893.

[43] Chen, S. L. and Kucernak, A., Fabrication of Carbon Microelectrodes with an Effective Rdius of 1 nm, *Electrochem. Commun.*, **2002**, *4*, 80-85.

[44] Chen, S. L. and Kucernak, A., The Voltammetric Response of Nanometer-sized Carbon Electrodes, *J. Phys. Chem. B*, **2002**, *106*, 9396-9404.

[45] Abbou, J., Demaille, C., Druet, M. and Moiroux, J., Fabrication of Submicrometer-sized Gold Electrodes of Controlled Geometry for Scanning Electrochemical-atomic Force Microscopy, *Anal. Chem.*, **2002**, *74*, 6355-6363.

[46] Watkins, J. J., Chen, J., White, H. S. and *et al.*, Zeptomole Voltammetric Detection and Electron-transfer Rate Measurements Using Platinum Electrodes of Nanometer Dimensions, *Anal. Chem.*, **2003**, *75*, 3962-3971.

[47] Penner, R. M., Heben, M. J., Longin, T. L. and Lewis, N. S., Fabrication and Use of Nanometer-sized Electrodes in Electrochemistry, *Science*, **1990**, *250*, 1118-1121.

[48] Pendley, B. D. and Abruna, H. D., Construction of Submicrometer Voltammetric Electrodes, *Anal. Chem.*, **1990**, *62*, 782-784.

[49] Shao, Y. H., Mirkin, M. V., Fish, G. *et al.*, Nanometer-sized Electrochemical Sensors, *Anal. Chem.*, **1997**, *69*, 1627-1634.

[50] Katemann, B. B. and Schuhmann, T., Fabrication and Characterization of Needle-type Pt-disk Nanoelectrodes, *Electroanalysis*, **2002**, *14*, 22-28.

[51] Zhang, B., Zhang, Y. H. and White, H. S., The Nanopore Electrode, *Anal. Chem.*, **2004**, *76*, 6229-6238.

[52] Sun, P. and Mirkin, M. V., Kinetics of Electron-transfer Reactions at Nanoelectrodes, *Anal. Chem.*, **2006**, *78*, 6526-6534.

[53] Zhang, B., Galusha, J., Shiozawa, P. G. and *et al.*, Bench-top Method for Fabricating Glass-sealed Nanodisk Electrodes, Glass Nanopore Electrodes, and Glass Nanopore Membranes of Controlled Size, *Anal. Chem.*, **2007**, *79*, 4778-4787.

[54] Thiebaud, P., Beuret, C., de Rooij, N. F. and Koudelka-Hep, M., Microfabrication of Pt-tip Microelectrodes, *Sens. Actuators, B*, **2000**, *70*, 51-56.

[55] Qiao, Y., Chen, J., Guo, X. L. and *et al.*, Fabrication of Nanoelectrodes for Neurophysiology: Cathodic Electrophoretic Paint Insulation and Focused Ion Beam Milling, *Nanotechnology*, **2005**, *16*, 1598-1602.

[56] Menke, E. J., Thompson, M. A., Xiang, C., Yang, L. C. and Penner, R. M., Lithographically Patterned Nanowire Electrodeposition, *Nat. Mater.*, **2006**, *5*, 914-919.

[57] Yang, F., Taggart, D. K. and Penner, R. M., Fast, Sensitive Hydrogen Gas Detection Using Single Palladium Nanowires that Resist Fracture, *Nano Lett.*, **2009**, *9*, 2177-2182.

[58] Hujdic, J. E., Sargisian, A. P., Shao, J. R., Ye, T. and Menke, E. J., High-density Gold Nanowire Arrays by Lithographically Patterned Nanowire Electrodeposition, *Nanoscale*, **2011**, *3*, 2697-2699.

[59] Heo, J. I., Shim, D. S., Teixidor, G. T. and *et al.*, Carbon Interdigitated Array Nanoelectrodes for Electrochemical Applications, *J. Electrochem. Soc.*, **2011**, *158*, J76-J80.

[60] Varnell, G. L., Spicer, D. F. and Rodger, A. C., E-beam Writing Techniques for Semiconductor-device Fabrication, *J. Vac. Sci. Technol.*, **1973**, *10*, 1048-1051.

[61] Finot, E., Bourillot, E., Meunier-Prest, R. and *et al.*, Performance of Interdigitated Nanoelectrodes for Electrochemical DNA Biosensor, *Ultramicroscopy*, **2003**, *97*, 441-449.

[62] Sandison, M. E. and Cooper, J. M., Nanofabrication of Electrode Arrays by Electron-beam and Nanoimprint Lithographies, *Lab Chip*, **2006**, *6*, 1020-1025.

[63] Naka, K., Hayashi, H., Senda, M., Shiraishi, H. and Konishi, S., Effect of Nano Stripe Carbonized-polymer Electrode on High S/N Ratio in Electrochemical Detection. *Proceedings of the IEEE Twentieth Annual International Conference on Micro Electro Mechanical Systems* **2007**, *1/2*, 374-377.

[64] Hoeben, F. J. M., Meijer, F. S., Dekker, C. and *et al.*, Toward Single-enzyme Molecule Electrochemistry: [NiFe]-hydrogenase Protein Film Voltammetry at Nanoelectrodes, *ACS Nano*, **2008**, *2*, 2497-2504.

[65] Moretto, L. M., Tormen, M., De Leo, M., Carpentiero, A. and Ugo, P., Polycarbonate-based Ordered Arrays of Electrochemical Nanoelectrodes Obtained by E-beam Lithography, *Nanotechnology*, **2011**, *22*, 185305.

[66] Dawson, K., Wahl, A., Murphy, R. and O'Riordan, A., Electroanalysis at Single Gold Nanowire Electrodes, *J. Phys. Chem. C*, **2012**, *116*, 14665-14673.

[67] Kleijn, S. E. F., Yanson, A. I. and Koper, M. T. M., Electrochemical Characterization of Nano-sized Gold Electrodes Fabricated by Nano-lithography, *J. Electroanal. Chem.*, **2012**, *666*, 19-24.

[68] Niwa, O., Morita, M. and Tabei, H., Electrochemical-behavior of Reversible Redox Species at Interdigitated Array Electrodes with Different Geometries - Consideration of Redox Cycling and Collection Efficiency, *Anal. Chem.*, **1990**, *62*, 447-452.

[69] Lanyon, Y. H. and Arrigan, D. W. M., Recessed Nanoband Electrodes Fabricated by Focused Ion Beam Milling, *Sens. Actuators, B*, **2007**, *121*, 341-347.

[70] Lanyon, Y. H., De Marzi, G., Watson, Y. E. and *et al.*, Fabrication of Nanopore Array Electrodes by Focused Ion Beam Milling, *Anal. Chem.*, **2007**, *79*, 3048-3055.

[71] Rauf, S., Shiddiky, M. J. A., Asthana, A. and Dimitrov, K., Fabrication and Characterization of Gold Nanohole Electrode Arrays, *Sens. Actuators, B*, **2012**, *173*, 491-496.

[72] Menon, V. P. and Martin, C. R., Fabrication and Evaluation of Nanoelectrode Ensembles, *Anal. Chem.*, **1995**, *67*, 1920-1928.

[73] Penner, R. M. and Martin, C. R., Preparation and Electrochemical Characterization of Ultramicroelectrode Ensembles, *Anal. Chem.*, **1987**, *59*, 2625-2630.

[74] Lemay, S. G., van den Broek, D. M., Storm, A. J. and *et al.*, Lithographically Fabricated Nanopore-based Electrodes for Electrochemistry, *Anal. Chem.*, **2005**, *77*, 1911-1915.

[75] Krapf, D., Wu, M. Y., Smeets, R. M. M. and *et al.*, Fabrication and Characterization of Nanopore-based Electrodes with Radii Down to 2 nm, *Nano Lett.*, **2002**, *6*, 105-109.

[76] Yang, M., Qu, F., Lu, Y. and *et al.*, Platinum Nanowire Nanoelectrode Array for the Fabrication of Biosensors, *Biomaterials*, **2006**, *27*, 5944-5950.

[77] Chou, S. Y., Krauss, P. R. and Renstrom, P. J., Imprint Lithography with 25-nanometer Resolution, *Science*, **1996**, *272*, 85-87.

[78] Beck, M., Persson, F., Carlberg, P. and *et al.*, Nanoelectrochemical Transducers for (Bio-) Chemical Sensor Applications Fabricated by Nanoimprint Lithography, *Microelectron. Eng.*, **2004**, *73*, 837-842.

[79] Huang, C. W. and Lu, M. S. C., Electrochemical Detection of the Neurotransmitter Dopamine by Nanoimprinted Interdigitated Electrodes and A CMOS Circuit with Enhanced Collection Efficiency, *IEEE Sens. J.*, **2011**, *11*, 1826-1831.

[80] Haynes, C. L. and Van Duyne, R. P., Nanosphere Lithography: A Versatile Nanofabrication Tool for Studies of Size-dependent Nanoparticle Optics, *J. Phys. Chem. B*, **2001**, *105*, 5599-5611.

[81] Valsesia, A., Lisboa, P., Colpo, P. and Rossi, F., Fabrication of Polypyrrole-based Nanoelectrode Arrays by Colloidal Lithography, *Anal. Chem.*, **2006**, *78*, 7588-7591.

[82] Lohmuller, T., Muller, U., Breisch, S. and *et al.*, Nano-porous Electrode Systems by Colloidal Lithography for Sensitive Electrochemical Detection: Fabrication Technology and Properties, *J. Micromech. Microeng.*, **2008**, *181*, 115011.

[83] Hees, J., Hoffmann, R., Kriele, A. and *et al.*, Nanocrystalline Diamond Nanoelectrode Arrays and Ensembles, *ACS Nano*, **2011**, *5*, 3339-3346.

[84] Ma, C., Contento, N. M., Gibson, L. R., 2nd and Bohn, P. W., Recessed Ring-disk Nanoelectrode Arrays Integrated in Nanofluidic Structures for Selective Electrochemical Detection, *Anal. Chem.*, **2013**, *85*, 9882-9888.

[85] Morris, R. B., Franta, D. J. and White, H. S., Electrochemistry at Pt Band Electrodes of Width Approaching Molecular Dimensions - Breakdown of Transport-equations at Very Small Electrodes, *J. Phys. Chem.*, **1987**, *91*, 3559-3564.

[86] Dumitrescu, I., Unwin, P. R. and Macpherson, J. V., Electrochemistry at Carbon Nanotubes: Perspective and Issues, *Chem. Commun.*, **2009**, *45*, 6886-6901.

[87] Dumitrescu, I., Unwin, P. R., Wilson, N. R. and Macpherson, J. V., Single-walled Carbon Nanotube Network Ultramicroelectrodes, *Anal. Chem.*, **2008**, *80*, 3598-3605.

[88] Dumitrescu, I., Edgeworth, J. P., Unwin, P. R. and Macpherson, J. V., Ultrathin Carbon Nanotube Mat Electrodes for Enhanced Amperometric Detection, *Adv. Mater.*, **2009**, *21*, 3105-3109.

[89] Heller, I., Kong, J., Heering, H. A. *et al.*, Individual Single-walled Carbon Nanotubes as Nanoelectrodes for Electrochemistry, *Nano Lett.*, **2005**, *5*, 137-142.

[90] Quinn, B. M. and Lemay, S. G., Single-walled Carbon Nanotubes as Templates and Interconnects for Nanoelectrodes, *Adv. Mater.*, **2006**, *18*, 855-859.

[91] Day, T. M., Unwin, P. R., Wilson, N. R. and Macpherson, J. V., Electrochemical Templating of Metal Nanoparticles and Nanowires on Single-walled Carbon Nanotube Networks, *J. Am. Chem. Soc.*, **2005**, *127*, 10639-10647.

[92] Quinn, B. M., Dekker, C. and Lemay, S. G., Electrodeposition of Noble Metal Nanoparticles on Carbon Nanotubes, *J. Am. Chem. Soc.*, **2005**, *127*, 6146-6147.

[93] Dawson, K., Strutwolf, J., Rodgers, K. P. and *et al.*, Single nanoskived Nanowires for Electrochemical Applications, *Anal. Chem.*, **2011**, *83*, 5535-5540.

[94] Xu, Q., Rioux, R. M., Dickey, M. D. and Whitesides, G. M., Nanoskiving: A New Method to Produce Arrays of Nanostructures, *Acc. Chem. Res.*, **2008**, *41*, 1566-1577.

[95] Campbell, J. K., Sun, L. and Crooks, R. M., Electrochemistry Using Single Carbon Nanotubes, *J. Am. Chem. Soc.*, **1999**, *121*, 3779-3780.

[96] Guillorn, M. A., McKnight, T. E., Melechko, A. and *et al.*, Individually Addressable Vertically Aligned Carbon Nanofiber-based Electrochemical Probes, *J. Appl. Phys.*, **2002**, *91*, 3824-3828.

[97] Mai, L., Dong, Y., Xu, L. and Han, C., Single Nanowire Electrochemical Devices, *Nano Lett.*, **2010**, *10*, 4273-4278.

[98] Zhao, M., Huang, J., Zhou, Y. and *et al.*, A Single Mesoporous ZnO/Chitosan Hybrid Nanostructure for a Novel Free Nanoprobe Type Biosensor, *Biosens. Bioelectron.*, **2013**, *43*, 226-230.

[99] Percival, S. J. and Zhang, B., Electrocatalytic Reduction of Oxygen at Single Platinum Nanowires, *J. Phys. Chem. C*, **2013**, *117*, 13928-13935.

[100] Kranz, C., Friedbacher, G., Mizaikoff, B. and *et al.*, Integrating an Ultramicroelectrode in an AFM Cantilever: Combined Technology for Enhanced Information, *Anal. Chem.*, **2001**, *73*, 2491-2500.

[101] Lugstein, A., Bertagnolli, E., Kranz, C. and Mizaikoff, B., Fabrication of A Ring Nanoelectrode in an AFM tip: Novel Approach Towards Simultaneous Electrochemical and Topographical Imaging, *Surf. Interface Anal.*, **2002**, *33*, 146-150.

[102] Burt, D. P., Wilson, N. R., Weaver, J. M. R., Dobson, P. S. and Macpherson, J. V., Nanowire Probes for High Resolution Combined Scanning Electrochemical Microscopy - Atomic Force Microscopy, *Nano Lett.*, **2005**, *5*, 639-643.

[103] Bai, S. J., Fabian, T., Prinz, F. B. and Fasching, R. J., Nanoscale Probe System for Cell-organelle Analysis, *Sens. Actuators, B*, **2008**, *130*, 249-257.

[104] Smirnov, W., Kriele, A., Hoffmann, R. and *et al.*, Diamond-modified AFM Probes: From Diamond Nanowires to Atomic Force Microscopy-integrated Boron-doped Diamond Electrodes, *Anal. Chem.*, **2011**, *83*, 4936-4941.

[105] Sanderson, D. G. and Anderson, L. B., Filar electrodes - Steady-state Currents and Spectroelectrochemistry at Twin Interdigitated Electrodes, *Anal. Chem.*, **1985**, *57*, 2388-2393.

[106] Aoki, K., Morita, M., Niwa, O. and Tabei, H., Quantitative-analysis of Reversible Diffusion-Controlled Currents of Redox Soluble Species at Interdigitated Array Electrodes under Steady-State Conditions, *J. Electroanal. Chem.*, **1988**, *256*, 269-282.

[107] Niwa, O., Xu, Y., Halsall, H. B. and Heineman, W. R. 1993. Small-volume Voltammetric Detection of 4-Aminophenol with Interdigitated Array Electrodes and Its Application to Electrochemical Enzyme-immunoassay, *Anal. Chem.*, **1993**, *65*, 1559-1563.

[108] Dam, V. A. T., Olthuis, W. and van den Berg, A., Redox Cycling with Facing Interdigitated Array Electrodes as a Method for Selective Detection of Redox Species, *Analyst*, **2007**, *132*, 365-370.

[109] Goluch, E. D., Wolfrum, B., Singh, P. S., Zevenbergen, M. A. G. and Lemay, S. G., Redox Cycling in Nanofluidic Channels Using Interdigitated Electrodes, *Anal. Bioanal. Chem.*, **2009**, *394*, 447-456.

[110] Ino, K., Saito, W., Koide, M. and *et al.*, Addressable Electrode Array Device with IDA Electrodes for High-throughput Detection, *Lab Chip*, **2011**, *11*, 385-388.

[111] Ino, K., Nishijo, T., Arai, T. and *et al.*, LocalRedox-cycling-based Electrochemical Chip Device with Deep Microwells for Evaluation of Embryoid Bodies, *Angew. Chem. -Int. Edit.*, **2012**, *51*, 6648-6652.

[112] Henry, C. S. and Fritsch, I., Microcavities Containing Individually Addressable Recessed Microdisk and Tubular Nanoband Electrodes, *J. Electrochem. Soc.*, **1999**, *146*, 3367-3373.

[113] Vandaveer, W. R., Woodward, D. J. and Fritsch, I., Redox Cycling Measurements of a Model Compound and Dopamine in Ultrasmall Volumes with a Self-contained Microcavity Device, *Electrochim. Acta*, **2003**, *48*, 3341-3348.

[114] Neugebauer, S., Muller, U., Lohmuller, T. and *et al.*, Characterization of Nanopore Electrode Structures as Basis for Amplified Electrochemical Assays, *Electroanalysis*, **2006**, *18*, 1929-1936.

[115] Menshykau, D., O'Mahony, A. M., del Campo, F. J., Munoz, F. X. and Compton, R. G., Microarrays of Ring-recessed Disk Electrodes in Transient Generator-collector Mode: Theory and Experiment, *Anal. Chem.*, **2009**, *81*, 9372-9382.

[116] Menshykau, D., del Campo, F. J., Munoz, F. X. and Compton, R. G., Current Collection Efficiency of Micro- and Nano-ring-recessed Disk Electrodes and of Arrays of These Electrodes, *Sens. Actuators, B*, **2009**, *138*, 362-367.

[117] Ma, C. X., Contento, N. M., Gibson, L. R. and Bohn, P. W., Redox Cycling in Nanoscale-recessed Ring-disk Electrode Arrays for Enhanced Electrochemical Sensitivity, *ACS Nano*, **2013**, *7*, 5483-5490.

[118] Zevenbergen, M. A. G., Krapf, D., Zuiddam, M. R. and Lemay, S. G., Mesoscopic Concentration Fluctuations in a Fluidic Nanocavity Detected by Redox Cycling, *Nano Lett.*, **2007**, *7*, 384-388.

[119] Wolfrum, B., Zevenbergen, M. and Lemay, S., Nanofluidic Redox Cycling Amplification for the Selective Detection of Catechol, *Anal. Chem.*, **2008**, *80*, 972-977.

[120] Zevenbergen, M. A. G., Wolfrum, B. L., Goluch, E. D., Singh, P. S. and Lemay, S. G., Fast Electron-transfer Kinetics Probed in Nanofluidic Dhannels, *J. Am. Chem. Soc.*, **2009**, *131*, 11471-11477.

[121] Zevenbergen, M. A. G., Singh, P. S., Goluch, E. D., Wolfrum, B. L. and Lemay, S. G., Electrochemical Correlation Spectroscopy in Nanofluidic Cavities, *Anal. Chem.*, **2009**, *81*, 8203-8212.

[122] Katelhon, E., Hofmann, B., Lemay, S. G. and *et al.*, Nanocavity Redox Cycling Sensors for the Detection of Dopamine Fluctuations in Microfluidic Gradients, *Anal. Chem.*, **2010**, *82*, 8502-8509.

[123] Zevenbergen, M. A. G., Singh, P. S., Goluch, E. D., Wolfrum, B. L. and Lemay, S. G., Stochastic Sensing of Single Molecules in a Nanofluidic Electrochemical Device, *Electroanalysis*, **2011**, Nano Lett., *11*, 2881-2886.

[124] Kim, J. H., Moon, H., Yoo, S. and Choi, Y. K., Nanogap Electrode Fabrication for a Nanoscale Device by Volume-expanding Electrochemical Synthesis, *Small*, **2011**, *7*, 2210-2216.

[125] Kang, S., Mathwig, K. and Lemay, S. G., Response Time of Nanofluidic Electrochemical Sensors, *Lab Chip*, **2012**, *12*, 1262-1267.

[126] Mathwig, K., Mampallil, D., Kang, S. and Lemay, S. G., Electrical Cross-correlation Spectroscopy: Measuring Picoliter-per-minute Flows in Nanochannels, *Phys. Rev. Lett.*, **2012**, *109*, 118302.

[127] Kang, S., Nieuwenhuis, A. F., Mathwig, K., Mampallil, D. and Lemay, S. G., Electrochemical Single-molecule Detection in Aqueous Solution Using Self-aligned Nanogap Transducers, *ACS Nano*, **2013**, *7* 10931-10937.

[128] Mathwig, K. and Lemay, S. G., Pushing the Limits of Electrical Detection of Ultralow Flows in Nanofluidic Channels, *Micromachines*, **2013**, *4*, 138-148.

[129] Mampallil, D., Mathwig, K., Kang, S. and Lemay, S. G., Redox Couples with Unequal Diffusion Coefficients: Effect on Redox Cycling, *Anal. Chem.*, **2013**, *85*, 6053-6058.

[130] McCarty, G. S., Moody, B. and Zachek, M. K., Enhancing Electrochemical Detection by Scaling Solid State Nanogaps, *J. Electroanal. Chem.*, **2010**, *643*, 9-14.

[131] Van Gerwen, P., Laureyn, W., Laureys, W. and *et al.*, Nanoscaled Interdigitated Electrode Arrays for Biochemical Sensors, *Sens. Actuators, B*, **1998**, *49*, 73-80.

[132] Yang, L. J., Li, Y. B. and Erf, G. F., Interdigitated Array Microelectrode-based Electrochemical Impedance Immunosensor for Detection of Escherichia Coli O157 : H7, *Anal. Chem.*, **2004**, *76*, 1107-1113.

[133] Heo, J. I., Lim, Y. and Shin, H., The Effect of Channel Height and Electrode Aspect Ratio on Redox Cycling at Carbon Interdigitated Array Nanoelectrodes Confined in a Microchannel, *Analyst*, **2013**, *138*, 6404-6411.

[134] Albery, W. J. H., M. L., *Ring-Disc Electrodes*. Oxford University Press: London, **1971**.

[135] Zhao, G., Giolando, D. M. and Kirchhoff, J. R., Carbon Ring Disk Ultramicroelectrodes, *Anal. Chem.*, **1995**, *67*, 1491-1495.

[136] Liljeroth, P., Johans, C., Slevin, C. J., Quinn, B. M. and Kontturi, K., Disk-generation/Ring-collection Scanning Electrochemical Microscopy: Theory and Application, *Anal. Chem.*, **2002**, *74*, 1972-1978.

[137] Yakushenko, A., Kaetelhoen, E. and Wolfrum, B., Parallel On-Chip Analysis of Single Vesicle Neurotransmitter Release, *Anal. Chem.*, **2013**, *85*, 5483-5490.

[138] Reed, M. A., Zhou, C., Muller, C. J., Burgin, T. P. and Tour, J. M., Conductance of a Molecular Junction, *Science*, **1997**, *278*, 252-254.

[139] Joachim, C., Gimzewski, J. K. and Aviram, A., Electronics Using Hybrid-molecular and Mono-molecular Devices, *Nature*, **2000**, *408*, 541-548.

[140] Akkerman, H. B., Blom, P. W. M., de Leeuw, D. M. and de Boer, B., Towards Molecular Electronics with Large-area Molecular Junctions, *Nature*, **2006**, *441*, 69-72.

[141] Manz, A., Fettinger, J. C., Verpoorte, E. and *et al.*, Micromachining of Monocrystalline Silicon and Glass for Chemical-analysis Systems - A Look Into Next Century Technology or Just A Fashionable Craze, *TrAC. Trends Anal. Chem.*, **1991**, *10*, 144-149.

[142] Kovacs, G. T. A., Petersen, K. and Albin, M., Silicon Micromachining - Sensors to Systems, *Anal. Chem.*, **1996**, *68*, A407-A412.

[143] Erickson, D. and Li, D. Q., Integrated Microfluidic Devices, *Anal. Chim. Acta.*, **2004**, *507*, 11-26.

[144] Lin, Y. H., Wu, H., Timchalk, C. A. and Thrall, K. D., Integrated Microfluidics/electrochemical Sensor System for Monitoring of Environmental Exposures to Toxic Chemicals. *Abstracts of Papers of the American Chemical Society*, **2002**, *223*, U77.

[145] Wang, J., Electrochemical Detection for Microscale Analytical Systems: A Review, *Talanta*, **2002**, *56*, 223-231.

[146] Rossier, J., Reymond, F. and Michel, P. E., Polymer Microfluidic Chips for Electrochemical and Biochemical Analyses, *Electrophoresis*, **2002**, *23*, 858-867.

[147] Wang, J., Electrochemical Detection for Capillary Electrophoresis Microchips: A review, *Electroanalysis*, **2005**, *17*, 1133-1140.

[148] Bange, A., Halsall, H. B. and Heineman, W. R., Microfluidic Immunosensor Systems, *Biosens. Bioelectron.*, **2005**, *20*, 2488-2503.

[149] Goral, V. N., Zaytseva, N. V. and Baeumner, A. J., Electrochemical Microfluidic Biosensor for the Detection of Nucleic Acid Sequences, *Lab Chip*, **2006**, *6*, 414-421.

[150] Sadik, O. A., Aluoch, A. O. and Zhou, A. L., Status of Biomolecular Recognition Using Electrochemical Techniques. *Biosens. Bioelectron.*, **2009**, *24*, 2749-2765.

[151] Swensen, J. S., Xiao, Y., Ferguson, B. S. and *et al.*, Continuous, Real-time Monitoring of Cocaine in Undiluted Blood Serum via a Microfluidic, Electrochemical Aptamer-based Sensor, *J. Am. Chem. Soc.*, **2009**, *131*, 4262-4266.

[152] Kraly, J. R., Holcomb, R. E., Guan, Q. and Henry, C. S., Review: Microfluidic Applications in Metabolomics and Metabolic Profiling, *Anal. Chim. Acta.*, **2009**, *653*, 23-35.

[153] Dungchai, W., Chailapakul, O. and Henry, C. S., Electrochemical Detection for Paper-based Microfluidics, *Anal. Chem.*, **2009**, *81*, 5821-5826.

[154] Jang, A., Zou, Z. W., Lee, K. K., Ahn, C. H. and Bishop, P. L., State-of-the-art Lab Chip Sensors for Environmental Water Monitoring, *Meas. Sci. Technol.*, **2011**, *22*, 032001.

[155] Fragoso, A., Latta, D., Laboria, N. and *et al.*, Integrated Microfluidic Platform for the Electrochemical Detection of Breast Cancer Markers in Patient Serum Samples, *Lab Chip*, **2011**, *11*, 625-631.

[156] Hebert, N. E., Kuhr, W. G. and Brazill, S. A., Microchip Capillary Electrophoresis Coupled to Sinusoidal Voltammetry for the Detection of Native Carbohydrates, *Electrophoresis*, **2002**, *23*, 3750-3759.

[157] Zhan, W., Alvarez, J. and Crooks, R. M., A Two-channel Microfluidic Sensor that Uses Anodic Electrogenerated Chemiluminescence as a Photonic Reporter of Cathodic Redox Reactions, *Anal. Chem.*, **2003**, *75*, 313-318.

[158] Zou, Z. W., Kai, J. H., Rust, M. J., Han, J. and Ahn, C. H., Functionalized Nano Interdigitated Electrodes Arrays on Polymer with Integrated Microfluidics for Direct Bio-affinity Sensing Using Impedimetric Measurement, *Sens. Actuators, A*, **2007**, *136*, 518-526.

[159] Lorenz, H., Despont, M., Fahrni, N. and *et al.*, SU-8: A Low-cost Negative Resist for MEMS, *J. Micromech. Microeng.*, **1997**, *7*, 121-124.

[160] Castano-Alvarez, M., Fernandez-Abedul, M. T., Costa-Garcia, A. and *et al.*, Fabrication of SU-8 Based Microchip Electrophoresis with Integrated Electrochemical Detection for Neurotransmitters, *Tantala*, **2009**, *80*, 24-30.

[161] Liu, X., Barizuddin, S., Shin, W. and *et al.*, Microwell Device for Targeting Single Cells to Electrochemical Microelectrodes for High-throughput Amperometric Detection of Quantal Exocytosis, *Anal. Chem.*, **2011**, *83*, 2445-2451.

[162] Ferguson, B. S., Buchsbaum, S. F., Swensen, J. S. and *et al.*, Integrated Microfluidic Electrochemical DNA Sensor, *Anal. Chem.*, **2009**, *81*, 6503-6508.

[163] Rassaei, L., Mathwig, K., Goluch, E. D. and Lemay, S. G., Hydrodynamic Voltammetry with Nanogap Electrodes, *J. Phys. Chem. C*, **2012**, *116*, 10913-10916.

[164] Wang, C., Li, S. J., Wu, Z. Q. and *et al.*, Study on the Kinetics of Homogeneous Enzyme Reactions in a Micro/nanofluidics Device, *Lab Chip*, **2010**, *10*, 639-646.

[165] Plecis, A., Schoch, R. B. and Renaud, P., Ionic Transport Phenomena in Nanofluidics: Experimental and Theoretical Study of the Exclusion-enrichment Effect on A Chip, *Nano Lett.*, **2005**, *5*, 1147-1155.

[166] Branagan, S. P., Contento, N. M. and Bohn, P. W., Enhanced Mass Transport of Electroactive Species to Annular Nanoband Electrodes Embedded in Nanocapillary Array Membranes, *J. Am. Chem. Soc.*, **2012**, *134*, 8617-8624.

[167] Shinwari, M. W., Zhitomirsky, D., Deen, I. A., and *et al.*, Microfabricated Reference Electrodes and Their Biosensing Applications, *Sensors*, **2010**, *10*, 1679-1715.

[168] Suzuki, H., Shiroishi, H., Sasaki, S. and Karube, I., Microfabricated Liquid Junction Ag/AgCl Reference Electrode and Its Application to a One-chip Potentiometric Sensor, *Anal. Chem.*, **1999**, *71*, 5069-5075.

[169] Huang, I. Y., Huang, R. S. and Lo, L. H., Improvement of Integrated Ag/AgCl Thin-film Electrodes by KCl-gel Coating for ISFET Applications, *Sens. Actuators, B*, **2003**, *94*, 53-64.

[170] Zhou, J. H., Ren, K. N., Zheng, Y. Z. and *et al.*, Fabrication of a Microfluidic Ag/AgCl Reference Electrode and Its Application for Portable and Disposable Electrochemical Microchips, *Electrophoresis*, **2010**, *31*, 3083-3089.

[171] Hassibi, A. and Lee, T. H., A Programmable 0.18-μm CMOS Electrochemical Sensor Microarray for Biomolecular Detection, *IEEE Sens. J.*, **2006**, *6*, 1380-1388.

[172] Zhu, X. S. and Ahn, C. H., On-chip Electrochemical Analysis System Using Nanoelectrodes and Bioelectronic CMOS Chip, *IEEE Sens. J.*, **2006**, *6*, 1280-1286.

[173] Li, L., Liu, X. W., Qureshi, W. A. and Mason, A. J., CMOS Amperometric Instrumentation and Packaging for Biosensor Array Applications, *IEEE T. Biomed. Circ. S.*, **2011**, *5*, 439-448.

[174] Huang, Y., Liu, Y., Hassler, B. L., Worden, R. M. and Mason, A. J., A Protein-based Electrochemical Biosensor Array Platform for Integrated Microsystems, *IEEE T. Biomed. Circ. S.*, **2013**, *7*, 43-51.

[175] Martin, S. M., Gebara, F. H., Larivee, B. J. and Brown, R. B., A CMOS-integrated Microinstrument for Trace Detection of Heavy Metals, *IEEE J. of Solid-State Circuits*, **2005**, *40*, 2777-2786.

[176] Swanson, P., Gelbart, R., Atlas, E. and *et al.*, A Fully Multiplexed CMOS Biochip for DNA Analysis, *Sens. Actuators, B*, **2000**, *64*, 22-30.

[177] Dill, K., Montgomery, D. D., Wang, W. and Tsai, J. C., Antigen Detection Using Microelectrode Array Microchips, *Anal. Chim. Acta*, **2001**, *444*, 69-78.

[178] Oleinikov, A. V., Gray, M. D., Zhao, J. and *et al.*, Self-assembling Protein Arrays Using Electronic Semiconductor Microchips and *in vitro* Translation, *J. Proteome. Res.*, **2003**, *2*, 313-319.

[179] Maurer, K., Cooper, J., Caraballo, M. and *et al.*, Electrochemically Generated Acid and Its Containment to 100 Micron Reaction Areas for the Production of DNA Microarrays, PLoS One, **2006**, *1*, e34.

[180] Dill, K., Montgomery, D. D., Ghindilis, A. L. and Schwarzkopf, K. R., Immunoassays and Sequence-specific DNA Detection on a Microchip Using Enzyme Amplified Electrochemical Detection, *J. Biochem. Biophys.*, **2004**, *69*, 181-187.

[181] Maurer, K., Yazvenko, N., Wilmoth, J., and *et al.*, Use of a Multiplexed CMOS Microarray to Optimize and Compare Oligonucleotide Binding to DNA Probes Synthesized or Immobilized on Individual Electrodes, *Sensors*, **2010**, *10*, 7371-7385.

[182] Martin, S. M., Strong, T. D. and Brown, R. B., Design, Implementation, and Verification of A CMOS-integrated Dhemical Sensor Ssystem. **2004** *International Conference on Mems, Nano and Smart Systems, Proceedings 379-385.*

[183] Huang, Y. and Mason, A. J., Lab-on-CMOS Integration of Microfluidics and Electrochemical Sensors, *Lab Chip*, **2013**, *13*, 3929-3934.

[184] Uddin, A., Milaninia, K., Chen, C. H. and Theogarajan, L., Wafer Scale Integration of CMOS Chips for Biomedical Applications *via* Self-aligned Masking, *IEEE Trans. Compon., Packag., Manuf. Technol*, **2011**, *1*, 1996-2004.

Chapter 3

Redox Couples with Unequal Diffusion Coefficients: Effect on Redox Cycling

Redox cycling between two electrodes separated by a narrow gap allows dramatic amplification of the faradaic current. Unlike conventional electrochemistry at a single electrode, however, the mass-transport-limited current is controlled by the diffusion coefficient of both the reduced and oxidized forms of the redox-active species being detected and, counter-intuitively, by the redox state of molecules in the bulk solution outside the gap itself. Using a combination of finite-element simulations, analytical theory and experimental validation, we elucidate the interplay between these interrelated factors. In so doing, we generalize previous results obtained in the context of scanning electrochemical microscopy and obtain simple analytical results that are generally applicable to experimental situations where efficient redox cycling takes place.

The contents of this chapter have been published as: Dileep Mampallil, Klaus Mathwig, Shuo Kang and Serge G. Lemay, Redox Couples with Unequal Diffusion Coefficients: Effect on Redox Cycling, *Anal. Chem.*, 2013, 85 (12), 6053–6058.

3.1 Introduction

In electrochemical detection at micro- and nanoelectrodes,[1, 2] where mass transport is commonly limited by diffusion, the measured current is proportional to the diffusion coefficient of the analyte species. This relationship can however become complex in redox cycling between two electrodes[3–6] due to unequal diffusivities of the oxidized and reduced forms of the analyte. This can influence both transient[7–11] and steady-state[12–14] behavior of the current. It is therefore crucial to understand the effect of unequal diffusivities of the oxidized and the reduced species for a quantitative interpretation of redox-cycling measurements.

A well-studied case is scanning electrochemical microscopy (SECM).[15–17] Due to unequal diffusivities, the steady-state current in SECM depends on the mode of operation:[8] interchanging the potentials of the tip and the substrate, i.e., switching between the feedback mode[7, 18, 19] and the substrate generation/tip collection (SG/TC) mode,[8, 20, 21] changes the steady-state current by a factor equal to the ratio of the diffusivities of the oxidized and the reduced species. Martin and Unwin[7, 8] performed a detailed numerical study of these effects supported by experiments for the SECM geometry (a shrouded disk microelectrode in close proximity to a planar substrate). This geometry has the particular feature that the bias of the substrate (reducing or oxidizing) also determines the species present in the "bulk" solution surrounding the microelectrode. For example, if the substrate is biased at an oxidizing potential, then the solution in the region surrounding the microelectrode, which is part of the one-dimensional diffusion zone generated by the substrate electrode, becomes essentially fully oxidized over time, independently of whether reduced or oxidized molecules were present in the original solution. This property was exploited in the experiments of Martin and Unwin to create a "bulk" solution of oxidized species. More recently, several experiments have started focusing on experimental geometries where this coupling between one of the electrodes and bulk does not exist. These include for example experiments where the conducting substrate is limited in extent, as studied by Zoski *et al.*[22] and more recently by Oleinick *et al.*,[23] as well as microfabricated nanogap devices that are only weakly coupled to bulk solution, as investigated by our group.[24] In these situations, the nature of the bulk solution and the polarity of the electrode biases can be independently controlled, in which case conclusions of Ref. [7] and [8] may not directly apply.

Here we investigate this question using nanogap devices,[24] in which the active region where redox cycling takes place is only weakly coupled to a bulk reservoir. This allows us to study independently the effect of switching the modes of operation and the influence of the species in the bulk. We observe that it is not the mode of operation but rather the redox state of the species in the bulk solution that controls the current during redox cycling. By using straightforward theoretical arguments, which are further supported by numerical calculations, we

quantitatively explain these experimental findings.

This chapter is organized as follows. We first present numerical simulations based on diffusive mass transport and the detailed specific geometry relevant in our experiments. We then derive analytical expressions for the diffusion-limited current that reproduce the full numerical result. These relatively simple expressions are more general than the numerical results in that they also apply to other geometries. Finally, we validate both numerical and analytical results through direct comparison with experiments.

3.2 Numerical model

We consider a simple outer-sphere heterogeneous electron-transfer reaction at the electrodes, $\mathrm{O} + ne \rightleftharpoons \mathrm{R}$, where n is the number of electrons transferred. Following the approach of Martin and Unwin,[7, 8] we numerically evaluate the diffusion-limited current under redox-cycling conditions for the general case where the diffusion coefficients for the reduced and the oxidized forms of a redox couple (D^R and D^O, respectively) have different values. We assume that the supporting electrolyte concentration is much greater than that of the redox species. Under these conditions, steady-state mass transport obeys the diffusion equation

$$\nabla^2 C^{R,O} = 0 \tag{3.1}$$

where C^R and C^O represent the concentrations of the reduced and the oxidized forms, respectively. The corresponding fluxes are given by

$$j^{R,O} = -D^{R,O} \nabla C^{R,O} \tag{3.2}$$

We solved Equation 3.1 for both R and O using a finite-element simulation (COMSOL Multiphysics 4.2), as reported earlier.[25] The simulation was performed over a two-dimensional domain representing the geometry and dimensions of the nanogap devices employed in our experiments, as sketched in Figure 3.1.

In short, the devices consist of two electrodes separated by a distance $z = 60$ nm. The top electrode has a length $L_E = 10$ μm and defines the so-called active region of the device. The active region is connected at both ends to outside reservoirs *via* nanochannels of length $L_A = 8$ μm and of the same height as the active region, z. The bottom electrode spans the entire length of the device, including both the active region and the access channel. Note that, importantly for the conclusions drawn below, the dimensions of the device satisfy the conditions $z \ll L_E, L_A$. For simplicity we assume that the electrodes span the whole width of the channel in the third (out of the page) dimension; the solution is then uniform in this third dimension and the simulations can be performed and

represented in only two dimensions. Boundary conditions corresponded to a high reducing overpotential at one electrode and a high oxidizing overpotential at the other electrode (reducing electrode: $C^O = 0$ and $j^R = -j^O$; oxidizing electrode: $C^R = 0$ and $j^O = -j^R$). The diffusion coefficients of the reduced and the oxidized molecules in aqueous solution were taken as $6.7{\times}10^{-10}\mathrm{m}^2/\mathrm{s}$ and $5.4{\times}10^{-10}\mathrm{m}^2/\mathrm{s}$, respectively, corresponding to the experimental conditions reported below and to a diffusion coefficient ratio $\gamma = D^O/D^R = 0.8$.[8] The concentrations in the bulk solution far from the entrances to the device, C_1^O and C_1^R, were treated as constant.

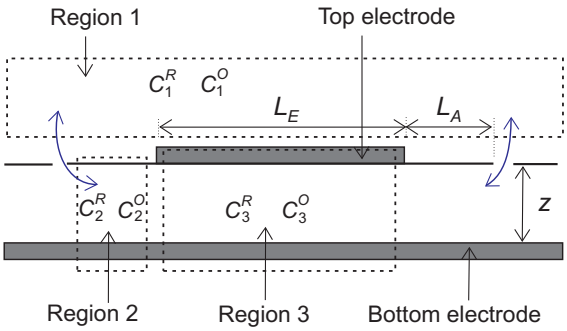

Figure 3.1: Schematic illustration of the device geometry employed for numerical simulations. Also shown are the three regions employed in analytical calculations: region 1, the bulk solution outside the device; region 2, the access channel without redox cycling; and region 3, the active region of the device where redox cycling takes place.

The results of the numerical simulations are summarized in Figure 3.2. We distinguish between four cases depending on whether the top or the bottom electrode is the reducing electrode and on whether the bulk solution contains only R ($C_1^R = C_B$, $C_1^O = 0$) or only O ($C_1^O = C_B$, $C_1^R = 0$).

Figure 3.2 a shows the two-dimensional concentration profiles $C^{R,O}(x, z)$ for the case where the bulk contains reduced species and the bottom electrode is oxidizing. Under these conditions, there exists a concentration gradient between the bulk solution and the access channel (regions 1 and 2 in Figure 3.1) since the bottom electrode oxidizes molecules from the bulk. There is also an approximately spherical concentration gradient extending into the bulk solution near each access hole of the device, but this lies outside the domain shown in Figure 3.2 a. In the access channel region, on the other hand, essentially all molecules are in the oxidized form due to the intimate contact with the bottom electrode. Finally, in the active region redox cycling causes steep gradients of both reduced and oxidized species between the electrodes. These gradients in the z-direction are essentially independent of x except for a short transition zone (length a few times z) at each end of the active region. Because $z \ll L_E$, this transition zone represents only a small perturbation on the total redox cycling flux.

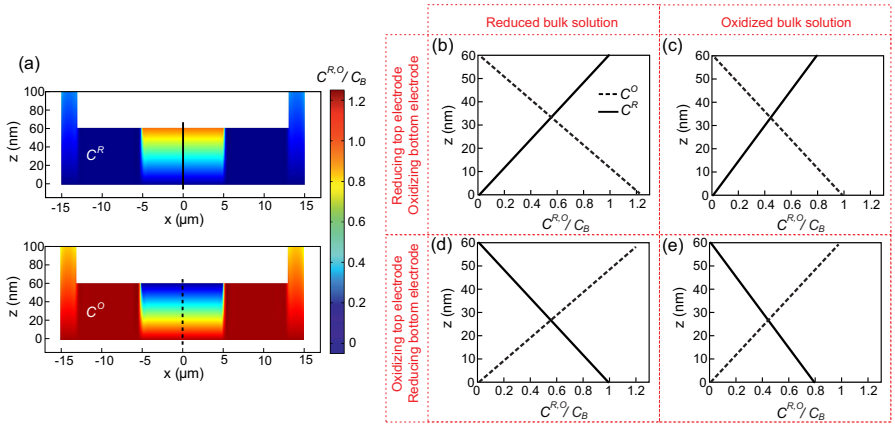

Figure 3.2: Results of numerical calculations. (a) Concentrations of R (top panel) and O (bottom panel) under steady-state conditions for the case where the bottom electrode is oxidizing, the top electrode reducing, and the bulk solution outside the device contains only R. The highly skewed aspect ratio is for clarity. (b-e) One-dimensional concentration profiles $C^{R,O}(x = 0, z)$ along the cross-section lines in panel (a). The cases where the top electrode is reducing and the bottom electrode is oxidizing are shown in the top row (panels b, c), while results for the opposite bias condition are shown in the bottom row (panels d, e). Both cases with reduced (panels b, d) and oxidized (panels c, e) species in the bulk reservoir are shown. All concentrations are normalized to the concentration of species in the reservoir, C_B.

Figure 3.2 b shows the one-dimensional concentration profiles $C^{R,O}(0, z)$ in the z-direction at a location halfway between the access holes (corresponding to the cross section lines in the active region in panel (a)). As required by the boundary conditions, the concentration of R is maximal at the reducing electrode and vanishes at the oxidizing electrode; the converse is true for O. Both concentration gradients are linear, reflecting the fact that, apart from a small region near the edges of the active region, the diffusion gradient is effectively one-dimensional between the electrodes. The maximum concentration of R is simply the bulk concentration, C_B, while the concentration of R averaged in the z-direction over the height of the device, which we denote by $\bar{C}_3^R$, is $C_B/2$. The concentration of O, on the other hand, is modified by a factor of $1/\gamma = 1.25$ compared to that of R, such that $\bar{C}_3^O = C_B/2\gamma$. This difference between $\bar{C}_3^R$ and $\bar{C}_3^O$ is dictated by the electrode boundary condition $j^R = -j^O$: since $j^{R,O} = \pm 2D^{R,O}\bar{C}_3^{R,O}/z$, this boundary condition reduces to

$$\bar{C}_3^O = \frac{D^R}{D^O}\bar{C}_3^R = \frac{\bar{C}_3^R}{\gamma} \tag{3.3}$$

It further follows from the above that the total concentration of redox species in the active region is given by $\bar{C}_3^R + \bar{C}_3^O = C_B(1 + 1/\gamma)/2$, which differs from the bulk concentration when $\gamma \neq 1$. This is possible because there exists a connection to the bulk reservoir and could not occur in a sealed volume. The total faradaic

current corresponding to Equation 3.3 is given by

$$i_{\text{lim}}^{R} = nFA|j^{R}| = nFA|j^{O}| = \frac{nFAD^{R}C_{B}}{z} \tag{3.4}$$

where F is the Faraday constant and A the area of overlap between the electrodes. This is the same result as if the diffusion coefficient for O had been ignored entirely; this is because the different speed of diffusion of O is compensated by the changes in concentration observed in Figgure 3.2.

Figure 3.2 c shows the R and O concentration profiles in the active region for a different case, namely, where the bulk solution is in the oxidized form instead of the reduced form. The profiles are qualitatively similar to those of panel (b), except that the concentrations are modified by a factor γ: we now observe $\bar{C}_3^O = C_B/2$ and $\bar{C}_3^R = \gamma C_B/2$. The corresponding change in gradients leads to a corresponding change in faradaic current,

$$i_{\text{lim}}^{O} = \frac{nFAD^{O}C_{B}}{z} = \gamma\ i_{\text{lim}}^{R} \tag{3.5}$$

Finally, Figure 3.2 d and 3.2 e show the corresponding profiles when the roles of the electrodes (reducing or oxidizing) are inverted. The only change in the concentration profiles is that they are inverted in the z direction, reflecting the inverted roles of the top and bottom electrodes; the magnitudes of the concentration gradients are unaffected. Correspondingly, the faradaic current is also unaffected. This indicates that it is the species present in the bulk that influences the diffusion-limited current rather than the choice of which electrode is reducing or oxidizing.

3.3 Analytical model

While useful for gaining a detailed understanding of the factors at play, results from numerical simulations are by their very nature obtained for a specific geometry and it is not necessarily clear how generally we can apply the conclusions drawn from a particular set of simulations. Here, armed with insights gained from the numerical study, we derive a simple analytical theory that reproduces the predictions of the simulations. Importantly, however, the derivation is independent of the specific geometry of the nanogap, so long as some simple pre-requisite conditions are satisfied. The analytical results can thus be employed for other redox cycling geometries without the need for additional numerical simulations for each case.

We first note that there exist three distinct regions in the system where the ratio of the concentrations of R and O is fixed, as illustrated in Figure 3.1. Region

1 consists in the bulk solution. Here the concentrations of R and O, C_1^R and C_1^O, respectively, are known by assumption. Region 2 consists of the part of the access channel far from both the active region and the access holes to bulk solution (where "far" signifies a distance of a few times the channel height, z). Here $C_2^O = \beta C_2^R$, where β is set by the potential of the bottom electrode; $\beta \to 0$ and $\beta \to \infty$ correspond to the bottom electrode being reducing or oxidizing, respectively. Finally, region 3 consists of the active region; here both $\bar{C}_3^R$ and $\bar{C}_3^O$ are finite during redox cycling, and their magnitudes are related by Equation 3.3.

Between these three regions, there exist transition zones (with a spatial extent of the order of z) where significant gradients in C^R and C^O can occur in the x-direction. For example, for the case of Figure 3.2 a, there is a diffusive flux of O from the access channels to the active region and a compensating flux of R in the opposite direction. Using the symbol J to represent the total flux integrated across the entire cross-section of the channel, this situation corresponds to $J_{2\to3}^O > 0$ and $J_{2\to3}^R < 0$. Under steady-state conditions, the total flux of redox molecules, either reduced or oxidized, must however vanish. Therefore,

$$J_{p\to q}^R + J_{p\to q}^O = 0 \tag{3.6}$$

where p, q represent any pair of adjacent reservoirs.

In order to determine explicit expressions for the fluxes $J_{p\to q}^{R,O}$ for diffusive transport between the various regions, it is necessary to solve the diffusion equation, Equation 3.1, for the specific geometry of interest. For our present purpose, however, it will prove sufficient that, without loss of generality, the expression for the total flux has the form[26]

$$J_{p\to q}^{R,O} = D^{R,O}(C_p^{R,O} - C_q^{R,O})\, b \tag{3.7}$$

here b is a geometry-dependent constant with the units of length. Importantly the value of b is independent of the diffusion coefficient or concentration; for a given geometry, its value is thus identical for R and O. Substituting Equation 3.7 into the steady-state condition, Equation 3.6, yields expressions relating the concentrations of R and O in region q to those in region p. Applying this procedure to the bulk solution (region 1) and the access channel (region 2) yields expressions for the concentrations in the access channel (averaged over the channel height)

$$\bar{C}_2^R = \frac{1}{1+\gamma\beta}\left(C_1^R + \gamma C_1^O\right) \tag{3.8}$$

and

$$\bar{C}_2^O = \frac{\beta}{1+\gamma\beta}\left(C_1^R + \gamma C_1^O\right) \tag{3.9}$$

Repeating the procedure between regions 2 and 3 and using Equation 3.8 and Equation 3.9 to eliminate $\bar{C}_2^R$ and $\bar{C}_2^O$ then yields the concentrations in the active

region in terms of those in the bulk,

$$\bar{C}_3^R = \frac{C_1^R + \gamma C_1^O}{2} \tag{3.10}$$

and

$$\bar{C}_3^O = \frac{C_1^R + \gamma C_1^O}{2\gamma} \tag{3.11}$$

Equation 3.10 and Equation 3.11 can be used to obtain $|j^R|$ and $|j^O|$, respectively. Following a similar procedure as in Equation 3.4, the corresponding diffusion-limited current is

$$i_{\lim} = \frac{nFA}{z}\left(D^R C_1^R + D^O C_1^O\right) = \frac{nFAD^R}{z}\left(C_1^R + \gamma C_1^O\right) \tag{3.12}$$

Interestingly, this result is independent of the parameter β characterizing the access channel; indeed, it can also be obtained by applying Equation 3.6 to regions 1 and 3 directly.

Equation 3.12 is valid for any mixture of R and O in the bulk solution; for the special cases of fully reduced ($C_1^R = C_B$ and $C_1^O = 0$) and fully oxidized ($C_1^R = 0$ and $C_1^O = C_B$) bulk solution, it reduces to Equation 3.4 and Equation 3.5, respectively. Importantly, the equation, since derived from Equation 3.7 is independent of the specific geometry and applies equally well to other systems where redox cycling takes place. The only requirements for its validity are that (1) the electrodes are much closer together than the lateral dimensions of the electrodes ($z \ll L_E$ in our particular geometry; $z \ll$ electrode radius for a shrouded disc electrode as in SECM), and (2) there is a sufficiently large overpotential that complete reduction or oxidation occurs at the two electrodes. Equation 3.12 is in this sense far more general than the results of the simulations of the previous section.

Finally, we note that, while the derivation above focused solely on the diffusion-limited current, it is straightforward to generalize it to the whole voltammogram so long as the heterogeneous reaction kinetics are reversible. The result in this case is simply that the whole voltammogram scales with C_1^R and C_1^O in the same manner as the limiting current, as described above. For the case of quasireversible kinetics, on the other hand, a more complex calculation would be required for values of the potential in the vicinity of the half-wave potential; such a calculation lies beyond the scope of the present work.

3.4 Experimental methods

Potassium chloride, ammonium persulphate ($(NH_4)_2S_2O_8$) and 1,1-ferrocene dimethanol were obtained from Sigma-Aldrich in analytical grade and used without further purification. Chromium etchant was obtained commercially from

Transene Co. Inc. Deionized and filtered water was obtained from a Milli-Q Advantage ultrapure water system. 1 M KCl (Sigma-Aldrich) was used as supporting electrolyte.

To prepare solutions with fully oxidized redox species, 50 μL of 100 mM $(NH_4)_2S_2O_8$ was added to 10 ml of a 1 mM 1,1-ferrocene dimethanol aqueous solution purged with nitrogen for 10 min. Cyclic voltammetry at an ultramicroelectrode was employed to verify that the solution was fully oxidized.

The nanogap device (as shown in Figure 3.3) was fabricated on a silicon substrate employing techniques reported previously[24, 27] except that photolithography was employed instead of electron-beam lithography. The fabricated devices contained two Pt electrodes separated by a Cr sacrificial layer of thickness 60 nm. The bottom electrode was 3 μm in width and 34 μm in length. The top electrode was 9 μm in width and 10 μm in length. The active region of the device was defined as the volume encompassed by the overlapping top and bottom electrodes (3 μm $\times$ 10 μm $\times$ 60 nm). The access holes were located at the top of the device, 8 μm away from the ends of the top electrode. Directly before the measurements, the sacrificial layer was chemically removed using a wet chromium etch at room temperature, thus forming the nanochannel. The etching procedure was monitored electrically by measuring the resistance between the top and bottom electrodes.

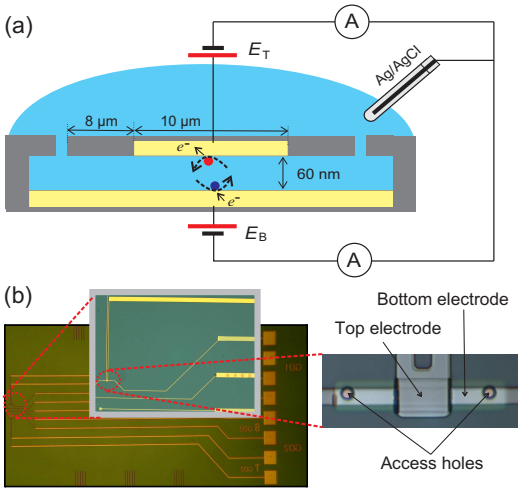

Figure 3.3: (a) Schematic diagram of the experimental configuration. (b) Top view optical images of a device with the zoomed in part showing the nanogap region.

Electrochemical experiments in the nanogap devices were performed with two Keithley 6430 sub-femtoampere source meters used both as voltage sources to bias the electrode potentials and as current meter. The Keithley instruments were

controlled remotely using custom Labview code. Electrochemical measurements using a polished carbon ultra micro electrode (UME) of radius 5.5 μm (BASi MF-2007) were performed with a bipotentiostat (CHI832B, CH Instruments). For all the measurements the potentials were applied with respect to a 3 M Ag/AgCl reference electrode (BASi). No auxiliary electrode was used in either case due to the low current level through the reference electrode. All the experiments were carried out at room temperature (21 $\pm$ 2 °C).

3.5 Experimental results

The measurement started with the cyclic voltammetry of the 1,1-ferrocene dimethanol solution using a carbon UME, as shown in Figure 3.4 (black curve). The electrode potential was swept between 0 and 0.5 V *vs.* Ag/AgCl and a sigmoidal oxidation wave was observed with half wave potential $E^{0'} = 0.24$ V, as expected for 1,1-ferrocene dimethanol. The corresponding voltammorgram for 1,1-ferrocene dimethanol in the oxidized form is also shown in Figure 3.4 (red curve), where a reduction wave is now observed. The limiting currents for the cases of bulk solution with R (black curve) and O (red curve) species are proportional to D^R and D^O, respectively. Therefore, the ratio of the wave heights of the two curves in Figure 3.4 gives the diffusivity ratio, $\gamma = D^O/D^R$. Our data yield $\gamma = 0.80 \pm 0.01$, which is closely comparable to the values reported in the literature.[8]

Immediately following the UME experiments, we performed measurements in nanogap devices using the same solutions. The devices were filled with solution containing only reduced species. The top electrode was scanned from 0 to 0.5 V *vs.* Ag/AgCl while keeping the bottom electrode at a reducing potential (0 V) or an oxidizing potential (0.5 V). The former configuration corresponds to the feedback mode and the latter to the SG/TC mode in SECM. The measured voltammograms for the two scanning modes are shown in Figure 3.5 (black curves). The figure includes voltammograms for both the top and the bottom electrodes; the curves are essentially identical except for a sign reversal in the current, as expected for redox cycling. Contrary to SECM studies,[7, 8] the limiting current is independent of which electrode is reducing or oxidizing. As discussed above, we attribute this difference to the fact that here the coupling between the bottom electrode and the bulk reservoir is weak enough that the composition of the bulk remains essentially unaffected by reactions taking place in the nanogap device.

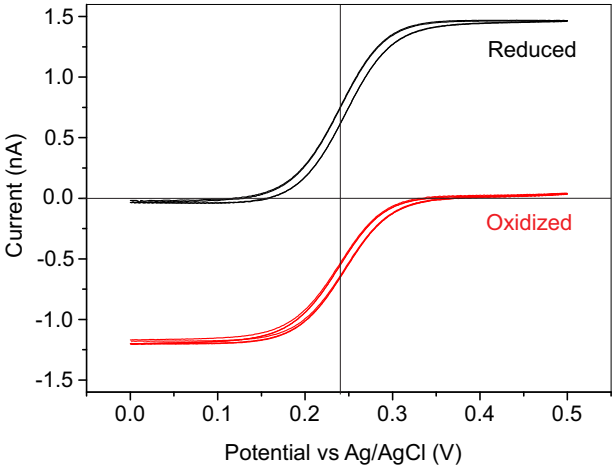

Figure 3.4: Cyclic voltammograms using a carbon UME for 1,1-ferrocene dimethanol solution in the reduced form (black curve) and the oxidized form (red curve). The ratio of the limiting currents in the two voltammograms yields the ratio of the diffusion coefficients, $\gamma = D^O/D^R$. Scan rate 20 mV/s.

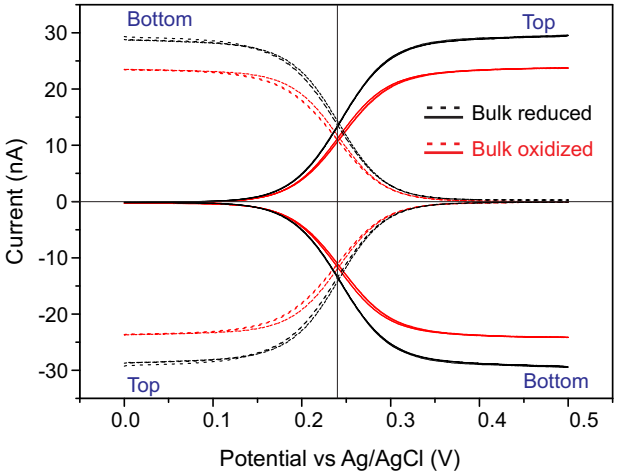

Figure 3.5: Cyclic voltammograms for a nanogap device. The bottom electrode is kept at a reducing (solid lines) or oxidizing (dashed lines) potential while the top electrode is swept. The solution in the bulk solution outside the device contained 1,1-ferrocene dimethanol in either the reduced (black lines) or oxidized (red lines) form. The current at both electrodes is shown for each case, as identified by the labels 'Top' and 'Bottom'. The limiting current is independent of which electrode is reducing or oxidizing, but is systematically lower by a factor 0.83±0.03 when the bulk solution is in the oxidized form (red lines). Scan rate 20 mV/s.

The same set of experiments was repeated using the solution containing ferrocene in the oxidized form. The measured curves are also shown in Figure 3.5 (red curves). Again, the steady-state current is independent of choice of which electrode is reducing or oxidizing, that is, of the mode of operation. The limiting current is however decreased compared to the case with reduced molecules in the bulk solution (black curves) in a manner reminiscent of the UME measurements. The measured ratio of the limiting currents for the two cases is 0.83 ± 0.03. Equation 3.4 and Equation 3.5 predict that this ratio should correspond to the diffusivity ratio, γ. This is fully consistent with the value of this ratio determined from the UME measurements, $\gamma = 0.80 \pm 0.01$.

3.6 Summary

In summary, we have derived a general expression, Equation 3.12, for the diffusion limited current in redox cycling. We have shown theoretically that Equation 3.12 is valid for any mixture of R and O species in the bulk solution and independent of the geometry of the redox cycling device. Our theoretical results indicate that the diffusion-limited current is influenced by the redox state of the species in the surrounding bulk solution and not by the choice of which electrode is reducing or oxidizing. These predictions were tested experimentally using microfabricated nanogap electrodes and good quantitative agreement was found. Our results provide a straightforward way of eliminating possible systematic errors due to unequal diffusion coefficients in a broad range of redox cycling systems.

For the specific case of the SECM configuration, it was instead reported earlier that the choice of which electrode is reducing or oxidizing influences the current.[7, 8] There is no contradiction with the present conclusions, however, since in the SECM case the contents of the "bulk" solution near the tip electrode is determined by the bias of the macroscopic working electrode and is not an independently controlled parameter as in the general case discussed here.

References

[1] Privett, B. J., Shin, J. H. and Schoenfisch, M. H., Electrochemical Sensors, *Anal. Chem.*, **2010**, *82*, 4723-4741.

[2] Kimmel, D. W., Leblanc, G., Meschievitz, M. E. and Cliffel, D. E., Electrochemical Sensors and Biosensors, *Anal. Chem.*, **2012**, *84*, 685-707.

[3] Bard, A. J., Mirkin, M. V., Unwin, P.R. and Wipf, D. O., Scanning Electrochemical Microscopy. 12. Theory and Experiment of the Feedback Mode with Finite Heterogeneous Electron-Transfer Kinetics and Arbitrary Substrate Size, *J. Phys. Chem.*, **1992**, *96*, 1861-1868.

[4] Niwa, O., Xu, Y., Halsall, H. B. and Heineman, W. R., Small-Volume Voltammetric Detection of 4-Aminophenol with Interdigitated Array Electrodes and Its Application to Electrochemical Enzyme-Immunoassay, *Anal. Chem.*, **1993**, *65*, 1559-1563.

[5] Schienle, M., Paulus, C., Frey, A., Hofmann, F., Holzapfl, B., Schindler-Bauer, P. and Thewes, R., A Fully Electronic DNA Sensor With 128 Positions and in-pixel A/D Conversion, *IEEE J. Solid-St. Circ.*, **2004**, *39*, 2438-2445.

[6] Kätelhön, E., Hofmann, B., Lemay, S. G., Zevenbergen, M. A. G., Offenhäusser, A., and Wolfrum, B., Nanocavity Redox Cycling Sensors for the Detection of Dopamine Fluctuations in Microfluidic Gradients, *Anal. Chem.*, **2010**, *82*, 8502-8509.

[7] Martin, R.D. and Unwin, P. R., Scanning Electrochemical Microscopy: Theory and Experiment for the Positive Feedback Mode with Unequal Diffusion Coefficients of the Redox Mediator Couple, *J. Electroanal. Chem.*, **1997**, *439*, 123-136.

[8] Martin, R. D. and Unwin, P. R., Theory and Experiment for the Substrate Generation Tip Collection Mode of the Scanning Electrochemical Microscope:

Application as an Approach for Measuring the Diffusion Coefficient Ratio of a Redox Couple, *Anal. Chem.*, **1998**, *70*, 276-284.

[9] Amatore, C., Sella, C. and Thouin, L., Diffusional Cross-talk Between Paired Microband Electrodes Operating within a Thin Film: Theory for Redox Couples with Unequal Diffusion Coefficients, *J. Phys. Chem. B*, **2002**, *106*, 11565-11571.

[10] Zoski, C. G., Luman, C. R., Fernández, J. L. and Bard, A. J., Scanning Electrochemical Microscopy. 57. SECM Tip Voltammetry at Different Substrate Potentials under Quasi-steady-state and Dteady-state Conditions, *Anal. Chem.*, **2007**, *79*, 4957-4966.

[11] Ghilane, J., Lagrost, C. and Hapiot, P.,Scanning Electrochemical Microscopy in Nonusual Solvents: Inequality of Diffusion Coefficients Problem, *Anal. Chem.*, **2007**, *79*, 7383-7391.

[12] Oldham, K. B., Effect of Diffusion Coefficient Diversity on Steady-state Voltammetry When Homogeneous Equilibria and Migration are Encountered, *Anal. Chem.*, **1996**, *68*, 4173-4179.

[13] Hyk, W. and Stojek, Z., Generalized Theory of Steady-state Voltammetry Without a Supporting Electrolyte. Effect of Product and Substrate Diffusion Coefficient Diversity, *Anal. Chem.*, **2002**, *74*, 4805-4813.

[14] Hyk, W. and Stojek, Z., General Theory for Migrational Voltammetry. Strong Influence of Diversity in Redox Species Diffusivities on Charge Reversal Electrode Processes, *Anal. Chem.*, **2005**, *77*, 6481-6486.

[15] Bard, A. J., Fan, F. R. F., Kwak, J. and Lev, O., Scanning Electrochemical Microscopy - Introduction and Principles, *Anal. Chem.*, **1989**, *61*, 132-138.

[16] Kwak, J. and Bard, A. J., Scanning Electrochemical Microscopy - Theory of the Feedback Mode, *Anal. Chem.*, **1989**, *61*, 1221-1227.

[17] Bard, A.J., Fan, F. R. F., Pierce, D. T., Unwin, P. R., Wipf, D. O. and Zhou, F., Chemical Imaging of Surfaces with the Scanning Electrochemical Microscope, *Science*, **1991**, *254*, 68-74.

[18] Lee, C., Kwak, J. and Anson, F. C., Application of Scanning Electrochemical Microscopy to Generation/Collection Experiments with High Collection Efficiency, *Anal. Chem.*, **1991**, *63*, 1501-1504.

[19] Amemiya, S., Bard, A. J., Fan, F. R. F., Mirkin, M. V. and Unwin, P. R., Scanning Electrochemical Microscopy, *Annu. Rev. Anal. Chem.*, **2008**, *1*, 95-131.

[20] Engstrom, R. C., Meaney, T., Tople, R. and Wightman, R. M., Spatiotemporal Description of the Diffusion Layer with a Microelectrode Probe, *Anal. Chem.*, **1987**, *59*, 2005-2010.

[21] Martin, R. D. and Unwin, P. R., Scanning Electrochemical Microscopy - Kinetics of Chemical Reactions Following Electron-transfer Measured with the Substrate-generation-tip-collection Mode, *J. Chem. Soc., Faraday Trans.*, **1998**, *94*, 753-759.

[22] Zoski, C. G., Simjee, N., Guenat, O. and Koudelka-Hep, M., Addressable Microelectrode Arrays: Characterization by Imaging with Scanning Electrochemical Microscopy, *Anal. Chem.*, **2004**, *76*, 62-72.

[23] Oleinick, A. I., Battistel, D., Daniele, S., Svir, I. and Amatore, C., Simple and Clear Evidence for Positive Feedback Limitation by Bipolar Behavior during Scanning Electrochemical Microscopy of Unbiased Conductors, *Anal. Chem.*, **2011**, *83*, 4887-4893.

[24] Zevenbergen, M. A. G., Krapf, D., Zuiddam, M. R. and Lemay, S. G., Mesoscopic Concentration Fluctuations in a Fluidic Nanocavity Detected by Redox Cycling, *Nano Lett.*, **2007**, *7*, 384-388.

[25] Rassaei, L., Mathwig, K., Goluch, E. D. and Lemay, S. G., Hydrodynamic Voltammetry with Nanogap Electrodes, *J. Phys. Chem. C*, **2012**, *116*, 10913-10916.

[26] Singh, P. S., Goluch,E. D., Heering, H. A. and Lemay, S. G., *Applications of Electrochemistry and Nanotechnology in Biology and Medicine II, volume 53 of Modern Aspects of Electrochemistry*, N. Eliaz ed. (Springer, **2012**), 1 - 66.

[27] Zevenbergen, M. A. G., Wolfrum, B. L., Goluch, E. D., Singh, P. S. and Lemay, S. G., Fast Electron-Transfer Kinetics Probed in Nanofluidic Channels, *J. Am. Chem. Soc.*, **2009**, *131*, 11471-11477.

Chapter 4

Response Time of Nanofluidic Electrochemical Sensors

Nanofluidic thin-layer cells count among the most sensitive electrochemical sensors built to date. Here we study both experimentally and theoretically the factors that limit the response time of these sensors. We find that the key limiting factor is reversible adsorption of the analyte molecules to the surfaces of the nanofluidic system, a direct consequence of its high surface-to-volume ratio. Our results suggest several means of improving the response time of the sensor, including optimizing the device geometry and tuning the electrode biasing scheme so as to minimize adsorption.

The contents of this chapter have been published as: Shuo Kang, Klaus Mathwig and Serge G. Lemay, Response Time of Nanouidic Electrochemical Sensors, *Lab Chip*, 2012, 12, 1262–1267.

4.1 Introduction

Electrochemical (bio)sensors with increasingly complex geometries are being created for integration into lab-on-a-chip systems.[1–4] One particularly promising approach is so-called redox cycling, in which analyte molecules are repeatedly oxidized and reduced at multiple, closely-spaced electrodes. The amplification of faradaic currents inherent to redox cycling can yield important gains in sensitivity and selectivity, while at the same time reducing the volume of sample needed for analysis.[5–7] A key performance criterion for electrochemical (bio)sensors is speed: for example, the response time of modern commercialized blood glucose meters is typically below 15 seconds.[8] The factors limiting the response time of "classic" thin-layer cells and the transient response of redox cycling devices have been studied.[9–11] Additional factors that may be relevant in nanoscale redox cycling devices have however not been explored in detail to date.

Here we present measurements as well as a theoretical analysis of the chronoamperometric transient response of nanoscale redox cycling sensors. Our measurements employ nanogap transducers, which consist of two parallel, closely spaced electrodes separated by a thin (70 nm) liquid-filled channel. By virtue of their geometry, these devices exhibit some of the highest levels of redox cycling amplification reported to date.[12] Surprisingly, we find that the response time of this type of sensor is predominantly limited by adsorption of the redox species onto the channel and electrode surfaces. This increased role for adsorption is a direct consequence of the high surface-to-volume ratio inherent to nanofluidic devices. These results suggest several methods for improving the response time of the devices. Our conclusions are also applicable to other miniaturized electrochemical sensor configurations, especially those based on redox cycling.

4.2 Experimental

4.2.1 Nanofluidic devices

Nanogap sensors were fabricated as described previously,[12] except that optical lithography was used to define all the structures instead of electron-beam lithography. In brief, on a 4-inch Si wafer isolated with 500 nm thick thermally grown SiO_2, a 20 nm thick Pt bottom electrode, a 60 nm thick Cr sacrificial layer and a 100 nm thick Pt top electrode were sequentially deposited by electron-beam evaporation and patterned using a lift-off process based on a positive photoresist (OIR 907-17, Arch Chemicals). Afterwards, a passivation layer consisting of 90 nm/325 nm/90 nm thick PECVD SiO_2/SiN/SiO_2 was deposited. Access holes were then etched through the passivation layer in a RIE etcher, reaching the Cr sacrificial layer. Finally, the sacrificial layer was etched by immersing the device in Cr

etchant, creating a nanochannel. Figure 4.1 a shows schematic cross-sections of the devices.

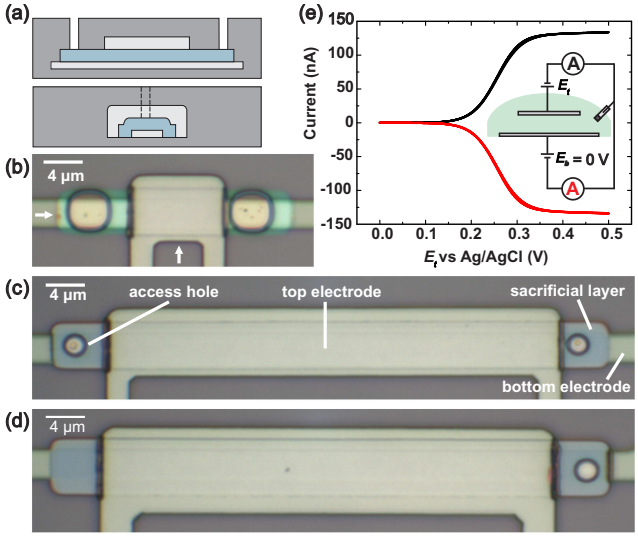

Figure 4.1: Schematic device cross-sections along the longitudinal axis (top) and transverse axis (bottom) at the stage prior to Cr etching (not drawn to scale). (b) Optical microscope top view image of device of type L10H2, in which the sacrificial Cr layer has been etched; the arrows indicate the lines corresponding to the schematic cross-sections in (a). (c) and (d) Devices of type L50H2 and L50H1, respectively, prior to Cr etching. (e) Cyclic voltammetry of a device of type L50H2 filled with 1 mM $Fc(MeOH)_2$ and 1M KCl with the potential of the top electrode, E_t, being swept while the potential of the bottom electrode, E_b, was held at 0V.

Three designs with different geometries were employed, as shown in Figure 4.1 (b)-(d). In short, devices of type L10H2 had a 10μm long detection region with access holes for samples located at both ends of the detection region. Devices of type L50H2 were essentially identical to type L10H2, except that they had a longer (50 μm) active region. Finally, devices of type L50H1 were identical to type L50H2 except that they had only a single access hole located at one end of the active region; the other end of the active region was blocked. Detailed dimensions for the three designs are given in Table 4.1.

4.2.2 Electrical measurements

Multi-potential-step chronoamperometry measurements were performed with two Keithley 6430 sub-femtoamp remote sourcemeters (Keithley Instruments) that were controlled with in-house LabVIEW software. A standard Ag/AgCl electrode (3M NaCl, BASi) served both as reference and counter electrode. This

Device name	L10H2	L50H2	L50H1
Length of top electrode (μm)	10	50	50
Width of top electrode (μm)	5	5	6
Width of bottom electrode (μm)	3	3	3
Number of access holes	2	2	1
Size of access holes[a] (μm $\times$ μm)	4×4	2×2	2×2
Distance of the access holes from the edge of the top electrode[b] (μm)	2	2	2

[a]The corners of the access holes become rounded during lithography.

[b]There is some random offset in the real devices compared to the mask design due to the alignment tolerance in lithography.

Table 4.1: Dimensions of the three types of devices used in this study.

configuration is appropriate since the current flowing through the reference electrode is negligibly small.[12] The reference electrode was immersed in a PDMS reservoir with an opening at the bottom that contacted the device.

4.2.3 Chemicals

Potassium chloride, KCl, was purchased from Sigma-Aldrich (cat. no.P3911), and Ferrocenedimethanol, $Fc(MeOH)_2$, from Acros (cat. no. 382550010). The chromium etchant (Selectipur) was from BASF and the sulphuric acid, H_2SO_4, from Sigma-Aldrich (cat. no. 339741). All chemicals were used as received and the solutions were prepared using 18.2 MΩ cm MilliQ water.

4.2.4 Electrode cleaning

Prior to electrochemical measurements, the devices were cleaned by filling with a solution of 0.5 M H_2SO_4 and repeatedly sweeping the electrode between -0.15 V and 1.15 V *vs.* Ag/AgCl until a reproducible voltammogram was obtained.

4.3 Results and discussion

The basic operation of a device of type L50H2 is illustrated in Figure 4.1 e, which shows a cyclic voltammogram in the presence of 1 mM $Fc(MeOH)_2$ and 1M

KCl as supporting electrolyte. The steady-state oxidation current collected at the top electrode is equal and opposite to the reduction current collected at the bottom electrode, as expected for redox cycling. Because the kinetics of $Fc(MeOH)_2$ are essentially reversible under the present conditions,[12] the magnitude of the steady-state current, i_{ss}, is simply given by diffusive mass transport combined with the Nernst equation,[13]

$$i_{ss} = \frac{nFADc_b}{z}\left(\frac{1}{1+e^{-f\eta_t}}\right) \tag{4.1}$$

here n represents the number of electrons transferred per molecule (n=1 for $Fc(MeOH)_2$), F the Faraday constant, A the overlap area between top and bottom electrode, D the diffusion coefficient (5.6×10^{-6}cm^2/s for $Fc(MeOH)_2$)*, c_b the bulk concentration of the redox species, $f = F/RT$ with R the gas constant and T the absolute temperature, $\eta_t = E_t\text{-}E^{0'}$ the overpotential applied to the top electrode, and z the distance between the two electrodes. The latter has a value $z = 70$ nm, as deduced from the diffusion-limited steady-state current at high overpotential ($f\eta_t >> 1$). This is slightly higher than the thickness of the sacrificial Cr layer (60 nm), which we attribute to slight buckling of the top electrode after the sacrificial Cr layer was etched.

4.3.1 Multi-potential-step chronoamperometry

To investigate the transient response of the devices, we filled a device with an aqueous solution of 1 mM $Fc(MeOH)_2$ and 1M KCl as supporting electrolyte. We then applied a series of step-wise perturbations to the biasing potential of one of the electrodes while holding the potential of the other electrode fixed. The resulting electrochemical current response was measured as a function of time. For example, Figure 4.2 a shows the potentials applied to the two electrodes of a device of type L50H2; the potential of the bottom electrode was kept at 0 V while the top electrode was stepped at regular intervals. The resulting current-time response is shown in Figure 4.2 b.

Each time that the voltage applied to the top electrode was stepped, the redox cycling current suddenly jumped to a different value, then gradually settled to a new steady-state current. This new steady-state current corresponded to the value i_{ss} given by Equation 4.1, as expected. Importantly, however, increasing the voltage typically caused the current to initially jump to a value lower than i_{ss}, a counterintuitive behaviour that cannot be predicted from inspection of the steady-state voltammogram. Conversely, stepping the potential downward typically caused an initial increase in the current. Furthermore, the duration of the

*Determined from the diffusion-limited current at a 5 μm radius platinum ultramicroelectrode.

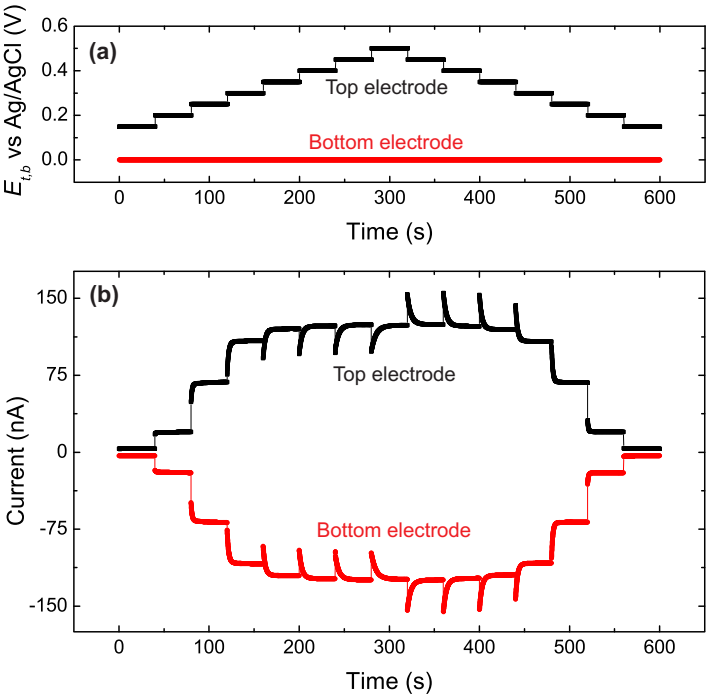

Figure 4.2: Multi-potential-step chronoamperometry of a device of type L50H2 filled with an aqueous solution of 1 mM $Fc(MeOH)_2$ and 1 M KCl as supporting electrolyte. (a) Potentials applied as a function of time to the top (black) and bottom (red) electrode. (b) Corresponding current-time response.

transient was longer for more positive potentials at the top electrode, indicating that the dynamic response of the device is limited by a potential-dependent effect.

To better quantify this potential dependence, a modified multi-potential-step chronoamperometry measurement was carried out in which the potential of the bottom electrode was kept at 0 V while a sequence of potential steps was applied to the top electrode, as shown in Figure 4.3 a. Before each step, the potential of the top electrode was returned to 0 V so as to initialize the device to the same state. The corresponding amperometric response is illustrated in Figure 4.3 b (a similar experiment in which the bottom electrode was kept at 0.5 V, an oxidizing potential, instead of 0 V, a reducing potential, is shown in Appendix A). No current flowed in the "initialization" stages where both top and bottom electrodes were biased at 0 V, as expected. When the potential of the top electrode was stepped up, the current first jumped to a finite value, then continued to increase gradually until the steady-state current i_{ss} was approached. Higher potentials resulted in longer transients and larger departures of the current from its steady-state value in the early part of the transients.

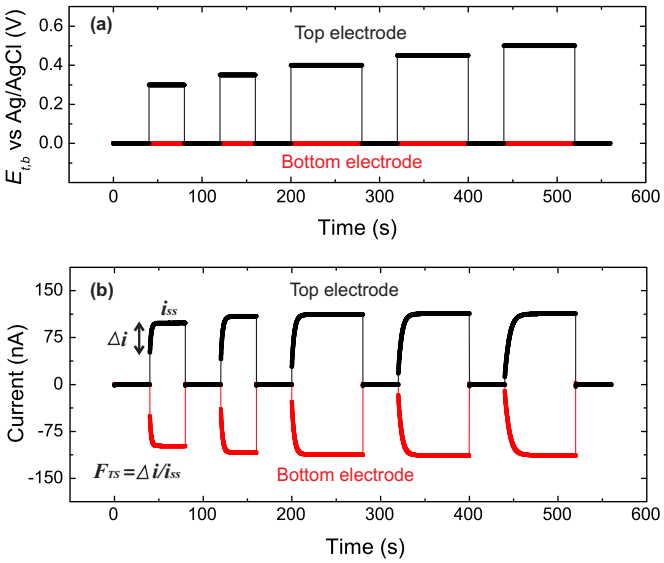

Figure 4.3: Modified multi-potential-step chronoamperometry of a device of type L50H2 filled with an aqueous solution of 1 mM $Fc(MeOH)_2$ and 1 M KCl as supporting electrolyte. (a) Potentials applied as a function of time to the top (black) and bottom (red) electrode. (b) Corresponding current-time response.

Quantitatively, the response time t_{90} (defined as the time to reach 90% of i_{ss} after a perturbation) increased from 5.3 s to 8.1 s and 11.1 s when stepping from 0 V to 0.4 V, 0.45 V and 0.5 V, respectively. For a linear system, one would expect the response time to be independent of the size of the stimulus step. The experimental results therefore indicate that, surprisingly, the response is not linear in the applied voltage.

To quantify the magnitude of the transient, we define the transient fraction, F_{TS}, as the ratio of the current excursion away from its new steady-state value, Δi, and the current level at steady state i_{ss}: $F_{TS} = \Delta i / i_{ss}$. For steps to 0.4 V, 0.45 Vand 0.5 V in Figure 4.3, the observed transient fractions were 75%, 84% and 89%, respectively. Once again, the dependence of the transient fraction on the size of the potential step reflects an underlying nonlinearity.

4.3.2 Transient response analysis

The above results show that the response time of the device varies from a few to a dozen seconds depending on the biasing potential. Several possible mechanisms can be ruled out as the origin because they take place in much shorter time scales: the sourcemeters have a rise time of several ms, much faster than the

observed response; we estimate the RC time of capacitive currents due to charging of the ionic double layer at the electrodes to be only 0.53 ms, as discussed further in Appendix A; and the concentration gradient of redox molecules across the nanochannel is established on a time scale $\tau = z^2/2D = 4.4\,\mu$s after a change in potential, again much shorter than the observed response.

As argued in detail below, we instead interpret the long transient time as the slow diffusive response to potential-dependent adsorption.[14] A change in adsorption of redox molecules at the electrodes after a voltage step causes a temporary concentration difference between the nanochannel and external reservoir; to bring the concentration back into equilibrium, molecules need to diffuse along the length of the nanochannel.

In a first estimate, the time for molecules to diffuse from the access holes of a nanochannel to its centre can be approximated by $(L/2)^2/2D$, where L is the length of the channel. For device type L50H2, this gives a value of 0.65 s. While shorter than the transient times observed in Figure 4.2 and Figure 4.3, this already suggests that longitudinal diffusion of the redox-active species along the length of the device may indeed be implicated in the observed slow response.

To further test this interpretation, we measured the response time of the three device geometries listed in Table 4.1 under identical measurement conditions. The expected ratio of response time between devices of type L10H2, L50H2 and L50H1 was 1 : 15 : 55 ($L/2 = 7\,\mu$m and $27\,\mu$m for devices of type L10H2 and L50H2, respectively; for type L50H1, $L = 52\,\mu$m should be used instead of $L/2$ for the estimation due to the unique access hole at the end of the channel). The measured current responses, $i(t)/i_{ss}$, are shown in Figure 4.4 a. The observed response times were $t_{90} = 0.31$ s, 5.5 s and 19.5 s, corresponding to a ratio 1 : 18 : 65 and consistent with the above estimate. This supports the hypothesis that longitudinal diffusion is responsible for the observed transient response.

In addition to correctly predicting the dependence of t_{90} on geometry, longitudinal diffusion can also quantitatively explain the counterintuitive transient shape observed in Figure 4.2 and Figure 4.3. At any given moment, the redox-cycling current $i(t)$ is proportional to $\overline{c}(t)$, the concentration of redox species present in the channel averaged over the volume of the channel:

$$i(t) = \frac{\overline{c}(t)}{c_b} i_{ss} \tag{4.2}$$

When a potential step is applied, the distribution of molecules inside the channel is altered, resulting in a transient $\overline{c}(t)$. To determine the theoretically expected form of $\overline{c}(t)$ we numerically solved the diffusion equation, $\partial c/\partial t = D_{\text{eff}}\partial^2 c/\partial x^2$ as detailed in Appendix A. Here D_{eff} is an effective diffusion coefficient inside the channel, as discussed further below. The numerical solutions for the current are well described by an analytical expression,

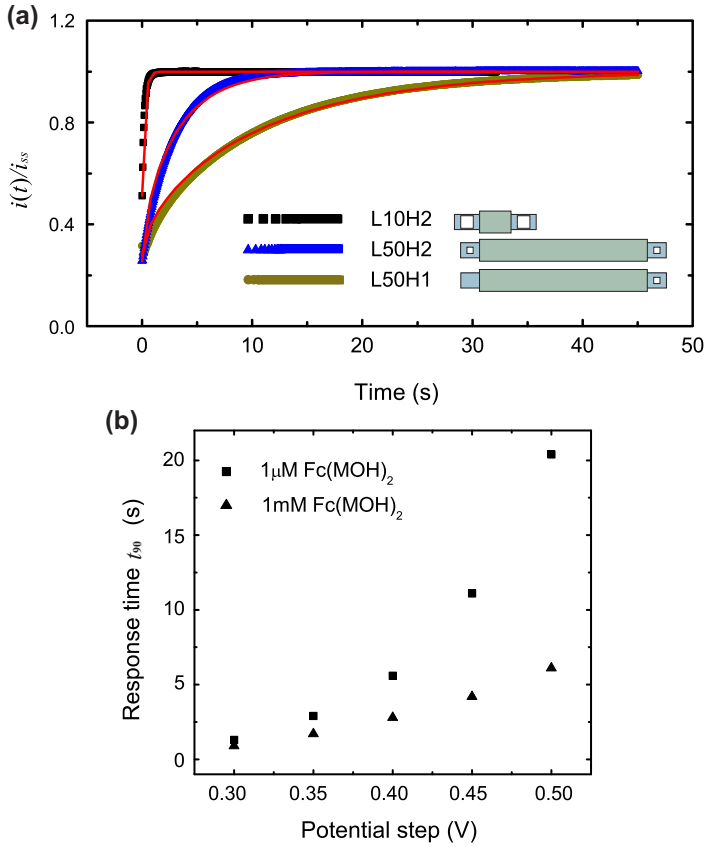

Figure 4.4: (a) Measured current responses $i(t)/i_{ss}$ of devices of type L10H2, L50H2 and L50H1 to a potential perturbation from 0 V to 0.4 V applied to one electrode while keeping the other electrode at 0 V. The red lines are fit to Equation 4.3. (b) Response time t_{90} of device of type L50H2 to potential steps with different magnitudes in 1 mM $Fc(MeOH)_2$ (triangle) and 1 μM $Fc(MeOH)_2$ (square). In order to obtain comparable data, the same device was used for all the measurements and the electrode was cleaned with H_2SO_4 before each measurement.

$$i(t) = i(0^+) + (i_{ss} - i(0^+))\,\mathrm{erf}\left(2.97\gamma\left(\frac{D_{\mathrm{eff}}t}{L^2}\right)^{0.6}\right) \tag{4.3}$$

where $i(0^+)$ is the value of current immediately after the potential step, i_{ss} is the new steady-state current and γ is a numerical constant with a value $\gamma = 1$ and 0.60 for devices with two and one access hole(s), respectively. This analytical form can be fitted to the experimental data and the value of D_{eff} can be extracted.

Fits of the measured current transients to Equation 4.3 are shown in Figure 4.4 a. The shape of the transients matches very well with the fits, which provides

strong evidence that the dynamic response of the nanofluidic device is indeed determined by longitudinal diffusion of the analyte molecules in the nanochannel. The fitted values of the effective diffusion constant, 8.0 $\times 10^{-7}$cm^2/s, 8.5 $\times 10^{-7}$cm^2/s and 5.4 $\times 10^{-7}$cm^2/s for the device of type L10H2, L50H2 and L50H1, respectively, are however one order of magnitude smaller than the diffusion constant measured in bulk (5.6 $\times 10^{-6}$cm^2/s). This indicates that diffusion of the redox species in the channel is dramatically slowed down compared to that in bulk solution.

4.3.3 Adsorption-limited diffusion

Our experimental data exhibit two unexpected features. First, changing the potential of an electrode leads to temporary decreases or increases in the channel concentration $\overline{c}(t)$. Second, the effective diffusion coefficient in the channel, D_{eff}, is smaller than the bulk diffusion coefficient, resulting in longer transients than expected from unconstrained diffusion. We propose that both of these effects share a common origin, namely, reversible adsorption of the analyte molecules onto the channel walls. Adsorption plays a particularly important role in nanochannels due to their high surface-to-volume ratio, and it is well documented that dynamic adsorption results in an apparent decrease of the diffusion coefficient.[14–20] Furthermore, the degree of adsorption of redox species to an electrode was shown to depend on the potential applied to that electrode.[14] As a consequence, molecules are adsorbed or desorbed when changing the potential at an electrode, resulting in the temporary depletion or accumulation of redox molecules inside the channel.

The adsorption scenario[†] corresponding to the data of Figure 4.2 and 4.3 is illustrated in Figure 4.5. In the first case considered, shown in the left column, the potential of the top electrode is stepped from 0 V to 0.5 V while the potential of bottom electrode is kept at 0 V. At time t_1, before the potential step, all the molecules are in the reduced form; the concentration of analyte molecules in the nanochannel, $\overline{c}(t_1)$, then equals the bulk concentration in the external reservoir, c_b, and there is no faradaic current. Some molecules are additionally adsorbed to the electrode surfaces. When the potential of the top electrode is stepped to 0.5 V at time t_2, redox cycling starts and molecules are oxidized at the top electrode. If these oxidized molecules adsorb more strongly to the top electrode than the reduced molecules did prior to the voltage step, the number of diffusing molecules remaining in the channel is temporarily decreased. Consequently, more molecules must enter the channel from the outside reservoir so as to re-establish the concentration balance until, at time t_3, the bulk concentration in the nanochannel, $\overline{c}(t_3)$, equals the bulk concentration, c_b, and a new steady state is approached. At time t_2, stepping to a higher potential causes more molecules to be adsorbed, leaving

[†]The senario is based on the assumption that the adsorption and desoprtion time are much shorter than the typical time for molecules to diffuse through the channel.[19]

fewer freely diffusing molecules in the channel, and causing the initial current to depart further from the new steady-state value. This shows how, in Figure 4.3 b, F_{TS} can increase with the biasing potential of the top electrode. Higher adsorption further means that D_{eff} decreases with increasing potential, which in turn causes the transients to last longer at higher top electrode potential, as observed.

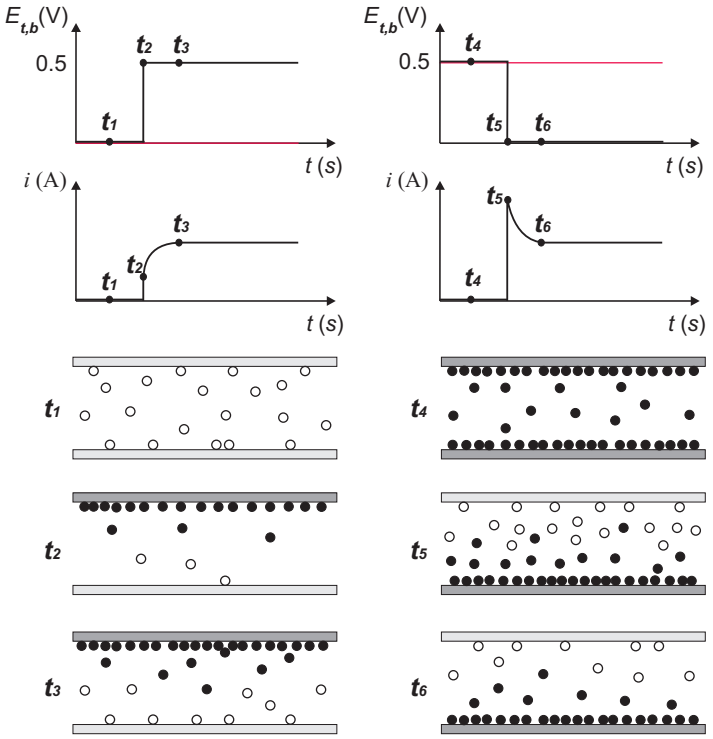

Figure 4.5: Adsorption (left column) and desorption (right column) scenario.

The reverse effect is sketched in the right column of Figure 4.5. Before the potential step, at time t_4, both of the electrodes are biased at 0.5 V, all the molecules inside the nanochannel are oxidized ($\overline{c}(t_4) = c_b$) and no redox cycling current is generated. Additional oxidized molecules are adsorbed to the electrode surfaces. At time t_5, when the potential of the top electrode drops from 0.5 V to 0 V, redox cycling starts and molecules desorb from the electrode, temporarily increasing the concentration of freely diffusing molecules in the channel, and hense the current then gradually decreases until diffusive equilibrium with the external reservoir is re-established. This effect is responsible for the current increases observed in the second half of Figure 4.2 b.

The data above are representative of measurements on more than 20 devices. We have however observed that D_{eff}, and therefore the amount of adsorption,

varied slowly over time for a given device. For example, storing devices for a day in MilliQ water usually resulted in a smaller value of D_{eff}. Occasionally, devices with a freshly etched Cr sacrificial layer exhibited opposite tendencies to those of Figures 4.2 and 4.3, as shown in Appendix A. Such sample history dependence is not surprising since adsorption is extremely sensitive to trace contaminants on the channel surfaces. Cleaning with H_2SO_4, as described in the Experimental section, helped to ensure reproducible starting conditions.

4.3.4 Improving the response time of nanogap transducers

The above finding that the transient response of nanofluidic thin-layer cells is dominated by adsorption suggests several ways to improve the response time of the sensor.

For adsorption-limited diffusion, the mean time for molecules to diffuse along the channel scales as the square of the length of the device. A short device provides a faster response, but at the cost of lower signal levels. By designing long devices with multiple access holes, or building multiple short devices in parallel, the response time can be shortened while maintaining high signal levels.

Less intuitively, Figure 4.2 b and Figure 4.3 b show that the response time is influenced by the biasing potential. This is further demonstrated in Figure 4.4 b, which shows the response time as a function of electrode potential for two concentrations of $Fc(MeOH)_2$ in 1 M KCl. The response time at low concentration (1 μM $Fc(MeOH)_2$) was longer than that at high concentration (1 mM $Fc(MeOH)_2$). This indicates that adsorption is more pronounced at low concentrations. This observation is consistent with the commonly observed Freundlich adsorption isotherm,[21] as well as consistent with previous observations in nanogap devices.[20] Importantly, the response times also increased with increasing electrode potential. This is a very significant effect: with 1 mM $Fc(MeOH)_2$, the response time increased from 2.8 s to 6.1 s for electrode potentials of 0.4 V and 0.5 V, respectively, even though both of these potentials are sufficiently high that the diffusion-limited steady-state current is observed in both cases. Similarly, with 1 μM $Fc(MeOH)_2$, the response time went from 5.6 s to 20.4 s at these potentials. This therefore leads to the important conclusion that the response time of redox cycling sensors can be decreased significantly without loss of signal by choosing operating potentials that minimize adsorption.

Finally, it has been shown that functionalization of the electrodes with self-assembled monolayers of organothiol molecules bearing polar end groups can reduce adsorption.[14] The present analysis indicates that doing so would correspondingly improve the response time of redox cycling sensors.

4.4 Conclusions

We have found that the chronoamperometric response time of redox cycling nanofluidic thin-layer cells is limited by adsorption of redox molecules to the nanochannel surface. Observed trends in the duration, the magnitude, the dependence on device geometry and on electrode potential of the transients are consistent with this interpretation, and the experimentally observed form of the transients is in excellent agreement with simulations based on diffusive mass transport. The observed response times were found to be an order of magnitude longer than expected if adsorption is not taken into account. These findings have important consequences for the design of thin-layer cell sensors since the slowing effect of adsorption can be mitigated by an appropriate choice of electrode material, device geometry and bias potential.

References

[1] Ronkainen, N. J., Halsall, H. B. and Heineman, W. R., Electrochemical Biosensors, *Chem. Soc. Rev.*, **2010**, *39*, 1747-1763.

[2] Wei, D., Bailey, M. J. A., Andrew, P. and Ryhänen, T., Electrochemical Biosensors at the Nanoscale, *Lab Chip*, **2009**, *9*, 2123-2131.

[3] Grieshaber, D., MacKenzie, R., Vörös, J. and Reimhult, E., Electrochemical Biosensors - Sensor Principles and Architectures, *Sensors*, **2008**, *8*, 1400-1458.

[4] Nyholm, L., Electrochemical Techniques for Lab-on-a-chip Applications, *Analyst*, **2005**, *130*, 599-605.

[5] Niwa, O., Xu, Y., Halsall, H. B. and Heineman, W. R., Small-Volume Voltammetric Detection of 4-Aminophenol with Interdigitated Array Electrodes and Its Application to Electrochemical Enzyme-Immunoassay, *Anal. Chem.*, **1993**, *65*, 1559-1563.

[6] Kätelhön, E., Hofmann, B., Lemay, S. G., Zevenbergen, M. A. G., Offenhäusser, A., and Wolfrum, B., Nanocavity Redox Cycling Sensors for the Detection of Dopamine Fluctuations in Microfluidic Gradients, *Anal. Chem.*, **2010**, *82*, 8502-8509.

[7] Schienle, M., Paulus, C., Frey A., Hofmann, F., Holzapfl, B., Schindler-Bauer, P. and Thewes, R., A Fully Electronic DNA Sensor With 128 Positions and in-pixel A/D Conversion, *IEEE J. Solid-St. Circ.*, **2004**, *39*, 2438-2445.

[8] Newman, J. D. and Turner, A. P. F., Home Blood Glucose Biosensors: A Commercial Perspective, *Biosens. Bioelectron.*, **2005**, *20*, 2435-2453.

[9] Yamad,a K., Kitamura, F., Ohsaka, T. and Tokuda, K., Response Time of Thin-layer Electrolytic Cells to Potential-step Signals, *J. Electrochem. Soc.*, **1996**, *143*, 4006-4012.

[10] Devilbiss, J. E., Wang, J. X., Ocko, B. M., Tamura, K., Adzic, R. R., Vartanyants, I. A. and Robionson, I. K., Time Response of the Thin Layer Electrochemical Cell Used for in situ X-ray Diffraction, *Electrochim. Acta*, **2002**, *47*, 3057-3064.

[11] Martin, R. D. and Unwin, P. R., Theory and Experiment for the Substrate Generation Tip Collection Mode of the Scanning Electrochemical Microscope: Application as an Approach for Measuring the Diffusion Coefficient Ratio of a Redox Couple, *Anal. Chem.*, **1998**, *70*, 276-284.

[12] Zevenbergen, M. A. G., Wolfrum, B. L., Goluch, E. D., Singh, P. S. and Lemay, S. G., Fast Electron-transfer Kinetics Probed in Nanofluidic Channels, *J. Am. Chem. Soc.*, **2009**, *131*, 11471-11477.

[13] Bard, A. J. and Faulkner, L. R., *Electrochemical Methods: Fundamentals and Applications*, Wiley: New York, **2001**.

[14] Singh, P. S., Chan, H. M., Kang, S. and Lemay, S. G., Stochastic Amperometric Fluctuations as a Probe for Dynamic Adsorption in Nanofluidic Electrochemical Systems, *J. Am. Chem. Soc.*, **2011**, *133*, 18289-18295.

[15] Pappaert, K., Biesemans, J., Clicq D., Vankrunkelsven, S. and Desmet, G., Measurements of diffusion coefficients in 1-D micro- and nanochannels using shear-driven flows, *Lab Chip*, **2005**, *5*, 1104-1110.

[16] Durand, N. F. Y., Bertsch, A., Todorova, M. and Renaud, P., Direct Measurement of Effective Diffusion Coefficients in Nanochannels Using Steady-state Dispersion Effects, *Appl. Phys. Lett.*, **2007**, *91*, 203106.

[17] Durand, N. F. Y., Dellagiacoma, C., Goetschmann, R., Bertsch, A., Märki, I., Lasser, T. and Renaud, P., Direct Observation of Transitions between Surface-Dominated and Bulk Diffusion Regimes in Nanochannels, *Anal. Chem.*, **2009**, *81*, 5407-5412.

[18] De Santo, I., Causa, F. and Netti, P. A., Subdiffusive Molecular Motion in Nanochannels Observed by Fluorescence Correlation Spectroscopy, *Anal. Chem.*, **2010**, *82*, 997-1005.

[19] Grattoni, A., Gill, J., Zabre, E., Fine, D., Hussain, F. and Ferrari, M., Device for Rapid and Agile Measurement of Diffusivity in Micro- and Nanochannels, *Anal. Chem.*, **2011**, *83*, 3096-3103.

[20] Zevenbergen, M. A. G., Singh, P. S., Goluch, E. D., Wolfrum, B. L. and Lemay, S. G., Electrochemical Correlation Spectroscopy in Nanofluidic Cavities, *Anal. Chem.*, **2009**, *81*, 8203-8212.

[21] Lyklema, J., *Fundamentals of Interface and Colloid Science Volume 1: Fundamentals*, Academic Press, London, **1991**.

Chapter 5

Reversible Adsorption of Outer-sphere Redox Molecules at Pt Electrodes

Adsorption often dominates the response of nanofluidic systems due to their high surface-to-volume ratios. Here we harness this sensitivity to investigate the reversible adsorption of outer-sphere redox species at electrodes, a phenomenon that is easily overlooked in bulk measurements. We find that, even though adsorption does not necessarily play a role in the electron-transfer process, such adsorption is nevertheless ubiquitous for the widely used outer-sphere species. We investigate the physical factors driving adsorption and find that this counter-intuitive behavior is mediated by the anionic species in the supporting electrolyte, closely following the well-known Hofmeister series. Our results provide foundations both for theoretical studies of the underlying mechanisms and for contriving strategies to control adsorption in micro/nanoscale electrochemical transducers where surface effects are dominant.

The contents of this chapter have been published as: Dileep Mampallil, Klaus Mathwig, Shuo Kang and Serge G. Lemay, Reversible Adsorption of Outer-Sphere Redox Molecules at Pt Electrodes, *J. Phys. Chem. Lett.*, 2014, 5 (3), 636–640.

5.1 Introduction

An ideal outer-sphere electron-transfer reaction between a molecule in solution and an electrode involves the tunnelling of one or more electrons without significant chemical interactions developing between the two. This is in contrast to inner-sphere reactions that by definition entail some form of linkage between the molecule and the surface – ranging from covalent binding to adsorption at specific sites – before the reaction can proceed.[1] Outer-sphere reactions are often associated with fast electron transfer that is relatively independent of the nature of the substrate.

Classification into inner- and outer-sphere reactions however pertains only to the electron-transfer mechanism. A reaction proceeds along an outer-sphere pathway and does not in itself rule out the possibility of residual interactions between the electrode and the molecule(s) involved, insofar as such interactions do not influence the electron-transfer process. A prototypical illustration is the case of a redox species immobilized at an electrode, an approach which was famously employed to quantitatively study electron tunnelling in outer-sphere reactions.[2] One can similarly envision that residual interactions between the reduced and/or oxidized forms of a redox species and an electrode lead to some degree of weak adsorption. While not directly involved in electron transfer, such adsorption can nonetheless affect electrochemical experiments by influencing mass transport.

It is widely accepted that small cations and anions in solution can adsorb onto solid electrodes.[3] In general terms, adsorption of a particular species results from a difference in (Gibbs) free energy between the species in bulk solution and at the surface. The microscopic driving mechanism can be enthalpic, entropic, or some combination thereof, and the degree of adsorption is thus sensitive to a broad range of tunable parameters that include temperature, the nature of the solvent, the degree of electrification of the electrode, the presence of other species at the surface and, of course, the identity of the adsorbing species. For example, the degree of specific adsorption of anions on metal electrodes is ion specific and increases in the order F^-, SO_4^{2-}, Cl^-, Br^-, I^-.[4–6] Specific adsorption of ions can in turn change an electrode's interfacial potential distribution[7, 8] and potential of zero charge,[9, 10] with the largest shift arising for the most polarizable ions (e.g., Br^- and I^-). It has further been argued that specific adsorption of anions can influence electrochemical processes, for example through the formation of 'bridges' between a redox-active species and an electrode that increase the reaction rate.[8, 11]

Given the ubiquity of adsorption, it is reasonable to expect that redox species can also exhibit some level of adsorption at electrodes, even when this is not a necessary step in the electron-transfer process. Here we use the term adsorption in its broadest sense to refer to a total surface excess that includes both physi- and chemisorption. Measuring such adsorption however represents a significant challenge since the corresponding surface concentration can represent only

a small fraction of a monolayer. For example, quartz microbalance experiments were initially interpreted as indicating detectable levels of adsorption but this interpretation was later disputed when it was suggested that the data could be understood solely by invoking relatively subtle changes in solution density and viscosity caused by redox reactions.[12] Less controversially, metal nanoparticles functionalized with ferrocene groups were also found to exhibit adsorption at Pt electrodes.[13]

One situation in which even a mild degree of adsorption can have a significant impact on measurements is in micro- or nanofluidic measurement systems. The last decade has seen a surge of activity aimed at creating miniaturized channels and electrodes suitable for electrochemical measurements on minute amounts of solution.[14] The motivations for these advances range from fundamental studies of electron transfer and mass transport, to the development of miniaturized analytical methods suitable for point-of-care diagnostics.[15] An inherent feature of such miniaturized systems is their high surface-to-volume ratio,[16] which can greatly magnify the influence of any surface interaction compared to measurements at more conventional macroscopic or micron-scale electrodes. Over recent years our group has performed a series of redox-cycling measurements at pairs of electrodes separated by nanogaps with heights below 100 nm suggesting that reversible adsorption is ubiquitous in these systems. We find that at high concentrations of redox species, adsorption dominates the noise properties of nanoscale sensors[17, 18] and limits their response time,[19] while at ultra-low-concentrations it significantly decreases the current levels generated by individual molecules.[20] Quantitatively understanding electrochemical processes in these systems thus requires revisiting the possible influence of adsorption.

Here we take advantage of our nanofluidic approach to investigate adsorption of outer-sphere redox couples. The nanogap geometry facilitates the measurements in three distinct manners: (1) it creates a very high surface-to-volume ratio, which increases the relative number of adsorbed molecules and therefore magnifies the influence of adsorption at the surfaces, (2) it insures that the absolute number of redox molecules in the detection region remains relatively small, which allows stochastic spectroscopy methods to be applied to the signals, and (3) it permits very efficient redox cycling, such that minute amounts of analyte, even down to single molecules at sub-nanomolar concentrations, can be detected.[20, 21] These factors render the method extremely sensitive even to small amount of adsorption. Our observations provide a solid basis for understanding the underlying physical mechanisms responsible for the adsorption.

A sketch of a nanogap device is shown in Figure 5.1 a. A detailed method for making the devices using optical lithography is given in Appendix B, and an optical image of a completed device is shown in Figure 5.1 b. All data shown here employ Pt electrodes based on thin films created by electron-beam evaporation. The active volume, namely, the volume sandwiched between the two redox-cycling

electrodes, is defined by the length of the top electrode, L_a, the width of the bottom electrode, w_b, and the separation between the electrodes, h. Here we employ two distinct families of devices, type 1 and type 2, with $L_a \times w_b \times h$ = 100 μm × 3 μm × 130 nm and 10 μm × 3 μm × 60 nm respectively. The redox-cycling current in a device is given by $i_{\text{lim}} = (enD/h^2)N_{\text{sol}}$, where $-e$ is the charge of the electron, n is the number of electrons transferred per cycle, D is the diffusion coefficient, and N_{sol} is the number of molecules in solution inside the active volume at a given instant. On average, $\langle N_{\text{sol}} \rangle = N_A L_a w_b h c$, where N_A is Avogadro's number and c is the molar concentration of the redox species in the reservoir of the device, which is independent of the level of adsorption at the surface of the electrodes.

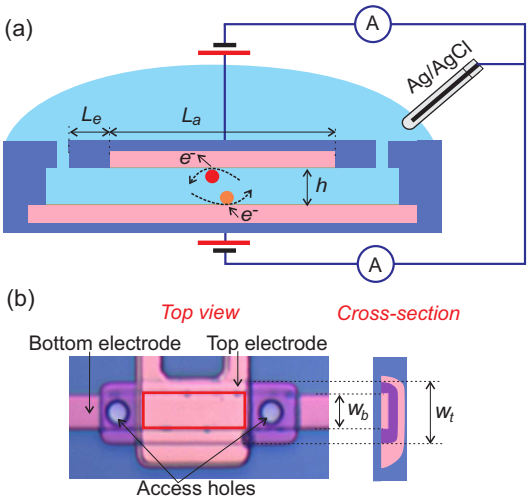

Figure 5.1: (a) Schematic diagram of the longitudinal cross-section of a nanogap device used for redox cycling. The two electrodes are shown in pink. Also identified are the height of the nanochannel, h, the length of the active redox-cycling region, L_a, and the length of the access channels, L_e. (b) Top view optical image of a device and schematic illustration of its cross-section. The active region (red rectangle) is defined as the volume between the top and the bottom electrodes. The widths of the bottom electrode and of the nanochannel are w_b and w_t, respectively.

5.2 Discussion

We first illustrate how reversible adsorption can be directly observed in nanofluidic systems through two separate experiments, potential-step amperometry and electrochemical correlation spectroscopy, as summarized in Figure 5.2. Each of these experiments furnishes two independent signatures of adsorption, emphasizing its broad impact on redox-cycling measurements.

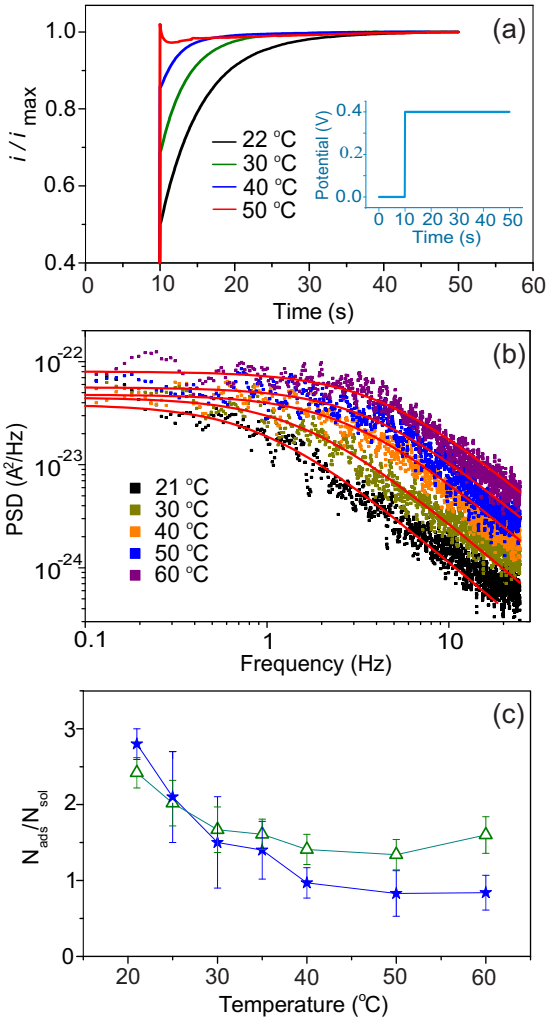

Figure 5.2: Redox-cycling measurements with 1 mM $Fc(MeOH)_2$ in 1 M KCl. (a) Transient response of the redox cycling current from a device of type 1 for a step change in the potential of the top electrode (inset) while the bottom electrode is held at 0 V. Each curve represents a different temperature, as indicated; the transient becomes shorter and less pronounced with increasing temperature, both trends reflecting a decrease in adsorption as discussed in the main text. (b) Power spectral density (PSD) of the fluctuations in the redox cycling current at different temperatures using a device of type 2. The shift of the PSD towards higher frequencies with increasing temperature reflects a combination of higher diffusion coefficients and decreasing adsorption. The red lines are fits from which values of the crossover frequency $f_{0,m}$ can be extracted. (c) Absolute degree of adsorption deduced from using Equation 5.1 (filled stars) and Equation 5.2 (open triangles). The error bars represent the standard deviation from five consecutive measurements.

Potential-step amperometry gives the clearest qualitative signature of adsorption in nanogap devices by exploiting the fact that the degree of adsorption typically depends on the electrode potential. For example, adsorption of the oxidized form of ferrocene is observed to be enhanced with increasing electrode potential.[18, 19] Abruptly stepping the potential of an electrode to a higher potential therefore causes a temporary decrease of the analyte concentration inside the nanogap as more molecules become bound to the electrode; this local depletion then recovers over time as more molecules diffuse from a large reservoir outside the device. Correspondingly, the redox cycling current, which is proportional to the local concentration of freely-diffusing analyte inside the nanodevice, is suppressed immediately following the potential step. It then gradually recovers over time, the rate of recovery being dictated by diffusion from the external reservoir and into the nanodevice. Because this diffusion is hindered by adsorption, slower recovery indicates increased adsorption. Both the magnitude of the initial current suppression and the duration of the recovery are thus indications of the degree of adsorption.[19]

This phenomenon is illustrated in Figure 5.2 a for 1 mM $Fc(MeOH)_2$ in 1 M KCl supporting electrolyte for a range of temperatures in device type 1. The bottom electrode (reducing) was kept at 0 V. At room temperature (22 °C), a ∼50% suppression of the limiting current is observed upon stepping the potential of the top electrode (oxidizing) from 0 V to 0.4 V, indicating enhanced adsorption at the oxidizing electrode. The current then recovers to its diffusion-limited value after ∼20 s. As the temperature is increased, the amplitude of the departure from the limiting current and duration of the transient both decrease, reaching <5% and 5 s, respectively, at 50 °C. These independent trends are mutually consistent.

Potential-step amperometry, while providing direct, qualitative evidence for adsorption, is only sensitive to differences in adsorption between two different electrode potentials. To measure the absolute amount of adsorbed molecules, we instead rely on electrochemical correlation spectroscopy, which probes fluctuations in the number of redox-active molecules inside the active volume resulting from Brownian motion. We have shown earlier[17, 22] that the random noise present in the redox cycling current is dominated by these intrinsic equilibrium fluctuations. The power spectral density (PSD) of the fluctuations, $S(f)$, takes the relatively simple form[17] $S(f) = S_{0,m}/(1 + (f/f_{0,m})^{3/2})$, where the crossover frequency $f_{0,m}$ is a parameter that quantifies the effect of Brownian motion. In the absence of adsorption, $f_{0,m}$ takes the ideal value $f_0 = \frac{D}{\pi}\left(\frac{3}{L_a^2(L_a+6L_e)}\right)^{2/3}$. Here L_a and L_e describe the channel geometry, as given in Figure 5.1 a. In the presence of adsorption the value of $f_{0,m}$ decreases below its ideal value; the absolute number of adsorbed molecules at both electrodes, N_{ads}, can then be extracted *via* the expression[17]

$$\frac{N_{\mathrm{ads}}}{N_{\mathrm{sol}}} = \frac{f_0}{f_{0,m}} - 1 \tag{5.1}$$

We measured the current-time fluctuations of the redox-cycling current under the same conditions as the data of Figure 5.2 a in type 2 devices with $L_e = 1$ μm and with the oxidizing and reducing electrodes set at 0.45 V and 0 V, respectively; further details can be found in Appendix B. The corresponding PSDs are shown in Figure 5.2 b. The spectra exhibit the expected form, crossing over from white noise at low frequencies to a $f^{-3/2}$ behavior above a characteristic frequency $f_{0,m}$. The crossover frequency clearly increases with increasing temperature, indicating that molecules can enter and exit the detection volume faster at higher temperatures. While one could expect an increase by a factor of 1.8 between 21 °C and 50 °C due to the increase of the diffusion coefficient D over this temperature range (Appendix B), this is insufficient to explain the observed factor 4.3 change in $f_{0,m}$. We attribute the additional increase to a change in adsorption with temperature. Applying Equation 5.1 yields the amount of adsorption, $N_{\mathrm{ads}}/N_{\mathrm{sol}}$, as a function of temperature, as shown by the filled stars in Figure 5.2 c. The adsorption decays monotonically with increasing temperature over the temperature range investigated, consistent with the qualitative conclusions from the transient measurements of Figure 5.2 a. Somewhat counter-intuitively, $N_{\mathrm{ads}}/N_{\mathrm{sol}}$ is found to be of order unity or higher. This is a direct consequence of the large surface-to-volume ratio: for a 1 mM solution in a 60 nm nanogap, $N_{\mathrm{ads}}/N_{\mathrm{sol}} = 1$ corresponds to a surface density of only 0.04 molecule per nm^2, well below full surface coverage.

In practice the spectral analysis described above requires extensive data and prior knowledge of the diffusion coefficient of the molecules. We have earlier demonstrated that the degree of adsorption can also be extracted from the total amplitude of the redox-cycling current fluctuations, $I_{F,\mathrm{rms}}$.[18] In short, this approach is model independent and relies solely on the assumption that analyte molecules undergo independent Brownian motion. High adsorption translates into more molecules participating to the redox-cycling process, but each molecule contributing a smaller current; high adsorption thus leads to more averaging and smaller fluctuations, as indicated by the equation

$$\frac{N_{\mathrm{ads}}}{N_{\mathrm{sol}}} = \frac{1}{N_{\mathrm{sol}}} \frac{I_F^2}{I_{F,\mathrm{rms}}^2} - 1 \tag{5.2}$$

here I_F is the average redox-cycling current and for most of the measurements described here $I_F = i_{\mathrm{lim}}$. Strictly speaking, a correction is required to Equation 5.2 to account for the transverse motion of redox molecules in and out of the active region since $w_c \neq w_b$ as shown in Figure 5.1 b. Because these transverse fluctuations occur at relatively high frequencies and are thus masked by motion in the longitudinal direction, however, we simplify our analysis by neglecting these corrections (see Appendix B for further details).

The value of $I_{F,\mathrm{rms}}$ is readily obtained from amperometric current-time traces. Figure 5.2 c shows the deduced degree of adsorption obtained using Equation 5.2

(open triangles) as a function of temperature. The data once again show that an increase in temperature by about 20 °C above room temperature decreases the degree of adsorption by a factor of 2 to 3. Both Equation 5.1 and Equation 5.2 yield similar adsorption values;[18] we ascribe the small mismatch at high temperatures to the uncertainty in determining I_F caused by small fluctuations in the temperature.

The measurements above show four separate ways in which adsorption of redox species is made manifest in nanogap devices. All of these exhibit consistent trends with temperature. For the remainder of this work, we concentrate on the method of Equation 5.2 as it is general, quantitative and straightforward to apply to experimental data.

The data of Figure 5.2 indicate that, perhaps counter-intuitively, the positively charged oxidized form of $Fc(MeOH)_2$ exhibits enhanced adsorption at positively biased electrodes. This suggests that the adsorption might be mediated by the negatively charged anions in the supporting electrolyte. To investigate this scenario, we quantified the adsorption of $Fc(MeOH)_2$ for different supporting electrolyte anionic species while keeping the cationic species as K^+. The results are plotted in Figure 5.3. We find that the degree of adsorption increases according to the anion sequence $SO_4^{2-} \sim F^- < Cl^- < Br^- < I^-$. This sequence is closely related to the well-known Hofmeister series,[23, 24] which was originally introduced to classify ions in terms of their ability to precipitate proteins. The relative effectiveness of anions or cations in a wide range of bio-chemical processes, for example protein crystallization, colloidal systems and the adsorption of cationic surfactants, to list a few, also follow the Hofmeister series.[25, 26] The sequence SO_4^{2-}, F^-, Cl^-, Br^-, I^- also corresponds to the direction of decreasing free energy of hydration.[27] It is possible that anions, especially the ions such as Br^- and I^- with low hydration energy, can partially deform their hydration shell in favor of specific adsorption at the interface.[5] In support of this scenario, the observed sequence is close to the direction of increasing degree of specific adsorption of anions on metal electrodes given as F^-, SO_4^{2-}, Cl^-, Br^-, I^-.[4–6]

Details of the interactions of molecules at the electrode-electrolyte interface can be very complex. For example, many experimental studies in the literature point to the possibility of binding between the adsorbed anions and the oxidized molecules (ferrocenium ions). Surface ferrocenium ions can have entropically enhanced binding with low hydration energy anions present in the supporting electrolyte through ion pairing.[28–30] The formation energy of the ion pairs roughly scales with the solvation energies of the anions[28] which is consistent with the Hofmeister series.

Surprisingly, we also observed a link between the type of anion and the limiting current: with non-adsorbing anions like F^- and SO_4^{2-}, we have observed decreased limiting currents and voltammograms representing slow reaction kinetics (see also Appendix B). Similar observations were reported in measurements

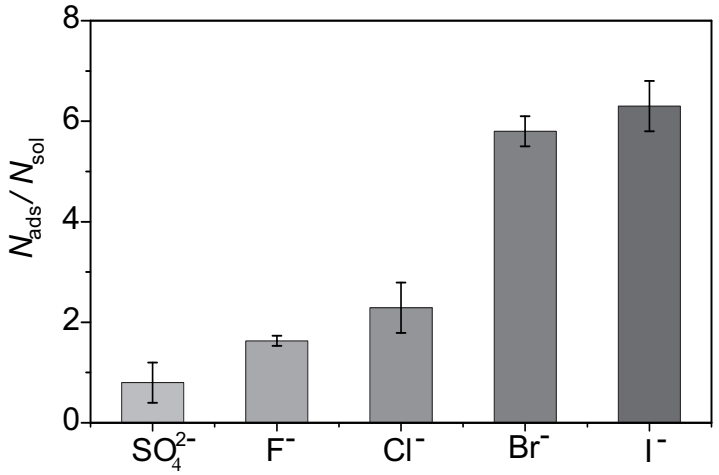

Figure 5.3: The degree of adsorption of $Fc(MeOH)_2$ versus anionic species present in the supporting electrolyte at room temperature. The degree of adsorption increases according to the sequence $SO_4^{2-} \sim F^- < Cl^- < Br^- < I^-$. The oxidizing and reducing electrodes were kept at 0.45 V and 0 V, respectively.

at nanoelectrodes with different supporting electrolytes.[31, 32] These observations were ascribed to a range of different mechanisms including adsorption,[31] Frumkin and dynamic diffuse-layer effects[32] and ion pairing.[33]

The molecule-electrode interactions driving adsorption can of course be species dependent. We quantified the degree of adsorption for five commonly employed redox species, as summarized in Figure 5.4, all of which exhibited some degree of adsorption. Among these, FcA^- and $[Fe(CN)_6]^{3-}$ exhibited the lowest and $[Ru(NH_3)_6]^{3+}$ the highest degree of adsorption. This is in contradiction with the common assumption that $[Ru(NH_3)_6]^{3+}$ does not adsorb on noble metal (gold) electrodes in electrochemical quartz crystal microbalance studies.[12] On the other hand, various other scenarios of the adsorption property of $[Ru(NH_3)_6]^{3+}$ were reported in the literature. For example, adsorption of positively charged $[Ru(NH_3)_6]^{3+}$ at negatively charged silica surfaces is used for preparing Ru based catalysts.[34] Similarly, $[Ru(NH_3)_6]^{3+}$ adsorbs at anionic self-assembled monolayers (SAM)[35] especially at the domain boundaries and defects formed on the SAM.[36] Singh et al.[18] also reported adsorption of $[Ru(NH_3)_6]^{3+}$ on bare platinum electrodes, where, contrary to other reports,[34–36] adsorption was found to decrease with increasing negative potentials on the electrodes. By analogy to the anion-mediated adsorption of $Fc(MeOH)_2$, we suggest that the counter-intuitive adsorption behavior of $[Ru(NH_3)_6]^{3+}$ may be mediated by the excess cations near the electrodes at negative electrode potentials.

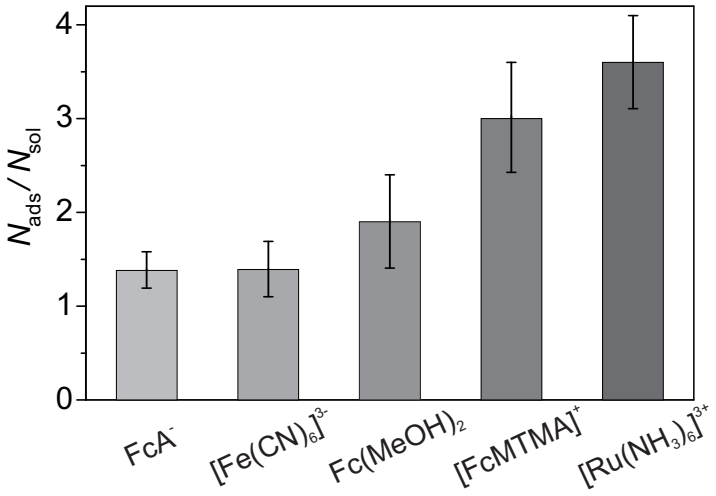

Figure 5.4: The degree of adsorption for five different redox molecules, ferrocene carboxylic acid (FcA^-), hexacyanoferrate-III ($[Fe(CN)_6]^{3-}$), 1,1 ferrocene dimethanol ($Fc(MeOH)_2$), (ferrocenyl methyl) trimethyl ammonium ($[FcMTMA]^+$) and hexaammine ruthenium ($[Ru(NH_3)_6]^{3+}$) at room temperature. The potentials at the oxidizing and the reducing electrode were 0.45 V and 0 V, respectively (or 0 V and -0.4 V for $[Ru(NH_3)_6]^{3+}$).

5.3 Conclusions

In summary, we have studied the adsorption of several outer-sphere electroactive species at Pt electrodes. We find that adsorption plays a significant role in both stepped-voltammetry and spectral measurements. Different degrees of adsorption were observed for several commonly-employed outer-sphere redox couples and surprisingly, $[Ru(NH_3)_6]^{3+}$, which is often considered as a particularly ideal species, exhibited the highest adsorption among the molecules we studied. Systematic investigations with $Fc(MeOH)_2$ suggest that its adsorption is mediated by the anionic species in the supporting electrolyte and follows the well-known Hofmeister series. Our results help to design measurement conditions where adsorption can be controlled, for example in single-molecule electrochemistry measurements where excess adsorption mainly limits the signal-to-noise ratio.[20, 21]

References

[1] Bard, A. j. and Faulkner, L. R., *Electrochemical Methods: Fundamentals and Applications*, John Wiley & Sons: New York, **2001**.

[2] Finklea, H. O., Electrochemistry of Organized Monolayers of Thiols and Related Molecules on Electrodes, *Electroanal. Chem.* **1996**, *19*, 109-335.

[3] Pletcher, D., Mitchell,P. J., Hampson, N. A. and McNell, A. J. S., Adsorption at Solid Electrodes, *Electrochem.*, **1985**, *10*, 1-84.

[4] Paik, W.-K., Genshaw, M. A. and Kris, J. O., Adsorption of Anions at the Solid-Solution Interface. Ellipsometric Study, *J. Phys. Chem.* **1970**, *74*, 4266-4275.

[5] Magnussen, O. M., Ordered Anion Adlayers on Metal Electrode Surfaces, *Chem. Rev.*, **2002**, *120*, 679-725.

[6] Tripkovic D. V., Strmcnik D., van der Vliet D., Stamenkovic V. and Markovic N. M., The Role of Anions in Surface Electrochemistry, *Faraday Discuss.*, **2008**, *140*, 25-40.

[7] Grahame, D. C., The Electric Double Later and the Theory of Electrocapilarity, *Chem. Rev.*, **1947**, *41*, 441.

[8] Timmer, B., Rehbach, M. S. and Sluyters, J. H., Electrode Kinetics and Double Layer Structure, *Surface Science*, **1969**, *18*, 44-61.

[9] Lyklema, J., Points of Zero Charge in the Presence of Specific Adsorption, *J. Colloid Interf, Sci.*, **1984**, *99*, 109-117.

[10] Conway, B. E., Individual Solvated Ion Properties and Specificity of Ion Adsorption Effects in Processes at Electrodes, *Chem. Soc. Rev.*, **1992**, *21*, 253-261.

[11] Frumkin A. N. and Nikolajeva N. V., On the Electroreduction of Anions, *J. Chem. Phys.*, **1957**, *26*, 1552.

[12] Lee W. W., White H. S. and Ward M. D., Depletion Layer Effects on the Response of the Electrochemical Quartz Crystal Microbalance, *Anal. Chem.*, **1993**, *65*, 3232-3237.

[13] Stiles, R. L., Balasubramanian, R., Feldberg, S. W. and Murray, R. W., Anion-induced Adsorption of Ferrocenated Nanoparticles, *J. Am. Chem. Soc.* **2008**, *130*, 1856-1865.

[14] Oja S. M., Wood M. and Zhang B., Nanoscale Electrochemistry, *Anal. Chem.*, **2013**, *85*, 473-486.

[15] Ronkainen, N. J., Halsall H. B. and Heineman W. R., Electrochemical Biosensors, *Chem. Soc. Rev.*, **2010**, *39*, 1747-1763.

[16] Bocquet, L. and Charlaix, E., Nanofluidics, From Bulk to Interfaces, *Chem. Soc. Rev.*, **2010**, *39*, 1073-1095.

[17] Zevenbergen, M. A. G., Singh, P. S., Goluch, E. D., Wolfrum, B. L. and Lemay, S. G., Electrochemical Correlation Spectroscopy in Nanofluidic Cavities, *Anal. Chem.*, **2009**, *81*, 8203-8212.

[18] Singh, P. S., Chan, H. S. M., Kang, S. and Lemay, S. G., Stochastic Amperometric Fluctuations as A Probe for Dynamic Adsorption in Nanofluidic Electrochemical Systems, *J. Am. Chem. Soc.*, **2011**, *133*, 18289 -18295.

[19] Kang, S., Mathwig, K. and Lemay, S. G., Response Time of Nanofluidic Electrochemical Sensors, *Lab Chip*, **2012**, *12*, 1262-1267.

[20] Zevenbergen, M. A. G., Goluch, E. D., Singh, P. S., Wolfrum, B. L. and Lemay, S. G., Stochastic Sensing of Single Molecules in a Nanofluidic Electrochemical Device, *Nano Lett.*, **2011**, *11*, 2881-2886.

[21] Kang, S., Nieuwenhuis, A. F., Mathwig, K., Mampallil, D. and Lemay, S. G., Electrochemical Single-molecule Detection in Aqueous Solution Using Self-Aligned Nanogap Transducers, *ACS Nano*, **2013**, *7*, 10931-10937.

[22] Zevenbergen, M. A. G., Krapf, D., Zuiddam, M. R. and Lemay, S. G., Mesoscopic Concentration Fluctuations in a Fluidic Nanocavity Detected by Redox Cycling, *Nano Lett.*, **2007**, *7*, 384-388.

[23] Kunz, W., Henle, J. and Ninham, B. W., About the Science of the Effect of Salts, *Curr. Opin. Colloid Interface Sci.*, **2004**, *9*, 19-37.

[24] Kunz, W., Lo Nostro, P. and Ninham, B. W., The Present State of Affairs with Hofmeister Effects, *Curr. Opin. Colloid and Interface Sci.*, **2004**, *9*, 1-18.

[25] Para, G., Jarek, E. and Warszynski, P., The Hofmeister Series Effect in Adsorption of Cationic Surfactants: Theoretical Description and Experimental Results, *Adv. Colloid and Interface Sci.*, **2006**, *74*, 39-55.

[26] Zhang Y. and Cremer, P. S., Interactions between Macromolecules and Ions: The Hofmeister Series, *Curr. Opin. Chemical Biology*, **2006**, *10*, 658-663.

[27] Marcus, Y., Thermodynamic Functions of Transfer of Single Ions from Water to Non-aqueous, *Pure and Appl.Chem.*, **1982**, *54*, 2327-2334.

[28] Rowe, G. K. and Creager, S. E., Redox and Ion-pairing Thermodynamics in Self-assembled Monolayers, *Langmuir*, **1991**, *7*, 2307-2312.

[29] Acevedo, D. and Abruna, H. D, Electron-Transfer Study and Solvent Effects on the Formal Potential of a Redox-Active Self-Assembling Monolayer, *J. Phys. Chem.*, **1991**, *95*, 9590-9594.

[30] Valincius, G., Niaura, G., Kazakevičienė, B., Talaikytė, Z., Kažemėkaitė, M., Butkus, E. and Razumas, V., Anion Effect on Mediated Electron Transfer through Ferrocene-Terminated Self-Assembled Monolayers, *Langmuir*, **2004**, *20*, 6631-6638.

[31] Beriet, C. and Pletcher, D., A Microelectrode Study of the Mechanism and Kinetics of the Ferro/Ferricyanide Couple in Aqueous Media: The Influence of the Electrolyte and its Concentration, *J. Electroanal. Chem.*, **1993**, *361*, 93-101.

[32] Chen, S. and Kucernak, A., The Voltammetric Response of Nanometer-sized Carbon Electrodes, *J. Phys. Chem. B*, **2002**, *106*, 9396-9404.

[33] Watkins, J. J. and White, H. S., Ion-pairing Kinetics Investigated Using Nanometer-size Pt Electrodes, *J. Electroanal. Chem.*, **2005**, *582*, 57-63.

[34] Jiao, L. and Regalbuto, J. R., The Synthesis of Highly Dispersed Noble and Base Metals on Silica via Strong Electrostatic Adsorption: I. Amorphous Silica, *J. Catalysis*, **2008**, *260*, 329-341.

[35] Steichen, M., Doneux, T. and Buess-Herman, C., On the Adsorption of Hexaammineruthenium (III) at Anionic Self-Assembled Monolayers, *Electrochimica Acta*, **2008**, *53*, 6202-6208.

[36] Grubb, M., Wackerbarth, H., Wengel, J. and Ulstrup, J., Direct Imaging of Hexaamine-Ruthenium(III) in Domain Boundaries in Monolayers of Single-stranded DNA, *Langmuir*, **2007**, *23*, 1410-1413.

Chapter 6

Electrochemical Single-Molecule Detection in Aqueous Solution Using Self-Aligned Nanogap Transducers

Electrochemical detection of individual molecular tags in nanochannels may enable cost effective, massively parallel analysis and diagnostics platforms. Here we demonstrate single-molecule detection of prototypical analytes in aqueous solution based on redox cycling in 40 nm nanogap transducers. These nanofluidic devices are fabricated using standard microfabrication techniques combined with a self-aligned approach that minimizes gap size and dead volume. We demonstrate the detection of three common redox mediators at physiological salt concentrations.

The contents of this chapter have been published as: Shuo Kang, Ab F. Nieuwenhuis, Klaus Mathwig, Dileep Mampallil, and Serge G. Lemay, Electrochemical Single-Molecule Detection in Aqueous Solution Using Self-Aligned Nanogap Transducers, *ACS Nano*, 2013, 7 (12), 10931–10937.

6.1 Introduction

Techniques for detecting and manipulating (macro)molecules in solution near or at the single-molecule limit enable both fundamental studies and new analytic applications.[1–7] The latter include assays in which the sample has a microscopic volume, such as single-cell analysis,[8, 9] or in which the measurement inherently requires such resolution, for example single-molecule DNA sequencing.[10] Particularly interesting are purely electrical detection approaches that are compatible with integrated electronics as they can lead to massively parallel assays at low costs, enabling faster and cheaper point-of-care diagnostic[11, 12] and clinical tools.[13] An important bottleneck in the development of such technology is the realization of transducers that can effectively convert chemical information directly into electrical signals at micro- and nanoscale detectors.

A candidate approach is electrochemical detection, an all-electrical, low-power transduction mechanism that is highly compatible with microfabrication. We recently demonstrated electrochemical single-molecule detection at the proof-of-concept level in an organic solvent, acetonitrile, using nanogap devices.[14] These consist of two closely-spaced electrodes separated by a nanochannel, as sketched in Figure 6.1 a. Redox cycling - the repeated, successive oxidation and reduction of analyte molecules at the two electrodes - provided the required charge amplification.

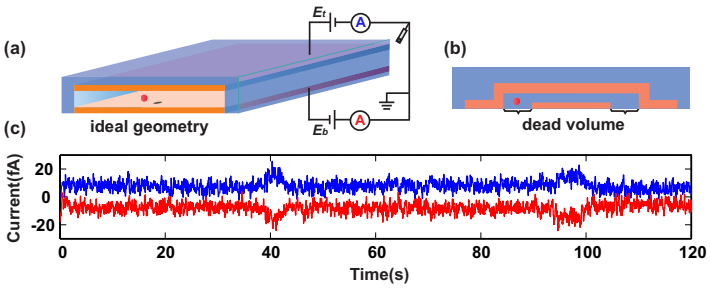

Figure 6.1: (a) Schematic of a nanogap device with ideal geometry: both the top and bottom electrodes span the full width of the nanochannel. (b) Schematic cross-section of a nanogap device with dead volumes due to alignment tolerances during microfabrication. This lowers the redox-cycling efficiency. (c) Current-time traces simultaneously obtained at the top (blue) and bottom (red) electrodes under redox cycling conditions (E_t = 0.5 V and E_b = 0.35 V with 10 pM FcTMABr in 0.1 M KCl aqueous solution). The traces have been vertically offset for clarity. Discrete, anti-correlated current steps with amplitude ∼7 fA are generated each time that an individual $FcTMA^+$ molecule enters and subsequently exits the nanogap. Here two events are observed during a 120 s period.

Even with highly efficient redox cycling, however, single-molecule detection is characterized by extremely low current levels in the femtoampere (10^{-15} A) range. This is near the limits of detectability at room temperature. As a result,

and because the diffusion coefficient of redox molecules in water is lower than that in typical organic solvents, measurements in water have proven unsuccessful so far. Since most (bio)analytical samples take the form of aqueous solutions, the ability to measure in water represents a key milestone in the further development of single-molecule electrochemical assays.

Here we present the first nanofluidic single-molecule electrochemical measurements in aqueous solution. This is made possible by a new microfabrication approach based on a self-aligned process which refines the nanogap geometry (eliminating the so-called dead volume illustrated in Figure 6.1 b) and facilitates downscaling the gap size. This process is based entirely on conventional optical lithography and is thus suitable for mass production. We demonstrate the ability to detect common redox mediators including ferricyanide and ferrocene derivatives as they freely diffuse in and out of the detection region of the transducer, as illustrated in Figure 6.1 c. All measurements were performed near physiological conditions, illustrating the compatibility of our approach with samples of biological relevance.

6.2 Results and discussion

6.2.1 Self-aligned electrode fabrication

A key challenge in fabricating nanogaps is to minimize the distance between the electrodes, z, while avoiding short circuits along the edges of the electrodes. In earlier work,[15–17] the bottom electrode, a sacrificial layer and the top electrode were deposited in separate steps with the sacrificial layer completely enveloping the bottom electrode in order to prevent any contact between the top and bottom electrodes. Following removal of the sacrificial layer this led to the geometry shown in Figure 6.1 b, where the electrode spacing z is set by the original thickness of the sacrificial layer. As the thickness of the sacrificial layer must be thicker than that of the bottom electrode to guarantee good step coverage, this imposed an important limitation on the minimum achievable z. In addition, the sacrificial layer needed to be wider than the bottom electrode to allow for alignment tolerances during lithography. This in turn led to a dead volume where the top and bottom electrodes did not overlap, as indicated in Figure 6.1 b. Whenever an analyte molecule enters this region no redox cycling can take place, lowering the observed current. Given typical alignment tolerances in optical lithography, the dead volume can easily be as wide as 1 μm on each side of the bottom electrode, thus occupying 40% of the channel in a 5 μm wide device[16] and causing a corresponding decrease in the single-molecule signal. Because of single-molecule detection at the limit of the sensitivity of present electronics, this can be enough to render such measurements impossible.

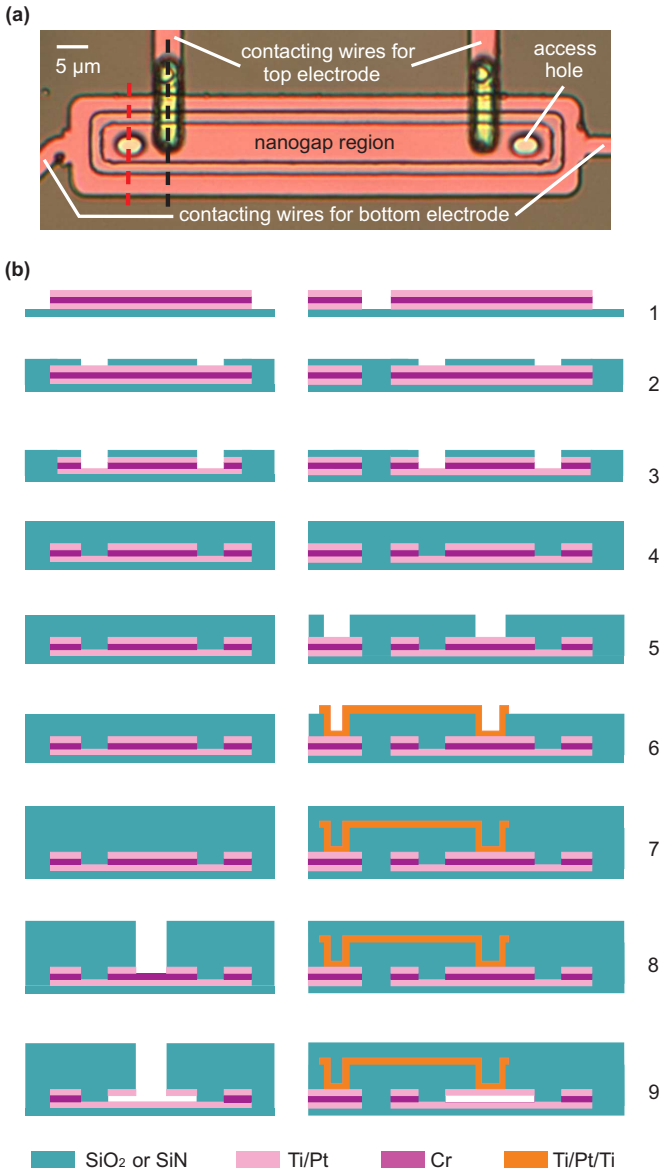

Figure 6.2: (a) Optical microscope image (top view) of a device prior to Cr etching. (b) Schematic device cross-sections (not drawn to scale) at different stages of the fabrication process; the sketches in the left and right columns correspond to the cross-sections along the red and black dashed lines in (a), respectively. 1. A stack of metal layers is deposited and patterned. 2. SiO_2 is deposited and patterned as a mask layer. 3. A trench is etched by IBE to define the detection region and treatment in aqua regia is used to remove the redeposition. 4 and 5. SiN is deposited and patterned. 6. A metal layer stack is deposited and patterned for electrical interconnection. 7. A final passivation layer is deposited. 8. Access holes are generated. 9. The sacrificial layer is etched and the nanochannel is released.

Here we introduce an alternate approach which circumvents these difficulties. The bottom electrode, sacrificial layer and top electrode were first deposited together, following which the edges of the electrodes and sacrificial layer were defined in a single lithography step. This allowed both minimizing the dead volume and simultaneously reducing the risk of short circuits between the electrodes. An additional benefit was that the electrode surface was not exposed to environmental conditions or additional chemicals throughout the complete fabrication process up to release of the sacrificial layer. Such an uncontaminated surface can improve the reproducibility of electrochemical measurements, which are very sensitive to surface conditions.

Figure 6.2 a shows an optical image of a finished device, and the fabrication scheme is illustrated in Figure 6.2 b. In short, a stack of metal layers was deposited and patterned in one step on a 4-inch Si wafer (step 1), followed by an ion-beam etching (IBE) to define the detection region with SiO_2 as a mask (steps 2-3). Step 3 represents the key step in creating the "self-aligned" structure as it automatically leads to the sacrificial layer and top electrode having the same width independently of alignment tolerances. Step 3 was also followed by a short (5 min) cleaning etch in aqua regia to remove material re-deposited during IBE. Afterwards (steps 4-7) another metal layer stack was defined as the electrical interconnection for top electrode between two passivation layers deposited as insulating and protecting layer, and finally access holes were generated through which the sacrificial layer was etched and the nanochannel was released (steps 8-9). Additional details about the individual steps are given in Appendix C.

Figure 6.3 a shows a scanning electron microscope (SEM) image of a finished device while Figure 6.3 b, 6.3 c and 6.3 d show its cross-sections at different levels of magnification after the device was cut open using a focused ion beam (FIB) along the dashed line in Figure 6.3 a. A 200 nm wide dead-volume region is visible on each side of the bottom electrode, as indicated by the dotted lines in Figure 6.3 d; this was created during the cleaning aqua regia etch, which also attacked the edge of the top electrode. Further optimizing the durations of the IBE and aqua regia etches (see Appendix C) allowed compensating for this unwanted feature, resulting in a dead volume as small as 80 nm (Figure 6.3 e).

The morphology of the device was measured with atomic force microscopy (AFM) to investigate the flatness of the top wall of the electrode once the nanochannel was released and filled with 1 mM $Fc(MeOH)_2$ in 0.1 M KCl (AFM image shown in Appendix C). No bending of the top electrode membrane was observed, as expected since a combination of multiple SiO_2 and SiN layers were deposited to balance the stress.[18, 19] Therefore, the gap size solely depends on the thickness of the sacrificial layer.

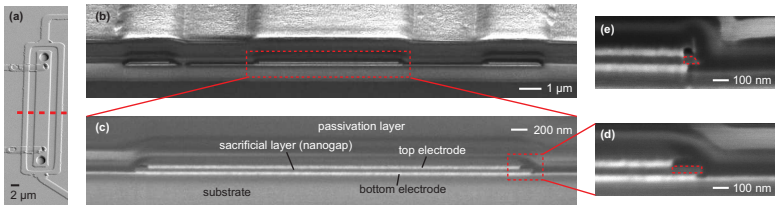

Figure 6.3: Scanning electron microscopy images from a 52° viewing angle. (a) Image of a complete device. (b), (c) and (d) Cross-sections at different magnifications. The device was cut open using a focused ion beam along the line indicated by the dashed line in (a). (b) Shows the complete overview, (c) shows a zoom of the nanochannel, and (d) shows the dead volume region at high magnification. (e) Cross-section of a different device with optimized etching procedure. The areas outlined with red dotted lines in (d) and (e) represent the dead volume.

6.2.2 Single-molecule detection in aqueous solution

Single-molecule detection experiments were based on amperometry under redox cycling conditions in the presence of a concentration C = 10 pM of redox species; the number of analyte molecules in the detection region is then on average $\langle N \rangle = CVN_A = 0.06$, where $V = 1 \times 10^{-17}\mathrm{m}^3$ is the volume of the nanochannel between the two electrodes and N_A is Avogadro's number. Figure 6.1 c illustrates the results of this measurement in the form of current-time traces that were recorded simultaneously through the two electrodes of a nanogap transducer filled with an aqueous solution of 10 pM (ferrocenylmethyl)trimethylammonium bromide (FcTMABr) in 0.1 M KCl. The top and bottom electrodes were biased at potentials of $E_t = 0.5$ V and $E_b = 0.35$ V, respectively. Because the formal potential for $FcTMA^+$ is $E^{0'} = 0.43$ V, the given potentials correspond to oxidizing and reducing potentials, respectively, thus enabling redox cycling. The traces mostly exhibit a background current which is constant within the noise level determined by the measurement electronics. At randomly occurring intervals, however, anti-correlated step-like features are observed in the current. Each of these events corresponds to a single molecule entering the active region by Brownian motion, shuttling $\sim 10^5$ electrons from the bottom to the top electrode by redox cycling, and exiting the active region again.[14] The opposite signs for the steps observed at the top and bottom electrodes correspond to oxidizing and reducing currents, respectively, as expected (additional control experiments supporting our conclusion that the steps originate from single-molecule fluctuations are given in Appendix C).

We note that it would be practically impossible to detect an analyte concentration as low as 10 pM by cyclic voltammetry - even with the help of efficient redox-cycling amplification provided by nanogaps - because the corresponding

fA-level currents would be dwarfed by unwanted background reactions involving water and oxygen. It is the step-like, discrete nature of the single-molecule events that allows extracting their contribution from the background currents.

The current per molecule in Figure 6.1 c, which corresponds to the height of the single-molecule current plateaus, is observed to be ∼7 fA. This corresponds to a signal-to-noise ratio (SNR) of 2.3, where we define the SNR as the ratio of the current step height to the standard deviation of the measured background current. How does this measured step height compare to theoretical expectations? In the presence of excess supporting electrolyte, as is the case here, mass transport of the analyte molecules is purely diffusive and the current per molecule, i_p, has the general form

$$i_p = i_{\mathrm{p,ideal}} \chi_{\mathrm{bias}} \chi_{\mathrm{geom}} \chi_{\mathrm{ads}} \tag{6.1}$$

here $i_{\mathrm{p,ideal}}$ represents the maximum expected current for pure diffusion and has the value $i_{\mathrm{p,ideal}} = e/2\tau$, where -$e$ is the electron charge, $\tau = z^2/2D$ is the average time a molecule takes to diffuse across the gap, z is again the distance between the electrodes and D is the diffusion coefficient of the redox species.[20] In the case where the diffusion coefficients of the reduced (D_{red}) and oxidized (D_{ox}) forms are unequal,[21] $D = 2D_{\mathrm{red}}D_{ox}/(D_{\mathrm{red}}+D_{ox})$. For aqueous solutions of the analytes studied here the difference between D_{ox} and D_{red} is however small and we ignore it for simplicity. χ_{bias}, χ_{geom} and χ_{ads} are dimensionless numerical coefficients that represent the signal reduction from the electrode bias, the device geometry (in particular any dead volume) and analyte adsorption to surfaces in the device, respectively:

- The value of χ_{bias} is given, under the assumption of Nernst equilibrium at the two electrodes,[22] by

$$\chi_{\mathrm{bias}} = \left| \frac{1}{1 + e^{-e(E_t - E^{0\prime})/KT}} - \frac{1}{1 + e^{-e(E_b - E^{0\prime})/KT}} \right| \tag{6.2}$$

  here k is the Boltzmann constant, T is the absolute temperature and the potentials are as defined above. Deviations are possible due to the finite rate of electron transfer at the electrodes, but this is only a small correction for the fast redox couples employed here.[15] In principle one can always insure that χ_{bias} has its maximum value of unity by applying sufficient reducing and oxidizing overpotentials at the two electrodes. With analyte concentrations as low as 10 pM, however, it is extremely difficult to remove all background contaminants, so a narrower potential window (100 - 150 mV) was usually employed to minimize any potential interference from such contaminants. In practice, χ_{bias} was determined from the cyclic voltammogram measured with a 5 μm radius ultramicroelectrode in a 1 mM analyte solution in 0.1 M KCl.

- The value of χ_{geom} represents the fact that shuttling time is lost when an analyte molecule enters the dead volume, effectively reducing the current per molecule (as shown in Appendix C). For linear, channel-shaped devices as discussed here, its value is simply given by the ratio of the width of the active region to the width of the fluid-filled nanochannel; for devices with minimal dead volume, such as that shown in Figure 6.3 e, it has a value $\chi_{\mathrm{geom}} = 0.97$.
- Because of the high surface-to-volume ratio of nanogap devices, adsorption can play a large role.[16, 23–25] The value of χ_{ads} is given by $\chi_{\mathrm{ads}} = (1+ \tau_{\mathrm{ads}}/\tau)^{-1}$, where τ_{ads} represents the average time per half cycle spent by an analyte molecule adsorbed to the electrodes.

For the case of Figure 6.1 c, where $D = 5.0 \times 10^{-6}\,\mathrm{cm}^2/\mathrm{s}$ and $z = 40\,\mathrm{nm}$, Equation 6.1 yields $\mathrm{i_{p,ideal}} = 50\,\mathrm{fA}$. Further correcting for $\chi_{\mathrm{bias}} = 0.90$ and $\chi_{\mathrm{geom}} = 0.92$ yields an expected current per molecule of 41 fA. This is significantly higher than the observed steps height, $i_p = 7\,\mathrm{fA}$, indicating a substantial degree adsorption with $\chi_{\mathrm{ads}} = 0.17$. This corresponds to each molecule spending more than 80% of its time adsorbsed at the electrodes. This level of adsorption is typical for ferrocene derivatives in nanogap devices as determined from high-concentration electrochemical spectroscopy methods.[23, 24] Single-molecule measurements in acetonitrile also found substantial suppression of the current due to adsorption with $\chi_{\mathrm{ads}} = 0.32$.[24] The current per molecule observed here is thus consistent with expectations.

In order to test the broader applicability of single-molecule detection in our nanogaps, we performed detection experiments for two other commonly employed redox mediators, namely, ferrocenedimethanol ($\mathrm{Fc(MeOH)_2}$, $E^{0'} = 0.25\,\mathrm{V}$) and ferricyanide ($\mathrm{Fe(CN)_6}^{3-}$, $E^{0'} = 0.23\,\mathrm{V}$). Figures 6.4 a-6.4 c show amperometry results for 10 pM FcTMABr, $\mathrm{Fc(MeOH)_2}$ and $\mathrm{K_3[Fe(CN)_6]}$ in 0.1 M KCl as supporting electrolyte at room temperature (22 °C) under redox conditions ($E_t = 0.5$ V and $E_b = 0.35$ V for $\mathrm{FcTMA^+}$, $E_t = 0.3$ V and $E_b = 0.2$ V for $\mathrm{Fc(MeOH)_2}$, $E_t = 0.3$ V and $E_b = 0.15$ V for $\mathrm{Fe(CN)_6}^{3-}$). In each case events with a height 5 - 7 fA were observed. Taking into account the different values of the diffusion coefficient D, χ_{bias} and χ_{geom} in each case, as summarized in Table 6.1, this indicates different degrees of adsorption for these three compounds. In particular, $\mathrm{FcTMA^+}$ and $\mathrm{Fe(CN)_6}^{3-}$ show similar degrees of adsorption, with χ_{ads} having a value of 0.12 and 0.10, respectively, while $\mathrm{Fc(MeOH)_2}$ exhibits the least adsorption with $\chi_{\mathrm{ads}} = 0.21$.

Because of the large influence of adsorption on the current per molecule, reducing adsorption can cause a significant improvement in i_p and the SNR. Since spectroscopic measurements indicate reduced adsorption of ferrocene derivatives at higher temperatures,[21] we expected that an increase in temperature would result in increased values for i_p. To test this hypothesis, we performed measurements at elevated temperatures. Amperometry results at 37 °C, while keeping

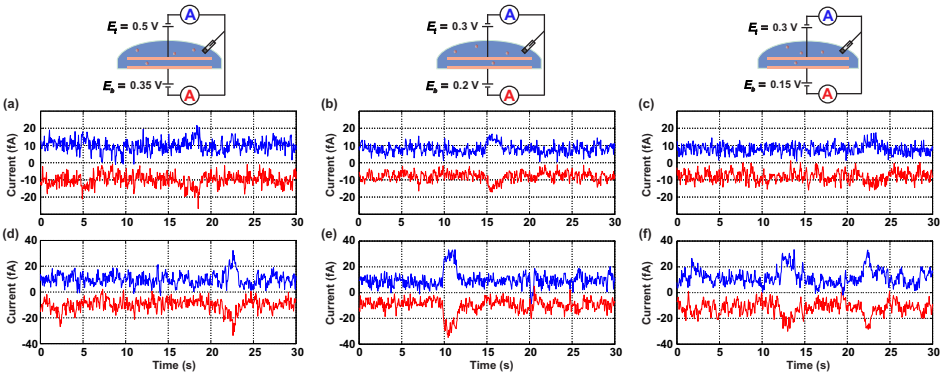

Figure 6.4: Bias schemes and current-time traces for single-molecule detection in (a,d) 10 pM FcTMABr in 0.1 M KCl, (b,e) 10 pM $Fe(MeOH)_2$ in 0.1 M KCl, and (c,f) 10 pM $K_3[Fe(CN)_6]$ in 0.1 M KCl. The top and bottom rows were measured at 22 °C and 37 °C, respectively. The traces have been vertically offset for clarity.

Temperature	Quantity	$FcTMA^+$	$Fe(MeOH)_2$	$Fe(CN)_6{}^{3-}$
	χ_{geom}	0.92	0.80	0.92
22 °C	χ_{bias}	0.88	0.75	0.88
	D (cm^2/s)	5.0×10^{-6}	5.6×10^{-6}	6.0×10^{-6}
	i_p (fA)	5 ±1	7 ±1	5 ±1
	$i_{p,ideal}$ (fA)	50	56	60
	$i_{p,ideal}\chi_{bias}\chi_{geom}$ (fA)	40	34	49
	χ_{ads}	0.13 ±0.02	0.21 ±0.03	0.10 ±0.02
37 °C	χ_{bias}	0.87	0.69	0.82
	D (cm^2/s)	7.0×10^{-6}	7.8×10^{-6}	8.4×10^{-6}
	i_p (fA)	14 ±2	20 ±2	15 ±2
	$i_{p,ideal}$ (fA)	70	78	84
	$i_{p,ideal}\chi_{bias}\chi_{geom}$ (fA)	56	43	63
	χ_{ads}	0.25 ±0.03	0.47 ±0.04	0.24 ±0.03

Table 6.1: Theoretical and measured values in Equation 6.1 for single-molecule measurement with $FcTMA^+$, $Fe(MeOH)_2$ and $Fe(CN)_6{}^{3-}$ at 22 °C and 37 °C.

the other parameters identical to those in Figure 6.4 a-6.4 c, are shown in Figures 6.4 d-6.4 f. A systematic increase of i_p by a factor of ∼3 was observed for each measurement while the background current noise was essentially unchanged. A factor of 1.4 increase in i_p can be attributed to the increase in diffusion coefficient, while the remaining factor of 1.5-3 is attributed to reduced adsorption, consistent with the spectroscopic measurements. The increase of i_p was accompanied by a

shortening of the average duration of the events, which is also consistent with reduced adsorption: the average time for a molecule to diffuse along the channel becomes shorter if it spends less time being immobilized on the electrode.

These experiments demonstrate unambiguously the ability of nanogap transducers to detect individual molecules in water. Naturally, only events with duration longer than the response time of the measurement electronics can be resolved. Because we relied on Brownian motion to bring molecules in and out of the detection region, however, we expect that many events may be much shorter; such events are not individually recognized but instead appear as noise in the baseline.[14, 26, 27] In the future we expect that advection of the sample solution through the nanogap transducer can overcome this difficulty.[26–29] In addition, functionalizing the electrode surface to minimize fouling and adsorption could greatly improve the performance and reliability of the transducer.[24, 30–32]

6.3 Conclusions

We have demonstrated a new self-aligned method for the fabrication of nanogap transducers that allows wafer-scale manufacturing of devices with 40 nm electrode spacing and sub-100 nm dead volume using conventional optical lithography with relatively poor (1 μm) alignment tolerances. The resulting gains in redox-cycling efficiency allowed us to detect for the first time individual redox molecules in aqueous solution using nanofluidic transducers, raising the possibility of new assays based on single-molecule fingerprinting. The robustness of the technique was demonstrated using different common analytes, namely $FcTMA^+$, $Fc(MeOH)_2$ and $Fe(CN)_6{}^{3-}$. It was further shown that the magnitude of the single-molecule signal can be increased by mitigating analyte adsorption.

References

[1] Walter, N. G., Huang, C. Y., Manzo, A. J. and Sobhy, M. A., Do-It-Yourself Guide: How to Use the Modern Single-Molecule Toolkit. *Nat. Methods*, **2008**, *5*, 475-489.

[2] Hinterdorfer, P. and Van Oijen, A., *Handbook of Single-Molecule Biophysics*, Springer: Dordrecht ; New York, **2009**.

[3] Walt, D. R., Optical Methods for Single Molecule Detection and Analysis, *Anal. Chem.*, **2013**, *85*, 1258-1263.

[4] Haas, P.; Then, P., Wild, A., Grange, W., Zorman, S., Hegner, M., Calame, M., Aebi, U., Flammer, J. and Hecht, B., Fast Quantitative Single-Molecule Detection at Ultralow Concentrations, *Anal. Chem.*, **2010**, *82*, 6299-6302.

[5] Li, W., Bell, N. A. W., Hernez-Ainsa, S., Thacker, V. V., Thackray, A. M., Bujdoso, R. and Keyser, U. F., Single Protein Molecule Detection by Glass Nanopores. *ACS nano*, **2013**, *7*, 4129-4134.

[6] Rajendran, A., Endo, M. and Sugiyama, H., Single-Molecule Analysis Using DNA Origami, *Angew. Chem. Int. Ed.*, **2012**, *51*, 874-890.

[7] Witters, D., Knez, K., Ceyssens, F., Puers, R. and Lammertyn, J., Digital Microfluidics-Enabled Single-Molecule Detection by Printing and Sealing Single Magnetic Beads in Femtoliter Droplets, *Lab Chip*, **2013**, *13*, 2047-2054.

[8] Kalisky, T. and Quake, S. R., Single-Cell Genomics, *Nat. Methods*, **2011**, *8*, 311-314.

[9] Yin, H. and Marshall, D., Microfluidics for Single Cell Analysis, *Curr. Opin. Biotechnol.*, **2012**, *23*, 110-119.

[10] Eid, J., Fehr, A., Gray, J., Luong, K., Lyle, J., Otto, G., Peluso, P., Rank, D., Baybayan, P., Bettman, B. and *et al.*, Real-Time DNA Sequencing from Single Polymerase Molecules, *Science*, **2009**, *323*, 133-138.

[11] Wang, J., Electrochemical Biosensors: Towards Point-of-Care Cancer Diagnostics. *Biosens. Bioelectron.*, **2006**, *21*, 1887-1892.

[12] White, R. J., Kallewaard, H. M., Hsieh, W., Patterson, A. S., Kasehagen, J. B., Cash, K. J., Uzawa, T., Soh, H. T. and Plaxco, K. W., Wash-Free, Electrochemical Platform for the Quantitative, Multiplexed Detection of Specific Antibodies, *Anal. Chem.*, **2012**, *84*, 1098-1103.

[13] Rothberg, J. M., Hinz, W., Rearick, T. M., Schultz, J., Mileski, W., Davey, M.; Leamon, J. H., Johnson, K., Milgrew, M. J., Edwards, M. and *et al.*, An Integrated Semiconductor Device Enabling Non-Optical Genome Sequencing, *Nature*, **2011**, *475*, 348-52.

[14] Zevenbergen, M. A. G., Singh, P. S., Goluch, E. D., Wolfrum, B. L. and Lemay, S. G., Stochastic Sensing of Single Molecules in a Nanofluidic Electrochemical Device, *Nano Lett.*, **2011**, *11*, 2881-2886.

[15] Zevenbergen, M. A. G., Wolfrum, B. L., Goluch, E. D., Singh, P. S. and Lemay, S. G., Fast Electron-Transfer Kinetics Probed in Nanofluidic Channels, *J. Am. Chem. Soc.*, **2009**, *131*, 11471-11477.

[16] Kang, S., Mathwig, K. and Lemay, S. G., Response Time of Nanofluidic Electrochemical Sensors, *Lab Chip*, **2012**, *12*, 1262-1267.

[17] Kätelhön, E., Hofmann, B., Lemay, S. G., Zevenbergen, M. A. G., Offenhäusser, A. and Wolfrum, B., Nanocavity Redox Cycling Sensors for the Detection of Dopamine Fluctuations in Microfluidic Gradients. *Anal. Chem.*, **2010**, *82*, 8502-8509.

[18] Faßbender, F., Schmitt, G., Schöning, M. J., Lüth, H., Buß, G. and Schultze, J. W., Optimization of Passivation Layers for Corrosion Protection of Silicon-Based Microelectrode Arrays, *Sens. Actuators, B*, **2000**, *68*, 128-133.

[19] Schmitt, G., Schultze, J. W., Faßbender, F., Buß, G., Lüth, H. and Schöning, M. J., Passivation and Corrosion of Microelectrode Arrays, *Electrochim. Acta*, **1999**, *44*, 3865-3883.

[20] Fan, F. R. F. and Bard, A. J., Electrochemical Detection of Single Molecules, *Science*, **1995**, *267*, 871-874.

[21] Mampallil, D., Mathwig, K., Kang, S. and Lemay, S. G., Redox Couples with Unequal Diffussion Coefficients: Effect on Redox Cycling. *Anal. Chem.*, **2013**, *85*, 6053-6058.

[22] Bard, A. j. and Faulkner, L. R., *Electrochemical Methods: Fundamentals and Applications*, John Wiley & Sons: New York, **2001**, pp31-32.

[23] Zevenbergen, M. A. G., Singh, P. S., Goluch, E. D., Wolfrum, B. L. and Lemay, S. G., Electrochemical Correlation Spectroscopy in Nanofluidic Cavities, *Anal. Chem.*, **2009**, *81*, 8203-8212.

[24] Singh, P. S., Chan, H. S. M., Kang, S. and Lemay, S. G., Stochastic Amperometric Fluctuations as a Probe for Dynamic Adsorption in Nanofluidic Electrochemical Systems, *J. Am. Chem. Soc.*, **2011**, *133*, 18289-18295.

[25] Mathwig, K. and Lemay, S. G., Mass Transport in Electrochemical Nanogap Sensors, *Electrochim. Acta*, **2013**, *112*, 943-949.

[26] Singh, P. S., Katelhon, E., Mathwig, K., Wolfrum, B. and Lemay, S. G., Stochasticity in Single-Molecule Nanoelectrochemistry: Origins, Consequences, and Solutions, *ACS Nano*, **2012**, *6*, 9662-9671.

[27] Lemay, S. G., Kang, S., Mathwig, K. and Singh, P. S., Single-Molecule Electrochemistry: Present Status and Outlook, *Acc. Chem. Res.*, **2013**, *46*, 369-77.

[28] Mathwig, K., Mampallil, D., Kang, S. and Lemay, S. G., Electrical Cross-Correlation Spectroscopy: Measuring Picoliter-Per-Minute Flows in Nanochannels, *Phys. Rev. Lett.*, **2012**, *109*, 118302.

[29] Mathwig, K. and Lemay, S. G., Pushing the Limits of Electrical Detection of Ultralow Flows in Nanofluidic Channels, *Micromachines*, **2013**, *4*, 138-148.

[30] Porter, M. D., Bright, T. B., Allara, D. L. and Chidsey, C. E. D., Spontaneously Organized Molecular Assemblies. 4. Structural Characterization of N-Alkyl Thiol Monolayers on Gold by Optical Ellipsometry, Infrared Spectroscopy, and Electrochemistry, *J. Am. Chem. Soc.*, **1987**, *109*, 3559-3568.

[31] Finklea, H. O., Avery, S., Lynch, M. and Furtsch, T., Blocking Oriented Monolayers of Alkyl Mercaptans on Gold Electrodes, *Langmuir*, **1987**, *3*, 409-413.

[32] Picher, M. M., Kupcu, S., Huang, C. J., Dostalek, J., Pum, D., Sleytr, U. B. and Ertl, P., Nanobiotechnology Advanced Antifouling Surfaces for the Continuous Electrochemical Monitoring of Glucose in Whole Blood Using a Lab-on-a-Chip, *Lab Chip*, **2013**, *13*, 1780-1789.

Chapter 7

Single-Molecule Electrochemistry in Nanochannels: Probing the First-Passage Time

The diffusive mass transport of individual redox molecules was probed experimentally in microfabricated nanogap transducers. The first-passage times of single molecules exiting a detection region were extracted and the resulting distribution was compared with quantitative analytical predictions. The results suggest that different adsorption processes dominate at trace analyte levels.

The contents of this chapter are to be submitted to *JACS*.

7.1 Introduction

The ability to address and probe individual molecules has led to significant new insights on molecular transport and internal dynamics in fields ranging from molecular electronics to biophysics.[1, 2] It is thus of considerable interest to extend the range of single-molecule analysis methods to other transduction mechanisms such as electrochemistry. While single-molecule detection by electrochemical means has indeed been reported,[3–7] efforts so far have focused almost exclusively on demonstrating the basic ability to resolve single molecules and have not allowed for deeper analysis. This is largely due to the experimental challenge inherent in measuring the extremely small signal levels associated with single-molecule faradaic processes.

Here we demonstrate for the first time the ability to statistically analyse the diffusive dynamics of individual molecules using an electrochemical method. We focus on the distribution of residence times for molecules randomly entering and leaving a nanofluidic cavity, an inherently single-molecule property. The residence time corresponds to a well-studied quantity in stochastic systems, the so-called first-passage time,[8] which appears in diverse fields including ecology,[9] biophysics,[10–12] finance,[13] diffusion-controlled chemical reactions,[14] etc,[15] and which permits a quantitative comparison with theory. This detailed analysis is made possible through the use of redox cycling in nanogap transducers,[6] which robustly yield extensive, high-quality single-molecule data.

7.2 Results and Discussion

The nanogap device is sketched in Figure 7.1 a. It consists of two electrodes with a length $L = 50\ \mu$m and a width of 4 or 5 μm that are separated by a solution-filled gap of 40 nm. The device was micro-fabricated using optical lithography, as described earlier:[6] In brief, a stack of metal layers was first deposited and patterned on a 4-inch Si wafer, followed by ion-beam etching (IBE) and subsequent wet etching to define the active nanogap detecting region. Afterwards a final metal layer sandwiched between two passivation layers was deposited and patterned to provide electrical connections. Finally, access holes for liquid were created by etching through the passivation and top electrode. Immediately before use the sacrificial layer was wet-etched *via* the access holes, releasing the nanochannel. An optical microscope image of a complete device and a scanning electron microscope image of the nanogap cross section are shown in Figures 7.1 b and 7.1 c, respectively.

The measurements were performed by interfacing the device with an external reservoir containing an aqueous solution with a concentration $C = 10$ pM of redox species and 0.1 M KCl as supporting electrolyte. The average number of analyte

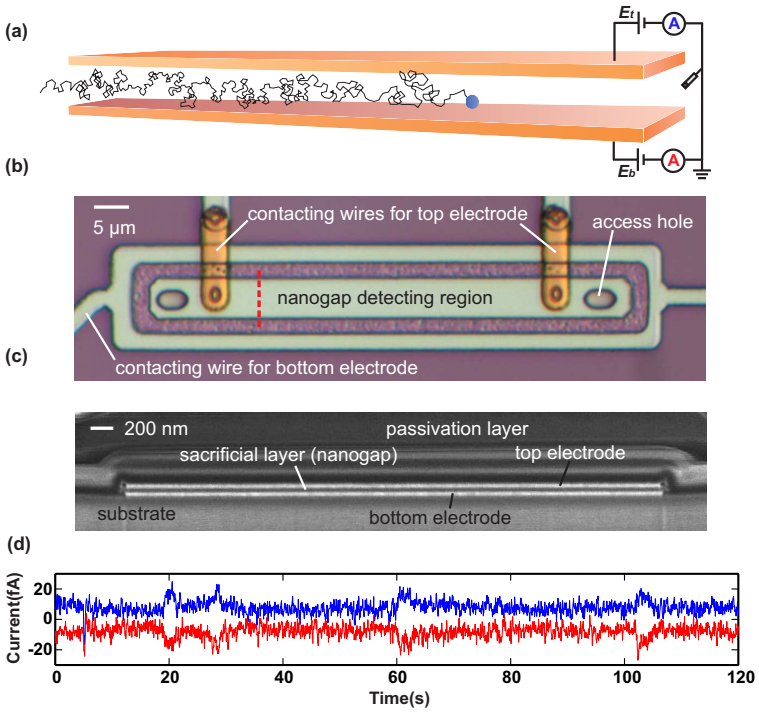

Figure 7.1: (a) Schematic illustration of a nanogap device. (b) Optical microscope image (top view) of a device. (c) Scanning electron microscopy image of the cross section of a device from a 52° viewing angle. The device was cut open using a focused ion beam along the line indicated by the dashed line in (b). (d) Current-time traces simultaneously measured at the top (blue) and bottom (red) electrodes (5 μm wide) under redox-cycling conditions (E_t = 0.5 V and E_b = 0.35 V, 10 pM FcTMABr in 0.1 M KCl aqueous solution). The traces have been offset vertically for clarity.

molecules in solution in the detection region was then $<N> = CVN_A = 0.05$ for a device with a width of 4 μm, where $V = 8 \times 10^{-18}$ m^3 is the volume of the nanogap region and N_A is Avogadro's number. For a 5 μm wide device, $<N> = 0.06$ under the same conditions. For such low occupancy, the fraction of the time that the device is occupied by two or more molecules at the same time is low ($< 0.2\%$) based on Poisson statistics.

For single-molecule experiments, the bottom and top electrodes were biased at reducing and oxidizing potentials, respectively. Under these redox-cycling conditions, each chemically reversible redox molecule present in the nanogap is repeatedly oxidized and reduced as it undergoes Brownian motion, generating faradaic currents of opposite polarity at the two electrodes. These reduction and oxidation currents were measured simultaneously; each time that a molecule randomly entered and subsequently exited the nanochannel, current steps with magnitudes

of order 10^{-14} A and opposite signs were observed in the measured currents. This is illustrated in Figure 7.1 d, which shows a time trace with four distinctly recognizable single-molecule events with durations of the order of a few seconds.

In order to achieve sufficient sensitivity to detect these extremely low currents, current-to-voltage converters with 10^{12} V/A trans-impedance gain and a response time of 350 ms (10% - 90% rise time) were employed.[16] Such a slow response is essentially unavoidable due to the inverse relationship between gain and measurement bandwidth in high-gain amplifiers. Consequently, and as discussed further below, only events lasting longer than ∼450 ms could be reliably resolved.

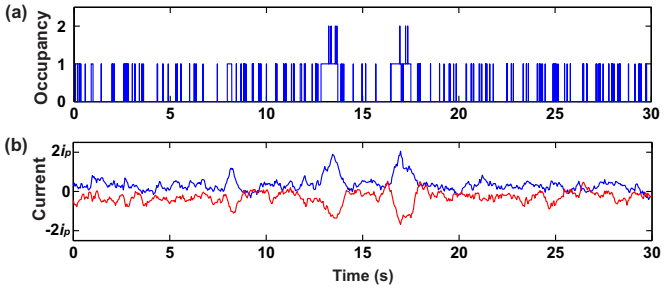

Figure 7.2: (a) Simulated occupancy-time trace for an average occupancy $<N> = 0.1$. (b) Corresponding simulated current-time trace including additive Gaussian noise and filtered to account for the influence of the measurement electronics.

To ascertain the feasibility of identifying events and determining their durations from the data, we performed 1D random walk simulations of individual single-molecule trajectories.[17] Figure 7.2 a shows a typical trace of the device occupancy versus time for an average occupancy $<N> = 0.1$. Most events are very short, with only a minority of events having durations of the order of seconds. To simulate the role of the measurement electronics, white noise was added to the simulation results and the resulting traces were convolved with a first-order impulse response with a time constant of $\tau = 350$ ms, the resulted trace is shown in Figure 7.2 b. Events with a duration of order 1 s reach (or exceed, because of noise) the full single-molecule current, i_p; such events exhibit a trapezoid shape, with a full width at half-maximum that agrees within ±10% the duration of the underlying event in Figure 7.2 a. Longer events (not shown) instead exhibit a well-defined plateau, while events with durations of order $\tau = 450$ ms or shorter contribute to the apparent noise in the current but cannot be reliably identified. Occasionally two long events are juxtaposed and cannot be distinguished, as illustrated in Figure 7.2 around 17 s. However, at this occupancy such occurrences –as well as occurrences of two long events overlapping in time– are rare, and they have minimal impact on overall statistics. Taken together, these simulation results suggest that it is feasible to accurately identify single-molecule events longer than $\tau = 450$ ms and to determine their duration.

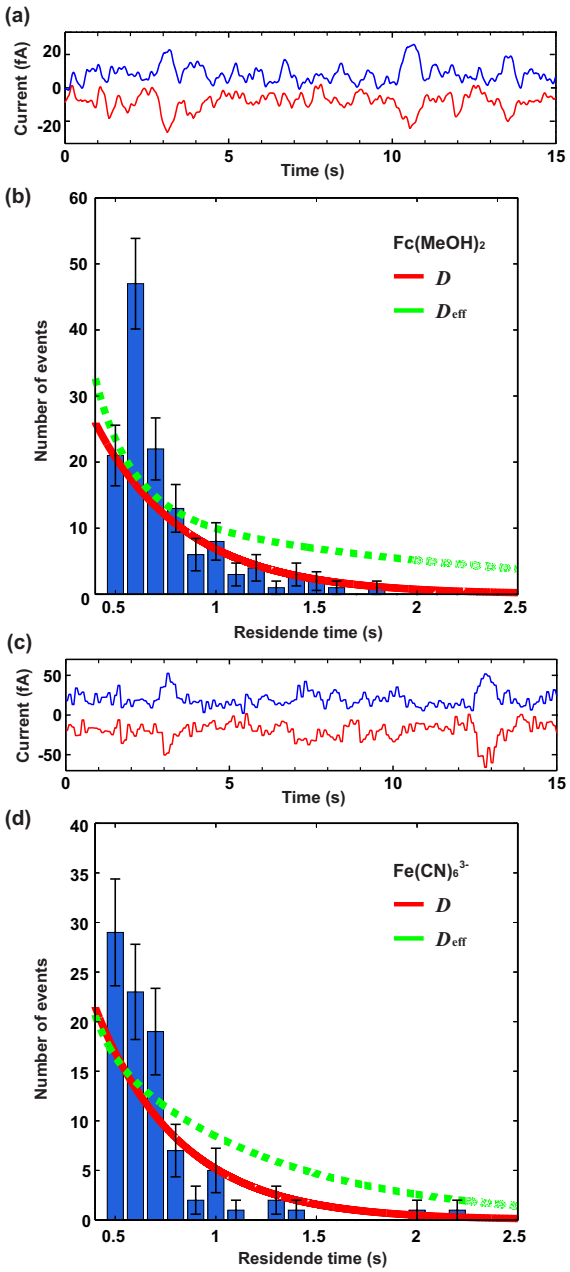

Figure 7.3: (a, c) Representative current-time traces for 10 pM $Fc(MeOH)_2$ and $Fe(CN)_6{}^{3-}$ in 0.1 M KCl under redox cycling conditions (E_t = 0.3 V, E_b = 0.2 V, $E^{0'}$ = 0.25 V and E_t = 0.3 V, E_b = 0.15 V, $E^{0'}$ = 0.23 V respectively). (b, d) Histograms (bin size $\gamma = 0.1$s) of observed event durations and corresponding theoretical predictions for the experimental conditions of (a) and (c). Events shorter than 450 ms were excluded as they could not be resolved reliably.

Extensive current-time traces, were recorded with aqueous solutions of 10 pM ferrocenedimethanol ($Fc(MeOH)_2$, $E^{0'} = 0.25$ V) and 10 pM ferricyanide ($Fe(CN)_6{}^{3-}$, $E^{0'} = 0.23$ V) in 0.1 M KCl under redox cycling conditions ($E_t = 0.3$ V, $E_b = 0.2$ V for $Fc(MeOH)_2$ and $E_t = 0.3$ V, $E_b = 0.15$ V for $Fe(CN)_6{}^{3-}$) in 4 μm and 5 μm wide devices, respectively, as shown in Figures 7.3 a and 7.3 c. Single-molecule events were identified and their durations were extracted from these data. Figure 7.3 b and 7.3 d show the histograms of event durations extracted from 26 min and 20 min long traces measured under the same conditions as Figures 7.3 a and 7.3 c, respectively. Events shorter than 450 ms were excluded from this analysis, yielding totals of 132 and 91 events for $Fc(MeOH)_2$ and $Fe(CN)_6{}^{3-}$, respectively. In both measurements, the histograms exhibit a sharply decreasing number of events with increasing event duration, with the majority of identifiable events having durations below 1 s.

The histograms in Figure 7.3 encapsulate detailed quantitative information about the statistics of individual single-molecule trajectories. Furthermore, because mass transport is purely diffusive at the high supporting electrolyte concentrations employed here, the form of the histograms can be predicted quantitatively from random-walk theory. This provides an unprecedentedly detailed test of electrochemical single-molecule data.

We have previously shown that, due to the devices' highly anisotropic geometry,[17] Brownian motion in nanogap transducers can be accurately modelled as a discrete 1D random walk with step size L/a, where L is the length of the device and a ($a >> 1$) is the number of grid points in the simulation.[17] The two edges of the simulation domain correspond to the two access holes of the device. Within such a model, a single-molecule event corresponds to a molecule starting at one edge of the simulation domain and taking a number of random steps inside the device, this process continuing until the molecule makes a final jump that takes it out of the simulation domain at either end. This process corresponds exactly to the so-called first-passage time of a particle undergoing a discrete random walk in a linear domain with absorbing boundaries at each end. The probability of the particle exiting after exactly n steps has the exact analytic form[18]

$$P(n) = \frac{1}{a}\sum_{\mu=1}^{a-1}\cos^{n-1}\frac{\pi\mu}{a}\sin\frac{\pi\mu}{a}\sin\frac{\pi\mu z}{a} + \frac{1}{a}\sum_{\mu=1}^{a-1}\cos^{n-1}\frac{\pi\mu}{a}\sin\frac{\pi\mu}{a}\sin\frac{\pi\mu(a-z)}{a} \qquad (7.1)$$

here z is the starting position of the particle ($1 \leq z \leq a$); we set $z = 1$ (or $z = a - 1$, which is equivalent from symmetry) to represent the starting position of the molecule near either access hole. The first term of the equation represents the probability that the particle exits from the same end as it entered and the second term from the opposite end. Equation 7.1 indicates that the most probable scenario is a molecule enters the nanochannel and exits from the same end within a few steps,[5, 17] such that the residence time is very short and cannot possibly be

resolved experimentally. In relatively rare cases the molecule penetrates further into the device, generating events that may be sufficiently long to be detected.

To compare theory with the experimental histogram data of Figure 7.3, we re-normalize Equation 7.1 to yield the average number of events in a histogram bin of width and centred at time t, $M(t)$:

$$M(t) = \frac{\gamma}{\Delta t} M_{\text{total}} P\left(n = \frac{t}{\Delta t}\right) \tag{7.2}$$

here $\Delta t = (L/a)^2/2D$ is the random-walk step time, D is the diffusion coefficient of the molecule, and M_{total} is the total number of events take place over the course of the measurement. The value of M_{total} is in turn obtained from $M_{\text{total}} = T<N>/\tau_0$, where T is the total duration of the measurement, $<N>$ is the average number of analyte molecules in the detection region, and τ_0 is the average duration of an event:

$$\tau_0 = \sum_{n=1}^{\infty} P(n) n \Delta t \tag{7.3}$$

Equations 7.1 - 7.3 represent a quantitative prediction for the histogram, $M(t)$, with the only inputs the device length, L, the diffusion coefficient, D, and the average occupancy, $<N>$. Predictions based on the bulk diffusion coefficient ($D = 5.6 \times 10^{-10}\,\text{m}^2/\text{s}$ for $D = 6.0 \times 10^{-10}\,\text{m}^2/\text{s}$, as determined from the diffusion-limited current at a 5 μm radius platinum ultramicroelectrode) and $<N>$ based on the 10 pM bulk concentration are shown as red curves in Figures 7.3 b and 7.3 d. In both cases the analytical calculation reproduces quite well with the experimental data, with both the absolute number of events per bin and the decrease in the number of events with increasing duration being comparable between calculation and experiment.

This good agreement however has subtle implications for our understanding of the microscopic dynamics of single redox molecules. We have previously reported that the species studied here undergo some degree of reversible adsorption at the electrodes.[6, 19, 20] This is manifested by a suppression of the single-molecule current i_p by a factor χ_{ads} (with $0 \leq \chi_{\text{ads}} \leq 1$) compared to its ideal, diffusion-limited value $i_{\text{p,ideal}} = eD/z^2$,[3] where $-e$ is the electron charge and z is the electrode spacing.* But reversible adsorption can also have a second consequence for mass transport, namely, that of decreasing the apparent diffusion coefficient along the channel, D_{eff}, below its value for unhindered diffusion in bulk solution, D.[17, 19, 21, 22] These two adsorption-induced effects are coupled: for the simplest model of adsorption in which adsorbed molecules are immobile on the electrode,

*Additional corrections are also included to take into account the electrode biases and the geometry of the device, as per Ref. [6].

$D_{\text{eff}} = \chi_{\text{ads}} D$.[6, 19] The amperometric data illustrated in Figure 7.3 a and 7.3 c yield $\chi_{\text{ads}} = 0.3$ and 0.5 for $Fc(MeOH)_2$ and $Fe(CN)_6{}^{3-}$, respectively. Replacing D with the corresponding values of D_{eff} in Equations 1-3 yields the dashed green curves in Figures 7.3 b and 7.3 d; consistent with intuition, slower diffusion along the channel leads to a higher occurrence of long events in theory. Interestingly, however, these predictions do not agree well with the data, as significantly more long events are predicted than are observed in the experiment.

In its most literal interpretation, the observation that the histograms fit well with calculations using the bulk diffusion coefficient D but not with those using D_{eff} suggests that molecules adsorbed to the electrodes can diffuse along the channel without being slowed down substantially. In such a scenario the shuttling rate between the two electrodes is influenced by adsorption but the residence time inside the active region is not, as per the experimental findings. Surface diffusion of adsorbents has been studied in a variety of systems,[23–27] in particular using single-molecule fluorescence techniques. In some cases adsorbed molecules occupy specific binding sites but are able to move between binding sites,[27] qualitatively consistent with our observations. On the other hand, adsorption studies in nanogaps based on power spectral density (PSD) analysis[19] and transient chronoamperometric response[21, 22] yield unambiguous evidence of an effective slowing down of Brownian motion at 1 μM or higher concentrations (five or more orders of magnitude higher than the concentration employed here). This would imply that facile hopping between binding sites is possible, but only at extremely low surface concentrations (presumably due to most binding sites remaining unoccupied). Such a reduction of surface diffusion coefficient of adsorbed molecules at solid/liquid interfaces with increasing adsorbed concentration has been reported in experiments with macromolecules.[28, 29]

An alternate interpretation is that D_{eff} is indeed the correct diffusion coefficient, in which case an additional mechanism must be invoked to explain the missing long events when compared to the theoretical predictions. Decay of the molecules on the scale of seconds would provide such a mechanism. This can however be ruled out on the basis that the species under study are stable, for example the oxidized form of ferrocene derivatives having a lifetime on the order of an hour.[30–33] Another hypothesis is the existence of deep trap sites at which molecules can remain adsorbed for several tenths of seconds, causing long events to be replaced by a succession of shorter –yet still resolvable– events due to repeated binding/unbinding at these sites. Since clustering of long events has not been observed in the measurements, however, we tentatively rule out this interpretation.

7.3 Conclusions

In summary, first-passage times of individual redox molecules were probed using electrochemical nanogap devices and their statistical distribution was compared with analytical calculations. The results suggest that single molecules undergo facile surface diffusion while adsorbed to the electrode surface, in contrast with behavior at high surface concentrations. This is the first time that mass transport is characterized with single-molecule resolution using an electrochemical method.

References

[1] Walter, N. G., Huang, C. Y., Manzo, A. J. and Sobhy, M. A., Do-it-yourself Guide: How to Use the Modern Single-Molecule Toolkit, *Nat. Methods*, **2008**, *5*, 475-489.

[2] Walt, D. R., Optical Methods for Single Molecule Detection and Analysis, *Anal. Chem.*, **2013**, *85*, 1258-1263.

[3] Fan, F. R. F. and Bard, A. J., Electrochemical Detection of Single Molecules, *Science*, **1995**, *267*, 871-874.

[4] Sun, P. and Mirkin, M. V., Electrochemistry of Individual Molecules in Zeptoliter Volumes, *J. Am. Chem. Soc.*, **2008**, *130*, 8241-8250.

[5] Zevenbergen, M. A. G., Singh, P. S., Goluch, E. D., Wolfrum, B. L. and Lemay, S. G., Stochastic Sensing of Single Molecules in a Nanofluidic Electrochemical Device, *Nano Lett.*, **2011**, *11*, 2881-2886.

[6] Kang, S., Nieuwenhuis, A. F., Mathwig, K., Mampallil, D. and Lemay, S. G., Electrochemical Single-molecule Detection in Aqueous Solution Using Self-Aligned Nanogap Transducers, *ACS Nano*, **2013**, *7*, 10931-10937.

[7] Lemay, S. G., Kang, S., Mathwig, K. and Singh, P. S., Single-molecule Electrochemistry: Present Status and Outlook, *Accounts Chem. Res.*, **2013**, *46*, 369-377.

[8] Redner, S., *A Guide to First-passage Processes*, Cambridge University Press: Cambridge, **2001**.

[9] Fauchald, P. and Tveraa, T., Using First-passage Time in the Analysis of Area-Restricted Search and Habitat Selection, *Ecology*, **2003**, *84*, 282-288.

[10] Goychuk, I. and Hanggi, P., Ion Channel Gating: A First-passage Time Analysis of the Kramers Type, *PNAS*, **2002**, *99*, 3552-3556.

[11] van Hijkoop, V. J., Dammers, A. J., Malek, K. and Coppens, M. O., Water Diffusion through a Membrane Protein Channel: A First Passage Time Approach, *J. Chem. Phys.*, **2007**, *127*.

[12] Rajani, V., Carrero, G., Golan, D. E., de Vries, G, and Cairo, C. W., Analysis of Molecular Diffusion by First-passage Time Variance Identifies the Size of Confinement Zones, *Biophys. J.*, **2011**, *100*, 1463-1472.

[13] Mcdonald, R. and Siegel, D., The Value of Waiting to Invest, *Q. J. Econ.*, **1986**, *101*, 707-727.

[14] Szabo, A., Schulten, K. and Schulten, Z., 1st Passage Time Approach to Diffusion Controlled Reactions, *J. Chem. Phys.*, **1980**, *72*, 4350-4357.

[15] Hofler, L. and Gyurcsanyi, R. E., Nanosensors Lost in Space. A Random Walk Study of Single Molecule Detection with Single-Nanopore Sensors, *Anal. Chim. Acta.*, **2012**, *722*, 119-126.

[16] *Datasheet, FEMTO DDPCA-300 Variable Gain Sub Femto Ampere Current Amplifier.*

[17] Singh, P. S., Katelhon, E., Mathwig, K., Wolfrum, B. and Lemay, S. G., Stochasticity in Single-molecule Nanoelectrochemistry: Origins, Consequences, and Solutions, *ACS Nano*, **2012**, *6*, 9662-9671.

[18] Feller, W., *An Introduction to Probability Theory and Its Applications, 3rd ed.*, Wiley: New York, **1968**.

[19] Zevenbergen, M. A. G., Singh, P. S., Goluch, E. D., Wolfrum, B. L. and Lemay, S. G., Electrochemical Correlation Spectroscopy in Nanofluidic Cavities, *Anal. Chem.*, **2009**, *81*, 8203-8212.

[20] Singh, P. S., Chan, H. S. M., Kang, S. and Lemay, S. G., Stochastic Amperometric Fluctuations as a Probe for Dynamic Adsorption in Nanofluidic Electrochemical Systems, *J. Am. Chem. Soc.*, **2011**, *133*, 18289-18295.

[21] Kang, S., Mathwig, K. and Lemay, S. G., Response Time of Nanofluidic Electrochemical Sensors, *Lab Chip*, **2012**, *12*, 1262-1267.

[22] Mathwig, K. and Lemay, S. G., Mass Transport in Electrochemical Nanogap Sensors, *Electrochim. Acta*, **2013**, *112*, 943-949.

[23] Tilton, R. D., Robertson, C. R. and Gast, A. P., Lateral Diffusion of Bovine Serum-albumin Adsorbed at the Solid Liquid Interface, *J. Colloid. Interf. Sci.*, **1990**, *137*, 192-203.

[24] Unwin, P. R. and Bard, A. J., Scanning Electrochemical Microscopy. 14. Scanning Electrochemical Microscope Induced Desorption - A New Technique for the Measurement of Adsorption Desorption-Kinetics and Surface-

Diffusion Rates at the Solid Liquid Interface, *J. Phys. Chem.*, **1992**, *96*, 5035-5045.

[25] Roy, S., Thomas, J. M., Holmes, E. A., Kellis, J. T., Poulose, A. J., Robertson, C. R. and Gast, A. P., Simultaneous Observation of Enzyme Surface Diffusion and Surface Reaction Using Microfluidic Patterning of Substrate Surfaces, *Anal. Chem.*, **2005**, *77*, 8146-8150.

[26] Seebauer, E. G. and Allen, C. E., Estimating Surface-Diffusion Coefficients, *Prog. Surf. Sci.*, **1995**, *49*, 265-330.

[27] Gomer, R., Diffusion of Adsorbates on Metal-surfaces, *Rep. Prog. Phys.*, **1990**, *53*, 917-1002.

[28] Zhao, J. and Granick, S., Polymer Lateral Diffusion at the Solid-Liquid Interface, *J. Am. Chem. Soc.*, **2004**, *126*, 6242-6243.

[29] Chan, V., Graves, D. J., Fortina, P. and McKenzie, S. E., Adsorption and Surface Diffusion of DNA Oligonucleotides at Liquid/Solid Interfaces, *Langmuir*, **1997**, *13*, 320-329.

[30] Avron, M. and Shavit, N., A Sensitive and Simple Method for Determination of Ferrocyanide, *Anal. Biochem.*, **1963**, *6*, 549-554.

[31] Gao, Z. N., Han, X. X., Yao, H. Q., Liang, B. and Liu, W. Y., Electrochemical Oxidation of Isoniazid Catalyzed by (Fcm)Tma at the Platinum Electrode and Its Practical Analytical Application, *Anal. Bioanal. Chem.*, **2006**, *385*, 1324-1329.

[32] Prins, R., Korswage. A. R. and Kortbeek, A. G., Decomposition of Ferricenium Cation by Nucleophilic Reagents, *J. Organomet. Chem.*, **1972**, *39*, 335-334.

[33] Holecek, J., Handlir, K., Klikorka, J. and Dinhbang, N., Decomposition of Ferricenium Cation in Alkaline-Medium, *Collect. Czech Chem. C*, **1979**, *44*, 1379-1387.

Appendix A

A.1 Multi-potential-step chronoamperometry

Figure A.1 shows an experiment complementary to the one of Figure 4.3: The bottom electrode was kept at 0.5 V instead of 0 V while the potential of the top electrode was stepped. Current transients were observed when the top electrode potential was stepped to the base level of 0 V, which corresponds to diffusion-limited mass transport. The shape of the transient depended on the potential of the top electrode prior to the potential step, the magnitude of the transient fraction is larger for higher starting potentials. Specifically, when the potential of the top electrode was stepped from 0.4 V, 0.45 V and 0.5 V to 0 V, the current increased to 129 nA, 133 nA and 139 nA, respectively.

A.2 RC charging time of the device

Here we estimate the RC charging time when stepping the potential of the top electrode (geometry of the device of type L50H2 is used). The equivalent circuit for this case is shown in Figure A.2. The various parameters in Figure A.2, as well as estimates for their numerical values, are as follows:

- C_p is the capacitance between bulk solution and the electrode across its protective passivation layer. This protective passivation layer consists of a 90 nm/325 nm/90 nm thick SiO_2/SiN/SiO_2 stack. The total capacitance is therefore given by the individual capacitances contributed by these three layers connected in series. Using a relative permittivity of $\epsilon_r = 7$ for PECVD SiN, $\epsilon_r = 5$ for PECVD SiO_2, and an area A $\approx 1000\,\mu m^2$ (including 350

Supporting information of Chapter 4 is included in this appendix.

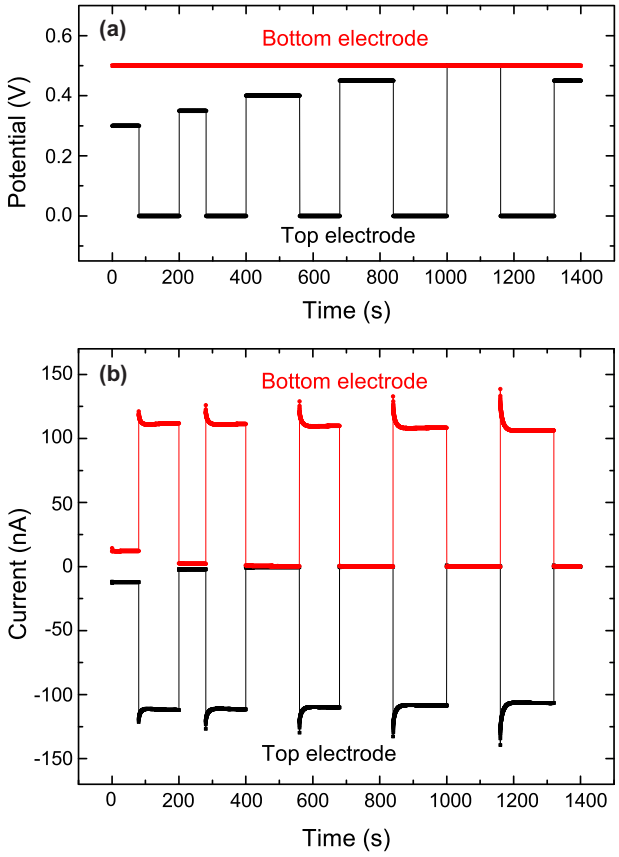

Figure A.1: Multi-potential-step chronoamperometry of a device of type L50H2 filled with an aqueous solution of 1 mM $Fc(MeOH)_2$ and 1 M KCl as supporting electrolyte. (a) Potentials applied as a function of time to the top (black) and bottom (red) electrode. (b) Corresponding current-time responses.

μm^2 for the top electrode itself and about 650 μm^2 for its contacting wire exposed to solution) yields a total capacitance $C_p \approx 0.1$ pF.

- C_d is the ionic double layer capacitance. At a given potential, the double layer capacitance per unit area is typically in the range of 10 to 40 $\mu F/cm^2$.[1] Using A = 175 μm^2, which is half of the top electrode area (for a symmetric device with two access holes), yields C_d in the range of 18 to 70 pF.

- R_a is the resistance of the cylindrical access hole given by $l/\kappa\pi r^2 = 16\,k\Omega$, where $l = 505$ nm is the depth of the access hole, $r = 1$ μm is its radius, and κ is the conductivity of the solution, which is 10.2 $\Omega^{-1}m^{-1}$ for 1 M KCl at 20 °C. The spreading resistance in the vicinity of the entrance hole contributes

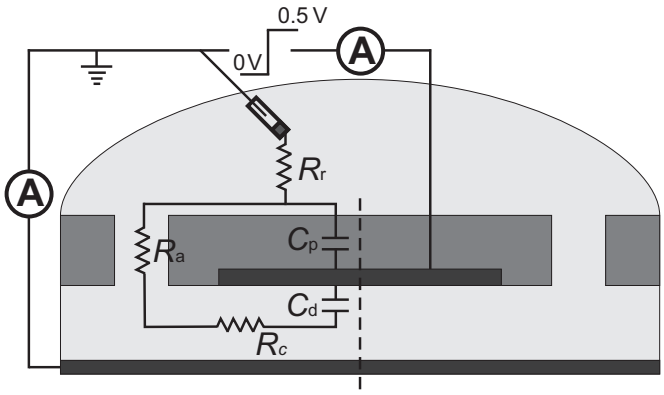

Figure A.2: Equivalent circuit diagram of the nanofluidic system.

an additional resistance $1/4\kappa r = 25\,\mathrm{k\Omega}$, for a total access resistance $R_a = 41\,\mathrm{k\Omega}$.

- R_r is the resistance of the bulk solution, R_r, is dominated by the spreading resistance in the region near the device. A rough estimate is $R_r = 1/4\kappa L = 500\,\Omega$, which indicates that it can be neglected.
- R_c is the resistance of (half of) the nanochannel, R_c, is equal to $L/\kappa hW = 7.6\,\mathrm{M\Omega}$, where $L = 27\,\mu\mathrm{m}$ is half of the length of the nanochannel, $h = 70\,\mathrm{nm}$ and $W = 5\,\mu\mathrm{m}$ are the height and width of the nanochannel, respectively.

The above indicates that the capacitance of the passivation layer is utterly negligible compared to the double-layer capacitance, despite the additional area relevant for C_p. Similarly, the resistance in series with the double layer capacitance is dominated by the nanochannel itself by virtue of its small cross-sectional area. An upper bound for the dominant RC time constant is therefore estimated as $\tau = (R_r + R_a + R_c)C_d = 0.53\,\mathrm{ms}$. This is orders of magnitude shorter than the transients observed in the experiments, indicating that the latter have a different origin. A corresponding calculation for the bottom electrode yields a similarly short RC time constant.

In addition to estimating the RC time constant, we measured the current response of a device of type L50H1 filled with only supporting electrolyte to the potential steps applied as in Figure A.3 a. Keeping the potential of bottom electrode at 0 V, without any redox species present in the nanochannel, positive or negative current spikes were observed at the top electrode when its potential was stepped upward or downward, respectively. The transients lasted $\sim$0.2 s, significantly shorter than those observed in the experiments with redox molecules. This shows that the slow response in the latter experiments was not caused by charging effects. To understand the difference between the observed response

and the numerical estimate of the RC time given above, note that besides RC charging, dielectric relaxation of the passivation material $(SiO_2/SiN/SiO_2)^{2-4}$ also contributes to (and in fact dominates) the measured current.

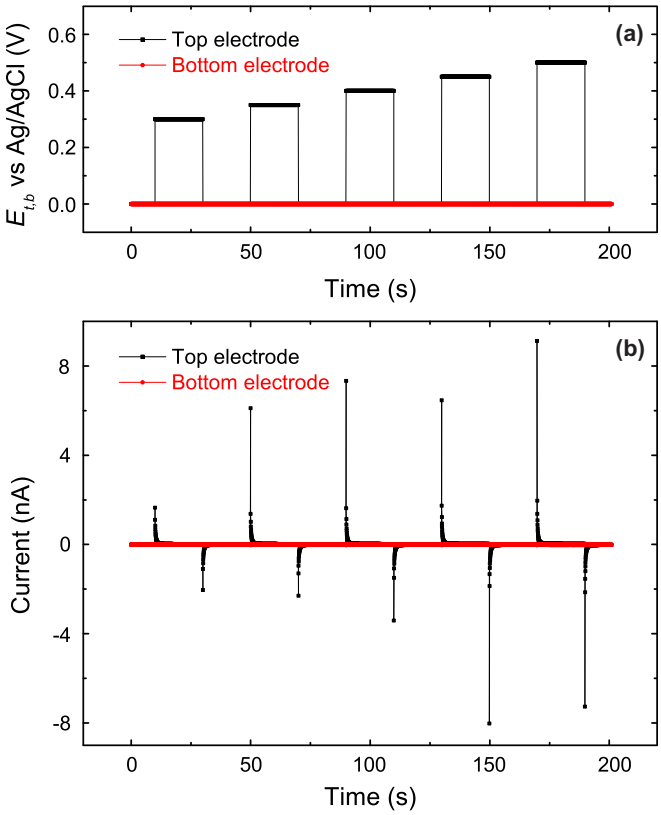

Figure A.3: Transient response of a device of type L50H1 filled with only supporting electrolyte of 1 M KCl. (a) Potentials applied as a function of time to the top (black) and bottom (red) electrode. (b) Corresponding current-time responses.

A.3 Determination of the transient response

We obtained the expression for the transient response of the current, Equation 4.3, as a purely phenomenological fit to the numerically determined diffusion of molecules into the channel. The one-dimensional diffusion equation,

$$\frac{\partial c(x,t)}{\partial t} = D\frac{\partial^2 c(x,t)}{\partial x^2} \tag{A.1}$$

was solved numerically along the length L of a nanochannel using the following initial and boundary conditions: Initially, no redox active molecules are present in the channel. Hence, the starting condition for $t = 0$ is

$$c(x, 0) = 0 \quad \text{for} \quad 0 < x < L \tag{A.2}$$

The bulk concentration at the edge of the nanochannel that is connected to the reservoir is kept constant at c_b for all times t:

$$c(x = 0, t) = c(x = L, t) = c_b \tag{A.3}$$

For $t > 0$, molecules start to diffuse into the nanochannel from both ends until the concentration equilibrates to $c(x, t) = c_b$ at time $t \to \infty$.

The total number of molecules present in the channel was determined by integrating the numerical solution $c(x, t)$ along the channel length for all time steps t:

$$N(t) = \int_0^L c(x, t)dx \tag{A.4}$$

This numerical solution $N(t)$ was phenomenologically fitted to the analytical expression

$$N(t) = c_b L \operatorname{erf}\left(2.97\left(\frac{Dt}{L^2}\right)^{0.6}\right) \tag{A.5}$$

which does not deviate more than 3% from the numerical solution for all time t (Figure A.4).

If molecules are initially present in the nanochannel, *i.e.* $N(t = 0) \neq c_b L$, the expression for $N(t)$ is modified to

$$N(t) = N(0) + (c_b L - N(0)) \operatorname{erf}\left(2.97\left(\frac{Dt}{L^2}\right)^{0.6}\right) \tag{A.6}$$

Since the faradaic current is proportional to the concentration of molecules in the channel, the current $i(t)$ can be be expressed as

$$i(t) = i(0) + (i_{ss} - i(0)) \operatorname{erf}\left(2.97\left(\frac{Dt}{L^2}\right)^{0.6}\right) \tag{A.7}$$

where $i(0)$ is the current at $t = 0$ and i_{ss} is the steady-state current.

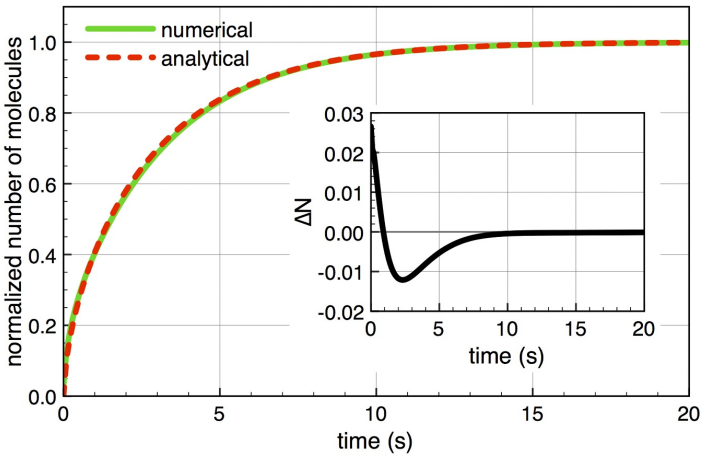

Figure A.4: Comparison of the normalized numerical solution for $N(t)$ (green line) and the analytical expression (dashed red line) for a 10 μm long device with two access holes using $D_{\text{eff}} = 8 \times 10^{-7}$ cm^2/s for both curves. Inset: Difference of the numerical solution and analytical expression.

For the case of a device with one access hole, molecules can only diffuse into the nanochannel from one end. This corresponds to starting conditions

$c(x, 0) = 0$ for $x > 0$

$c(x, 0) = c_r$ for $x \leq 0$

and the boundary conditions

$c(x{=}0, t) = c_b$

$\frac{\partial c(x=L,t)}{\partial x} = 0$

The numerical solution of the diffusion equation under these conditions is well described by

$$N(t) = c_b L \operatorname{erf}\left(2.97 \times 0.60 \left(\frac{Dt}{L^2}\right)^{0.6}\right) \tag{A.8}$$

and the solution for the diffusion with $N(0)$ molecules present in the channel at $t = 0$ is

$$N(t) = N(0) + (c_b L - N(0)) \operatorname{erf}\left(2.97 \times 0.60 \left(\frac{Dt}{L^2}\right)^{0.6}\right) \tag{A.9}$$

Correspondingly, the current is equal to

$$i(t) = i(0) + (i_{ss} - i(0)) \operatorname{erf}\left(2.97 \times 0.60 \left(\frac{Dt}{L^2}\right)^{0.6}\right) \tag{A.10}$$

A.4 Multi-potential-step chronoamperometry exhibiting opposite tendencies

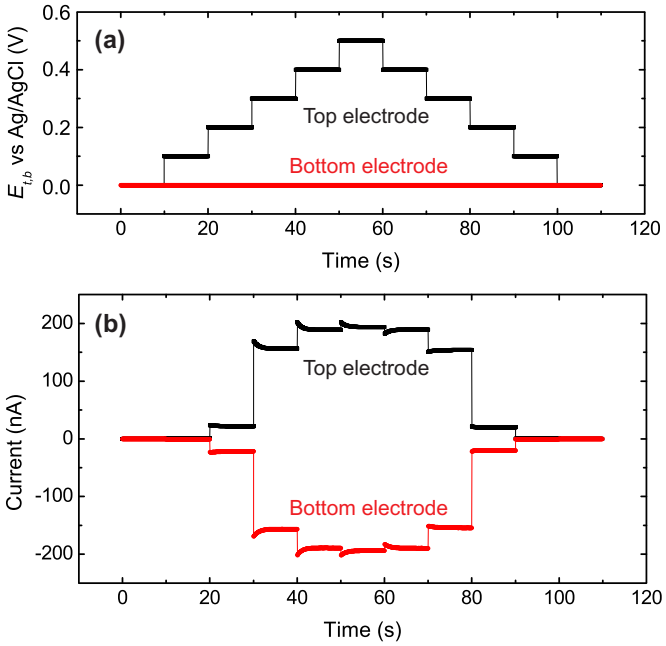

Figure A.5: Multi-potential-step chronoamperometry of a device of type L50H1 filled with an aqueous solution of 1.5 mM $Fc(MeOH)_2$ and 1 M KCl as supporting electrolyte exhibiting tendencies opposite to Figure 2 and 3. (a) Potentials applied as a function of time to the top (black) and bottom (red) electrode. (b) Corresponding current-time response.

Occasionally it was observed that a device whose Cr sacrificial layer was freshly etched exhibited opposite tendencies to those shown in Figure 4.1 and 4.3, as

shown in Figure A.5. When the potential of the oxidizing electrode was stepped up while that of the reducing electrode was maintained at 0 V, the current jumped to a value higher than i_{ss} and gradually returned to the steady-state value; the current fell below i_{ss} when the potential was stepped downwards, then increased again during the transient.

References

[1] Bard, A. J. and Faulkner, L. R., *Electrochemical Methods: Fundamentals and Applications*, Wiley: New York, **2001**.

[2] Krapf, D., Wu, M., Smeets, R. M. M., Zandbergen, H. W., Dekker, C. and Lemay, S. G., Fabrication and Characterization of Nanopore-based Electrodes with Radii Down to 2 nm, *Nano Lett.*, **2006**, *6*, 105-109.

[3] Jonscher, A. K., Universal Dielectric Response, *Nature*, **1977**, *267*, 673-679.

[4] Westerlund, S. and Ekstam, L., Capacitor Theory, *IEEE Trans. Dielectr. Insul.*, **1994**, *1*, 826-839.

Appendix B

B.1 Experimental methods

Potassium fluoride, potassium chloride, potassium bromide, potassium iodide, potassium sulfate, ferrocene carboxylic acid (FcCOOH), potassium hexacyanoferrate-III ($K_3Fe(CN)_6$), 1,1 ferrocene dimethanol ($Fc(MeOH)_2$), (ferrocenyl methyl) trimethyl ammonium iodide (FcMTMAI) and hexaammine ruthenium chloride ($Ru(NH_3)_6Cl_3$) were obtained from Sigma-Aldrich in analytical grade and used without further purification. Aqueous solutions of 1 mM $Fc(MeOH)_2$ were prepared with the above-mentioned salts as supporting electrolyte with concentration 1 M except for $K_2SO_4^{2-}$, whose concentration was only 0.68 M due to its limited solubility in water. Additionally, 1 mM solutions of all the above mentioned redox species were prepared in 1 M KCl as supporting electrolyte, except for FcCOOH whose supporting electrolyte was 200 mM PBS buffer with pH 6.5 due to solubility issues. Water was obtained from a Milli-Q Advantage ultrapure water system.

Nanogap devices were fabricated using lithographic techniques on a silicon substrate employing an approach reported previously[1, 2] except that photolithography was employed instead of electron-beam lithography. The fabricated devices contained two Pt electrodes separated by a Cr sacrificial layer. The active region of the device was defined as the volume encompassed by the overlapping top and bottom electrodes. We used two types of devices, Type 1 and Type 2, with $L_a \times w_b \times h = 100\,\mu\text{m} \times 3\ \mu\text{m} \times 130$ nm and $10\,\mu\text{m} \times 3\ \mu\text{m} \times 60$ nm, respectively. Type 1 devices were used for the transient measurements in which the potential of one of the electrodes was stepped and the corresponding current transient was monitored (Figure 5.2 a). All other measurements were performed in Type 2 devices. There were two access holes located at the top of the devices. The distance between the edge of the top electrode and the access hole was L_e=

Supporting information of Chapter 5 is included in this appendix.

2 μm except for devices used for temperature varied measurements where L_e was 1 μm. Since the top electrode was wider than the bottom electrode, there are two inactive regions of width 1 μm, symmetrically located at both sides of the active region. In all the devices, directly before the measurements, the sacrificial layer was chemically removed using a wet chromium etchant (Selectipur) from BASF, at room temperature, thus forming the nanochannel. The etching procedure was monitored electrically by measuring the resistance between the top and the bottom electrodes.

Electrochemical experiments in the nanogap devices were performed with two Keithley 6430 subfemtoamp source meters used both as voltage sources to bias the electrodes and as current meters. The Keithley instruments were controlled remotely using Labview code. All potentials were applied at the electrodes with respect a 3 M Ag/AgCl reference electrode (BASi). No auxiliary electrode was used since the current through the reference electrode was appropriately small (in the range of pA, which is three orders of magnitude smaller than the redox-cycling current).

In the redox cycling measurements the potential at the reducing electrode was 0 V (or -0.4 V for $Ru(NH_3)_6Cl_3$) while that at the oxidizing electrode was swept between 0 V and 0.6 V. Current-time traces, each of length 50 s, were recorded at different temperatures ranging from room temperature ($21 \pm 2\,^{\circ}C$) to 60 °C by heating the metal slab over which the nanogap sensor was placed using a resistive element. The temperature was measured using a Pt-100 temperature sensor. From the steady state currents ($i = 4ner_0DN_B$, where N_B is the bulk number concentration of the redox species) measured using a glassy carbon ultramicroelectrode (UME) of radius, $r_0 = 5.5\,\mu$m (BASi MF-2007) the bulk diffusion coefficient D of $Fc(MeOH)_2$ molecules in 1 M KCl was determined at different temperatures.

B.2 Cleaning the electrodes

Prior to the redox cycling measurements, the devices were cleaned by filling with a solution of 0.5 M H_2SO_4 and repeatedly (typically 2 to 3 times) sweeping the electrode potential between -0.2 V and 1.2 V *vs.* Ag/AgCl until a reproducible voltammogram was obtained. A typical cyclic voltammogram obtained in this way from a nanogap device is shown in Figure B.1. The peaks (1) to (4) are representative for Pt in contact with H_2SO_4.[3] This shows that a clean Pt surface is exposed to the solution.

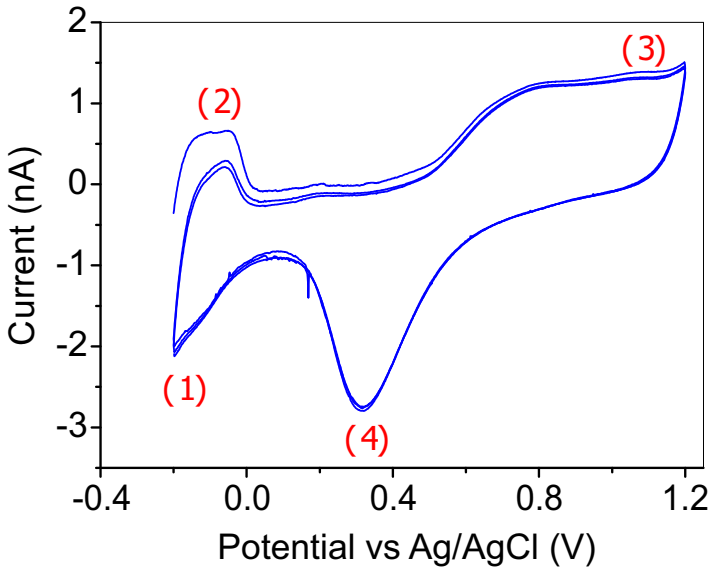

Figure B.1: Cyclic voltammogram of a platinum electrode in a nanogap sensor filled with 0.5 M of H_2SO_4. The peaks correspond to: (1) hydrogen adsorption, (2) oxidation of the adsorbed hydrogen, (3) oxidation of platinum, (4) reduction of the platinum oxide layer. The scan rate is 50 mV/s.

B.3 Quantifying adsorption

To quantify adsorption using Equation 5.2 one must determine the rms value of the fluctuations in the faradaic current, $I_{F,\mathrm{rms}}$. As plotted in Figure B.2, we determined the degree of adsorption from the values of $I_{F,\mathrm{rms}}$ obtained directly from the current-time traces (open squares) or from the PSD of the traces (open circles) as[4]

$$I_{F,\mathrm{rms}} = \sqrt{\int S(f)df} \tag{B.1}$$

The integration is performed between the minimum (20 mHz) and the maximum (25 Hz) frequencies of the measured PSDs.

As the temperature increases, the frequency spectrum shifts towards higher values and frequency fluctuations beyond 25 Hz are not captured due to the limited data acquisition rate of the instrument. Therefore, the values of $I_{F,rms}$ determined in this way from the current-time traces at high temperature are not fully accurate. This is the reason why the initial decreasing trend in the adsorption in Figure B.2 (open circles and squares) disappears and above 35 °C

the adsorption appears to increase as the temperature rises. To overcome this issue, we integrated the expression for the PSD ($S(f) = S_{0,m}/(1 + (f/f_{0,m})^{3/2})$) from $f = 0$ to $+\infty$ to include contributions from all frequencies. This results in the expression,

$$I_{F,rms} = \sqrt{2 S_{0,m}\, f_{0,m}} \tag{B.2}$$

This means that if the values of S_0 and $f_{0,m}$ are obtained from fitting the PSD, it is then possible to get the correct value of $I_{F,rms}$ using Equation B.2. In Figure B.2, the degree of adsorption obtained using Equation B.2 is plotted (open triangles). These values are very close to the ones calculated using the frequency analysis (filled stars), as embodied by Equation 5.2, both showing a decreasing adsorption with increasing temperature.

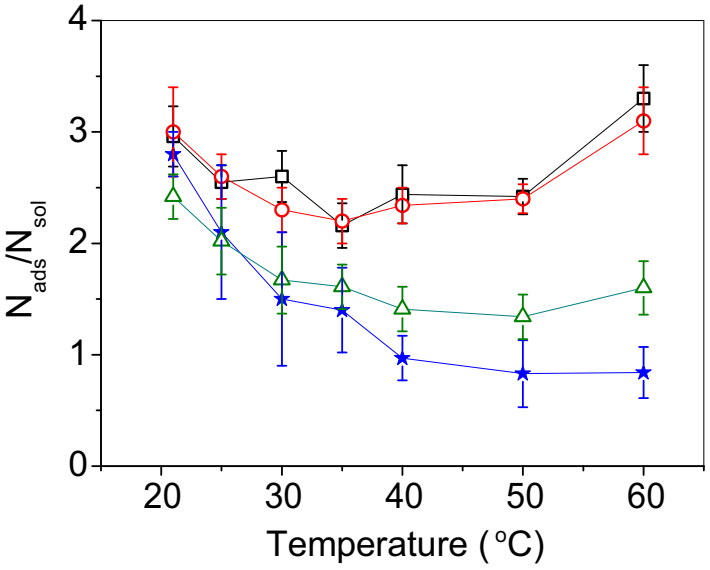

Figure B.2: Degree of adsorption versus temperature obtained from the rms noise analysis using Equation 5.2 (open symbols) and frequency analysis using Equation 5.1 (filled symbols) for 1 mM $Fc(MeOH)_2$ in 1 M KCl. In Equation 5.2, the rms value of the fluctuations in the faradaic current can be obtained directly (black open squares) from the current-time traces or by integrating the PSD (red open circles) of the traces. As the temperature increases the frequency spectrum of the fluctuations goes beyond the detection bandwidth of the measurement device which brings inaccurate values of $I_{F,\mathrm{rms}}$ and adsorption. Integrating the PSD with frequencies ranging from 0 to ∞, however, gives correct values of $I_{F,\mathrm{rms}}$ and adsorption (green open triangles).

Figure B.2 indicates that determining adsorption using $I_{F,\mathrm{rms}}$ obtained directly from the current-time traces does not give correct values if a significant portion of the spectra is not included due to instrumental averaging. This becomes sig-

nificant as $f_{0,m}$ approaches the measurement bandwidth at higher temperatures. However, at room temperature and when adsorption is large, this procedure is accurate and generates adsorption values similar to the ones obtained using Equation 5.1.[5] In all the measurements at room temperature (with devices having L_e= 2 μm) we determined the degree of adsorption using Equation 5.2, with $I_{F,\mathrm{rms}}$ directly obtained from the current-time traces.

B.4 Effect of the inactive region

The devices have two inactive region each of width 1 μm, symmetrically placed at each side of the active region due to the fact that the top electrode is broader than the bottom one. No redox cycling takes place in the inactive region as there is only one electrode (top) present. The transverse diffusion of molecules between the active and inactive regions causes high frequency fluctuations in the redox-cycling current. A detailed analytical derivation of the expressions to calculate the maximum power S_0 and cross-over frequency f_0 of these transverse and longitudinal fluctuations can be found in ref.[2] These values depend on the device geometry through the parameters L_e and L_a as,

$$S_0 = \frac{N i_p^2}{3D}(L_a^2 + 6L_e L_a) \tag{B.3}$$

$$f_0 = \frac{D}{\pi}\left(\frac{3}{L_a^2(L_a + 6L_e)}\right)^{2/3} \tag{B.4}$$

where N is the average number of molecules present in the active region, D is the diffusion coefficient, and i_p is the current per molecule.[2] In the transverse case, taking $L_e = 1$ μm (width of the inactive region) and $L_a = 3$ μm (in this case, the width of the bottom electrode) we obtain S_0 is at least 100 times smaller than that of the longitudinal fluctuations taking $L_e = 1$ μm (the length of the access channel) and $L_a = 10$ μm (the length of the active region). Similarly, the cross-over frequency f_0 is 36 times larger than that of the longitudinal fluctuations. Therefore, since the longitudinal fluctuations mask the transverse fluctuations, to simplify our analysis we neglected any correction due to the inactive regions.

B.5 Temperature and limiting current

The diffusion-limited current in redox cycling is given by

$$I_F = \frac{neADcN_A}{h} \tag{B.5}$$

where n is the number of electrons transferred, $-e$ is the electron charge, A is the active area, N_A is the Avagadro constant, c is the molar concentration of the molecules and h is the distance between the top and bottom electrodes. Increasing the temperature also increases the diffusion-limited faradaic current, as shown in Figure B.3, because the value of the diffusion coefficient increases with temperature.

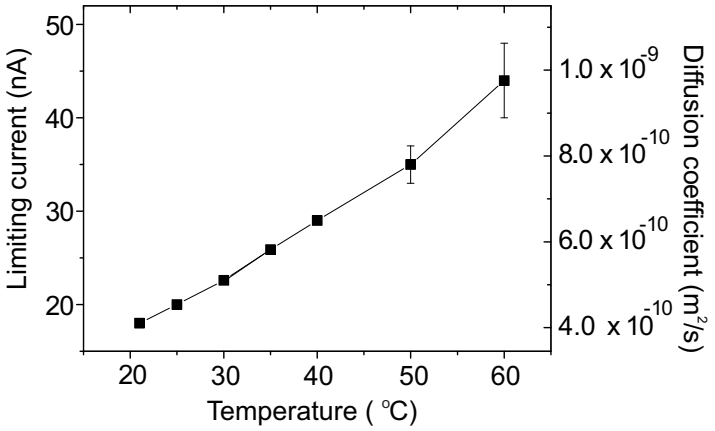

Figure B.3: The diffusion limited steady state current for 1 mM $Fc(MeOH)_2$ in 1 M KCl. The steady state current is directly proportional to the diffusion coefficient and increases with increasing temperature. The error bars are the standard deviations from five consecutive measurements.

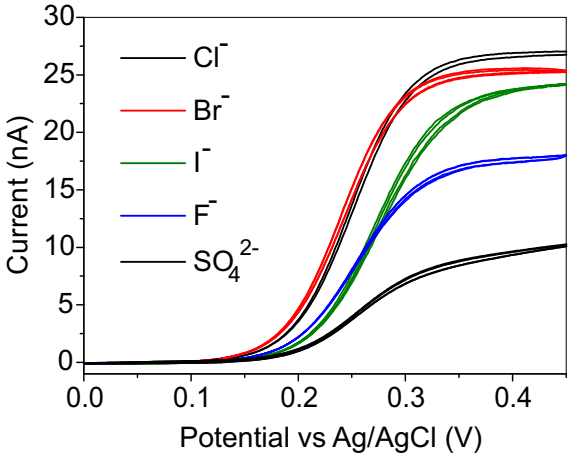

Figure B.4: Cyclic voltammogram of 1 mM, $Fc(MeOH)_2$ with 1 M concentration of supporting electrolyte with different anions (shown in the figure). With SO_4^{2-} the reaction kinetics are found to be significantly slowed.

B.6 Cyclic voltammogram of $Fc(MeOH)_2$ and anions

We measured the redox-cycling current of $Fc(MeOH)_2$ while scanning the potential at the oxidizing electrode between 0 and 0.45 V. The experiments were performed with different anionic species in the supporting electrolyte and K^+ as cation. The results are shown in Figure B.4. With anions, F^- and SO_4^{2-}, the limiting current was considerably lower than the expected diffusion-limited value, obtained with Cl^-. The voltammogram for SO_4^{2-} further exhibits slow reaction kinetics. The half-wave potential (0.25 V) also changes for different anions.

References

[1] Zevenbergen, M. A. G., Krapf, D., Zuiddam, M. R. and Lemay, S. G., Mesoscopic Concentration Fluctuations in a Fluidic Nanocavity Detected by Redox Cycling, *Nano Lett.*, **2007**, *7*, 384-388.

[2] Zevenbergen, M. A. G., Singh, P. S., Goluch, E. D., Wolfrum, B. L. and Lemay, S. G., Electrochemical Correlation Spectroscopy in Nanofluidic Cavities, *Anal. Chem.*, **2009**, *81*, 8203-8212.

[3] Bard, A. j. and Faulkner, L. R., *Electrochemical Methods: Fundamentals and Applications*, John Wiley & Sons: New York, **2001**.

[4] Stremler F. G., *Introduction to Communication Systems, 3rd ed.*, Addison-Wesley Publishing Company, **1990**, pp. 168-171.

[5] Singh, P. S., Chan, H. S. M., Kang, S. and Lemay, S. G., Stochastic Amperometric Fluctuations as A Probe for Dynamic Adsorption in Nanofluidic Electrochemical Systems, *J. Am. Chem. Soc.*, **2011**, *133*, 18289 -18295.

Appendix C

C.1 Methods

C.1.1 Fabrication of nanogap devices

The complete process flow is shown in Figure 6.2 b. In step 1, a stack of metal film layers consisting of 15 nm/50 nm/40 nm/50 nm/10 nm Ti/Pt/Cr/Pt/Ti was defined on a 4-inch Si wafer with 500 nm thermally grown SiO_2. The metal layers were deposited consecutively by electron-beam evaporation without breaking vacuum and patterned using a lift-off process based on a positive photoresist (OIR 907-17, Arch Chemicals).

Afterwards, a layer of 210 nm of PECVD SiO_2 was deposited and patterned (step 2) in a RIE etcher to function as the mask for the following IBE step. IBE was chosen to etch through the Pt top electrode and Cr sacrificial layer and thus define the active region of the device (step 3). This was because it was found that the etching speed of Cr by wet etching was too fast to control[1] and that RIE deposited contaminants at the edges of the pattern which were difficult to remove. SiO_2 was used as mask instead of photoresist because the photoresist was hardened during IBE and difficult to remove afterwards. The IBE was done with an Oxford i300 system which has a secondary ion mass spectrometry (SIMS) endpoint detector integrated in the chamber. Etching was terminated 20 s after a rising signal of Pt was observed in SIMS to guarantee that all the Cr in the trench had been removed. During IBE the wafer was tilted with an ion beam incident angle of 70° and rotated with a speed of 5 rpm. Nonetheless, re-deposition[2–4] of some of the etched Cr and Pt was inevitable, resulting in an electrical connection between the two electrodes. The wafer was therefore immediately dipped into 5% HF for 10 s (to remove a passivation layer,[5, 6] see C.4) and immersed

Supporting information of Chapter 6 is included in this appendix.

into freshly prepared aqua regia solution (37% HCl : 70% HNO3 : H_2O 3 : 1 : 2, no external heating) for 5 min to remove the Pt re-deposited during IBE.

Subsequently, a passivation layer of 210 nm PECVD SiN was deposited (step 4) to cover all the metal layers. In the next two steps, a contact wire was deposited to provide a connection between the top electrode and its leading wire by first etching through the SiN plus SiO_2 using RIE so as to open a contact window (step 5) and then lifting off the sputtered 10 nm/340 nm/10 nm Ti/Pt/Ti (step 6) with the same photoresist as used in step 1. A final passivation layer consisting of 108 nm/528 nm/108 nm PECVD SiO_2 / SiN/ SiO_2 was deposited (step 7) to protect the device from being exposed to the liquid. Finally entrance holes were generated by RIE through the passivation layer followed by IBE through the top Pt layer (step 8). A second 10 s 5% HF dip plus aqua regia treatment of 8 minutes was carried out to remove any redeposition. Immediately before electrochemical measurements, the Cr layer was etched by immersing the device in Chromium Etch Selectipur (BASF), creating a nanochannel (step 9).

After releasing the nanochannel but before measurements, the devices were placed in a sonication bath and vortex to increase their robustness, since 40 nm long hanging beams of TiO_2 were generated around the access holes in step 8, causing failures in some devices. By this method, the yield of the devices was 50%. More detailed explanations and information are provided in C.5.

The devices used for the experiments had a channel dimension of 50 μm × 5 μm × 40 nm, with 4 × 2 μm^2 access holes at each end.

C.1.2 Electrical measurements

The currents were measured with two FEMTO DDPCA-300 variable-gain sub-femto-ampere amplifiers that were controlled with in-house LabVIEW software. The trans-impedance gain was 10^{12} V/A and oversampling with a sampling frequency of 10 kHz and averaging interval of 50 ms was employed. In the absence of redox molecules, the current traces exhibited random noise with amplitude 3 - 5 fA rms. A standard Ag/AgCl electrode (3 M NaCl, BASi) served both as reference and counter electrode. This configuration is appropriate since the current flowing through the reference electrode is negligibly small. The reference electrode was immersed in a PDMS reservoir with an opening at the bottom that contacted the device. All the potentials mentioned in the manuscript are referenced to Ag/AgCl. The device was placed on a vibration isolation table inside a Faraday cage to shield vibration and interfering electrical signals. For the high-temperature measurements, the chip was placed on a copper block that was heated by passing a current generated by a TTi PL303-P power supply through a 20 Ω 50 W resistor glued onto the block. The temperature was monitored with a K-type (Chromel-Alumel) thermocouple reader (206-3738, RS components).

The diffusion coefficients of the analyte molecules were determined from the diffusion-limited current at a 5 μm radius platinum ultramicroelectrode (BASi MF-2005).

C.1.3 Chemicals

(Ferrocenylmethyl)trimethylammonium bromide (FcTMABr) was purchased from ABCR GmbH (cat. no. AB145893), potassium ferricyanide ($K_3Fe(CN)_6$) from Sigma-Aldrich (cat. no. 702587), ferrocenedimethanol ($Fc(MeOH)_2$) from Acros (cat. no. 382550010), potassium chloride (KCl) from Sigma-Aldrich (cat. no. P3911) and Selectipur chromium etchant from BASF. All chemicals were used as received and the solutions were prepared using 18.2 MΩ cm MilliQ water.

C.2 Reduction of single-molecule current due to dead volume and origin of χ_{geom}

We argued in the main text that the observed single-molecule current, i_p, is suppressed by a factor χ_{geom} due to the existence of a dead volume. Here we explain in more detail the origin of this suppression.

First consider a particular random-walk trajectory of a molecule in a device with no dead volume, as sketched in Figure C.1 a. The occupancy of the device increases from 0 to 1 when the molecule enters the active region and returns to 0 when it exits, as sketched in Figure C.1 b. The corresponding measured redox-cycling current exhibits a similar time evolution, except that, due to the finite response speed of the current measurement circuit, finite rise and fall times are observed. Such limited time resolution is unavoidable: the inverse relationship between the gain and measurement bandwidth of current-detection circuitry ensures that the more sensitive a measurement system, the lower its time resolution. In particular, the rise time of the transconductance amplifiers employed in this work is 350 ms for the 10^{12} V/A gain required for measuring single-molecule signals; only events lasting longer than this can be resolved.

Now consider the same trajectory in a device with a dead volume along both lateral edges of the device, as shown in figure C.1 d. Each time that the molecule enters the dead volume the occupancy of the active region drops to 0, leading to rapid consecutive oscillations as the molecule travels along the channel (Figure C.1 e). If the dead volume is sufficiently narrow, however, these random excursions into the dead volume are short-lived compared to the rise time of the electronics. Consequently, the extra fluctuations cannot be resolved and are instead averaged over, as sketched in Figure C.1 f. Because the total amount of charge transferred per unit time is lowered, however, the fluctuations still result in a decrease in

the average detected current. This can be put on a more quantitative footing by noting that the residence time in the dead volume is of order $(\Delta x)^2/D$, where Δx is the width of the dead volume. This corresponds to $\sim$1 ms for $\Delta x = 1\,\mu$m and decreases rapidly with decreasing dead volume, the typical residence time being thus orders of magnitude shorter than the time resolution for all values of Δx investigated here.

The arguments above are addressed formally in the supporting information of Ref. [23], where it is shown analytically that the fluctuations associated with a random process much more rapid than the longitudinal diffusion time scale have negligible effect on the noise spectral density of the redox-cycling signal but do reduce the current per molecule.

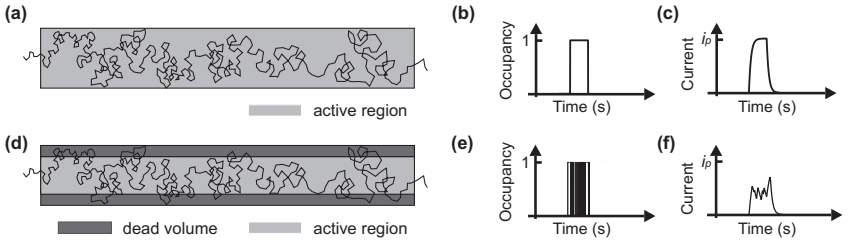

Figure C.1: (a,d) Sketch of a trajectory of the random walk of a molecule in the plane parallel to the electrode plates in a device without and with dead volume, respectively. (b, e) Simulated occupancy-time traces corresponding to situation (a) and (d). (c, f) Corresponding current-time plot after convolving the trace in (b) and (e) with a model impulse response with a time constant τ equal to the rise time of the electronics.

C.3 Stress-balanced passivation layer and AFM measurement of the morphology of the device

The complete passivation layer consisted of a $SiO_2/SiN/SiO_2/SiN/SiO_2$ stack with thickness 60/210/108/528/38 nm; the bottom and top SiO_2, which were originally 210 nm and 108 nm as deposited, were later consumed during the IBE (10 nm/min) and 5% HF dip (4 nm/s). A combination of PECVD oxide and nitride was employed because a layer with tensile stress was required to prevent film bending[7] and, based on previous reports, multiplex layers exhibit superior insulation compared to monolayers of pure silicon nitride and silicon dioxide.[8, 9]

A device with the nanochannel released was placed in an atomic force microscope (AFM, Cypher, Asylum Research) liquid cell that was filled with 1 mM $Fc(MeOH)_2$ in 0.1 M KCl and the morphology was measured in solution in contact mode. The height image and 3D image are shown in Figure C.2 a and C.2 b, respectively, which show that the top electrode membrane remained flat.

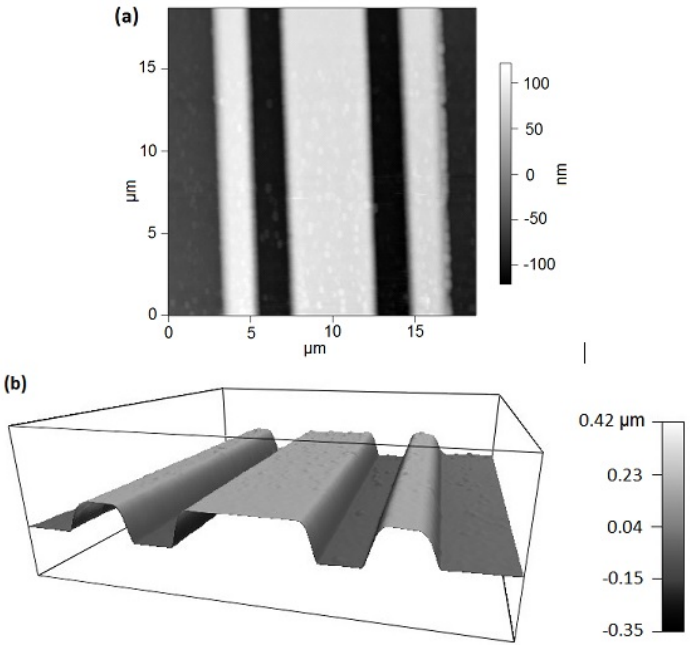

Figure C.2: AFM images of the detection region of a device. (a) Height image. (b) 3D image.

C.4 Redeposition in IBE, HF pre-treatment and etching with aqua regia

To determine the etching rate in aqua regia (37% HCl : 70% HNO_3 : H_2O 3 : 1 : 2, no external heating) of the metals, a test wafer was fabricated following the same method as described in the manuscript up to step 3, etching through the top Pt and Cr with IBE. Afterwards, the wafer was broken into pieces, three of which were processed further, one without any pre-treatment, one dipped in 1% HF for 10 seconds and the other in 5% HF for 10 seconds. All three were then immersed into freshly mixed aqua regia solution for 10 min. Finally, each chip was cleaved along the direction perpendicular to the side wall of the pattern and cross sections were observed with SEM.

Figure C.3 a shows the SEM image of a chip that was not treated with HF. Pt is not etched at all in aqua regia and a re-deposited film is visible along the side wall. Figures C.3 b and C.3 c show two different locations on a chip that was dipped in 1% HF before the aqua regia etch; in both figures, the bottom Pt is not etched, however, the top Pt is etched laterally with a different etching rate in the two cases. This shows that the passivation layer[5, 6] formed in the trench

that stopped the etching of Pt in aqua regia was not effectively removed; the top Pt electrode was etched when aqua regia went through the rift of the re-deposited film along the side wall, and the etching process thus depended on how much the side wall was sealed by the redeposition. Since it is thicker in Figure C.3 b than in Figure C.3 c, the lateral etching of the top Pt was more hindered in the former case than in the latter one.

Figure C.3 d shows a chip that was pre-treated with 5% HF and in which the SiO_2 mask layer was much thinner; as a result the bottom Pt in the trench was totally etched in aqua regia and an undercut of ∼100 nm was created, while the top Pt was etched in the lateral direction for ∼200 nm. This indicates that the passivation layer was removed by the HF, allowing the Pt to be effectively etched in aqua regia. The redeposition was completely removed in this case, as shown in the figure.

Based on the above tests, it was found that the etching rate of Pt in aqua regia was about 10 - 20 nm/min. The etching proceeded faster where there was a thinner re-deposited layer. Cr was not attacked in aqua regia, thus the sacrificial layer was wider than the two Pt electrodes and short circuits were avoided (Figure C.3 d). The etching rate of Ti in aqua regia was about 3 angstroms/min, this slow rate insured that some Ti was still remaining after the etching (as also shown in Figure C.3 d) and the electrical connection to the bottom electrode was not lost.

In the discussion section, Figure 6.3 d and 6.3 e show two devices resulted in different geometries by tuning the durations of the IBE and aqua regia etches. The device shown in Figure 6.3 d was fabricated by switching off the IBE as soon as Pt was detected in SIMS, at which point some Cr still remained and hindered the following etching of the Pt beneath. With 20 min etch in aqua regia, the bottom Pt in the trench was still present, and a ∼200 nm undercut was formed in the top electrode only. In Figure 6.3 e, an over-etching of 20 s was instead employed in the IBE step, etching away all the Cr in the trench; following 5 min immersion in aqua regia, the bottom electrode was etched through and a further lateral etch proceeded for ∼50 nm, while the top electrode was etched laterally for ∼80 nm. This represents a good compromise between minimizing the dead volume and, simultaneously, the risk of short circuits.

In the discussion section, Figure 6.3 d and 6.3 e show two devices resulted in different geometries by tuning the durations of the IBE and aqua regia etches. The device shown in Figure 6.3 d was fabricated by switching off the IBE as soon as Pt was detected in SIMS, at which point some Cr still remained and hindered the following etching of the Pt beneath. With 20 min etch in aqua regia, the bottom Pt in the trench was still present, and a ∼200 nm undercut was formed in the top electrode only. In Figure 6.3 e, an over-etching of 20 s was instead employed in the IBE step, etching away all the Cr in the trench; following 5 min immersion in aqua regia, the bottom electrode was etched through and a further lateral etch proceeded for ∼50 nm, while the top electrode was etched laterally

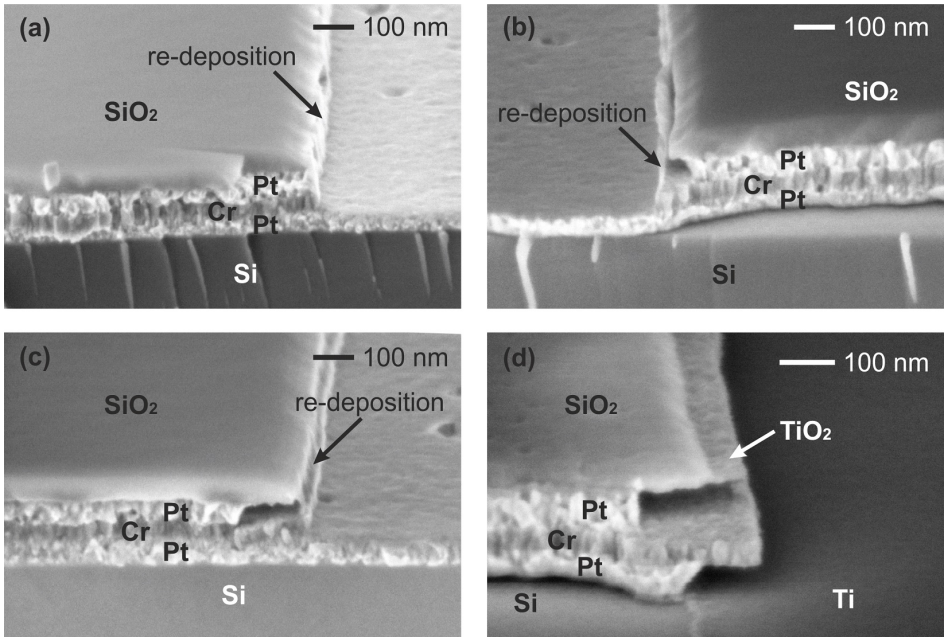

Figure C.3: Scanning electron microscopy images of cross-sections of test structures immersed for 10 min in aqua regia with (a) no pre-treatment, (b) and (c) 10 s in 1% HF as pre-treatment and (d) 10 s in 5% HF.

for ∼80 nm. This represents a good compromise between minimizing the dead volume and, simultaneously, the risk of short circuits.

C.5 Hanging beams around the access holes

In Figure C.3 d, there is a ∼40 nm wide strip hanging at the edge of the remaining SiO_2 mask. This was generated when the Ti adhesion layer of the top Pt electrode was oxidised and became resistant to the etching chemicals. Once the SiO_2 above was etched in 5% HF and the Pt beneath was etched in aqua regia, a hanging beam was formed which was merged with the passivation layer deposited in the following step, causing no risk for later steps. However, beams were also created around the access holes and kept hanging after the 5% HF treatment and aqua regia etching in process step 8. Figure C.4 a and C.4 b show the SEM images of access holes of two devices after the nanochannels have been released. In Figure C.4 a, part of the hanging beam was broken off and flushed away, as indicated by the arrow; this did not influence the functioning of the device. However, if part of the beam collapsed and touched the bottom electrode, a conduction path

was formed, as indicated by the arrow in Figure C.4 b, which caused the failure of the device. Based on a large number of experiments, it was found that the beams could be broken off and the residue flushed away, greatly increasing the robustness of the devices. This was achieved by applying 15min sonication to the chip (Branson DTH-1510, 42 kHz, 80 W) and subsequently placing the chip in a vortex generated by a magnetic stirrer rotated with a speed of 1600 rpm in a beaker of water. Yields of 50% were achieved with this additional handling. In the future, the formation of hanging beams can be avoided by changing the material used for the IBE mask.

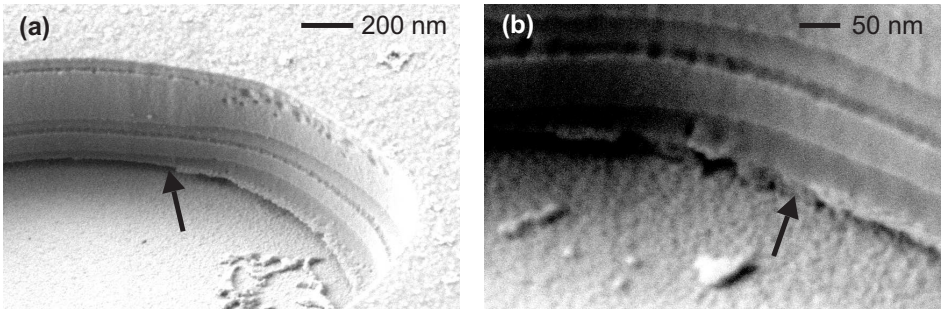

Figure C.4: Scanning electron microscope images of hanging beams around the access holes. (a) A working device in which part of the hanging beam has been broken off and flushed away. (b) Part of the hanging beam collapses and touches the bottom electrode, forming a conducting path between the top and bottom electrode and causing a short circuit of the device.

C.6 Single-molecule detection control experiments

We interpret the anti-correlated step-like features excursed from the baseline as the signature of single molecules entering the nanogap, as further supported by the following control experiments:

- Measurement at redox cycling conditions with and without redox species. Figure C.5 a and C.5 b show traces obtained from a device biased at E_t = 0.48 V and E_b = 0.32 V in 0.1 M KCl and 10 pM FcTMABr in 0.1 M KCl respectively. By adding FcTMABr, the anti-correlated excursions started to appear, which was not observed with only KCl in the solution. This supports the conclusion that anti-correlated events are caused by the redox molecules.

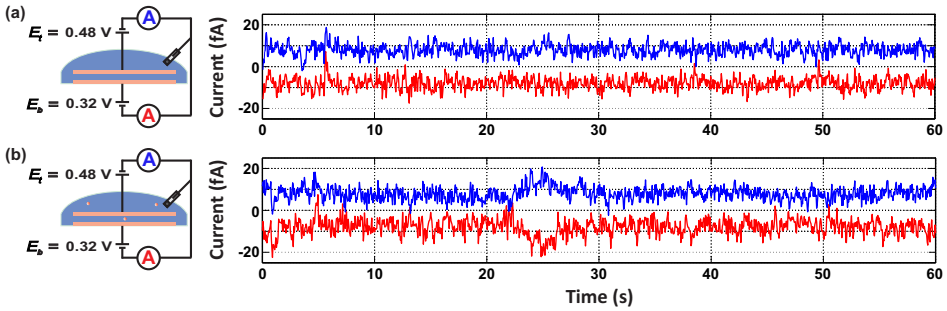

Figure C.5: Current-time traces at redox cycling conditions (E_t = 0.48 V and E_b = 0.32 V) in (a) 0.1 M KCl and (b) 10 pM FcTMABr in 0.1 M KCl.

- Measurement in redox species with and without employing redox-cycling potentials. Figure C.6 a and C.6 b show traces measured from a device filled with 10 pM $Fc(MeOH)_2$ in 0.1 M KCl with E_t = E_b = 0.1 V and E_t = 0.3 V, E_b = 0.2 V respectively. Anti-correlated steps arose only when potentials suitable for redox cycling were applied.

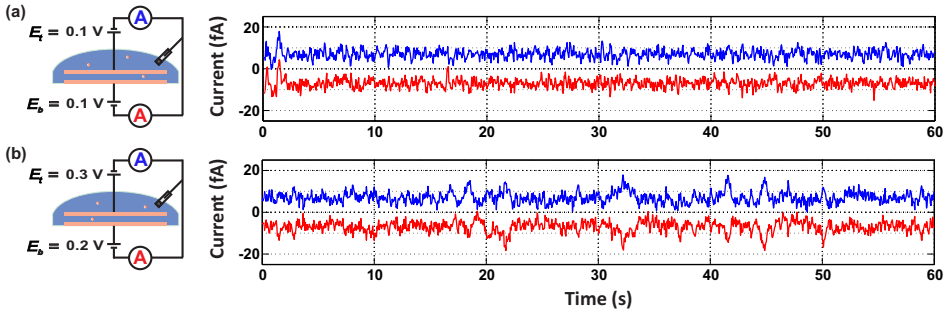

Figure C.6: Current-time traces measured with 10 pM $Fc(MeOH)_2$ in 0.1 M KCl at (a) E_t = E_b = 0.1 V and (b) E_t = 0.3 V, E_b = 0.2 V.

- Measurements while swapping the bias potentials of the electrodes. Figure C.7 a and C.7 b show traces measured in 10 pM $Fc(MeOH)_2$ in 0.1 M KCl with E_t = 0.3 V, E_b = 0.2 V and E_t = 0.2 V, E_b = 0.3 V, respectively. The polarity of the excursions were reversed when the potentials were swapped, consistent with the reversed oxidizing/reducing role of the electrodes.

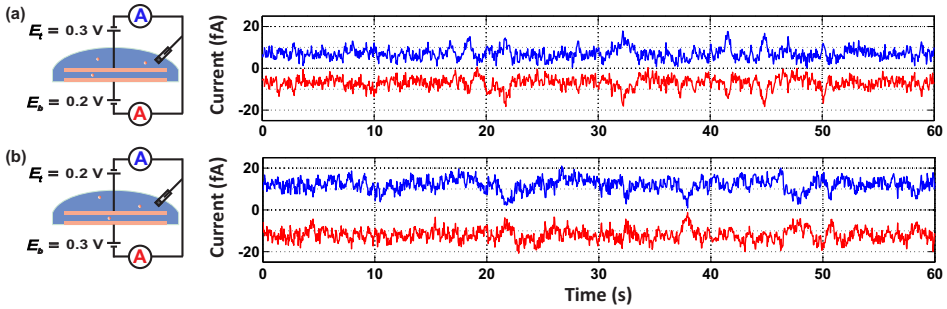

Figure C.7: Current-time traces measured with 10 pM $Fc(MeOH)_2$ in 0.1 M KCl at (a) E_t = 0.3 V and E_b = 0.2 V and (b) E_t = 0.2 V, E_b = 0.3 V.

- Measurement with shifted potential window. Figure C.8 a and C.8 b show traces measured from a device filled with 10 pM $Fc(MeOH)_2$ in 0.1 M KCl with E_t = 0.3 V, E_b = 0.2 V and E_t = 0.5 V, E_b = 0.4 V respectively. When the potential window was shifted to the non-redox cycling region, the signal disappeared.

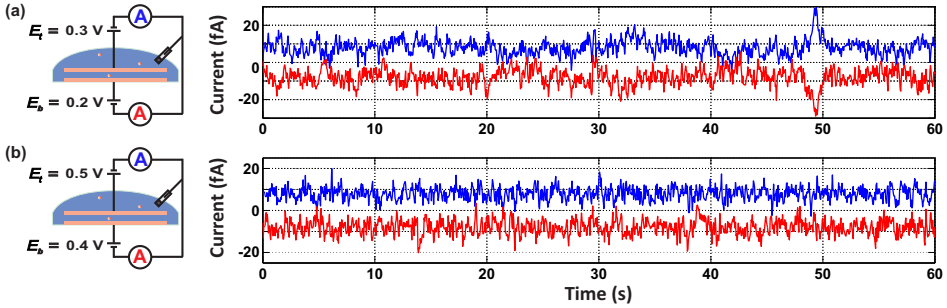

Figure C.8: Current-time traces measured with 10 pM $Fc(MeOH)_2$ in 0.1 M KCl at (a) E_t = 0.3 V and E_b = 0.2 V and (b) E_t = 0.5 V, E_b = 0. 4 V.

- Cross-correlation analysis of data obtained at different concentrations of $Fc(MeOH)_2$ in 0.1 M KCl at E_t = 0.4 V and E_b = 0.1 V. Each of the two simultaneously acquired amperometric traces consists of two components: the redox cycling current, which has the same magnitude but opposite signs at the two electrodes, and instrumental noise, which is independent for the two electrodes. This allows performance of a cross-correlation analysis[10] to extract the amplitude of the faradaic fluctuations. Figure C.9 shows the uncorrelated and anti-correlated parts of the fluctuations in the current versus concentration of $Fc(MeOH)_2$. Noise from the instrumentation is independent of the concentration of redox species, while the faradaic contribution

scales as $C^{1/2}$, supporting the conclusion that the fluctuations originate from the random walk of the molecules.[6]

At low concentration (100 pM and below), the anti-correlated component shows a higher value than predicted, indicating some contributions from contaminating background signals. At this level, it is extremely difficult to entirely remove contamination, therefore a narrower potential window of 100 - 150 mV was employed.

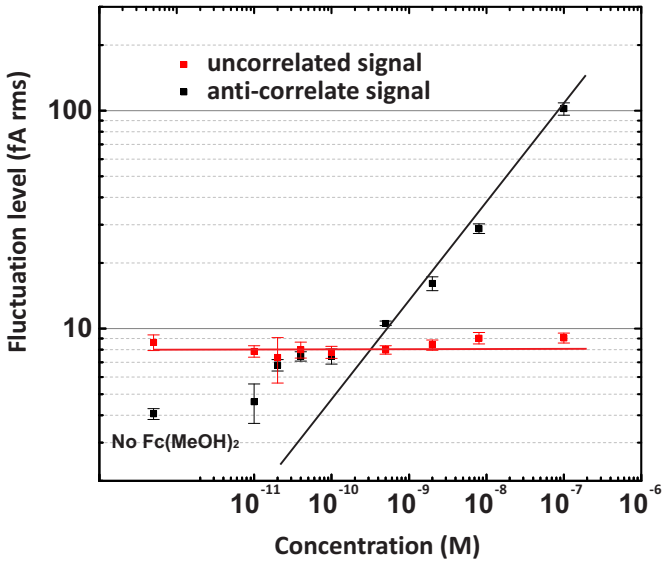

Figure C.9: Uncorrelated and anti-correlated parts of the measured fluctuations in the current versus concentration of $Fc(MeOH)_2$.

C.7 Ultra-low noise current measurements

Together with sub-femto-ampere amplifiers (FEMTO DDPCA-300), a Keithley 7078-TRX low noise triaxial cable was used. The inner shield was driven by a unity gain low impedance amplifier (guard) to reduce the cable leakage current and effective cable capacitance.[11] With probes lifted up to create an open-circuit configuration, the peak-to-peak background noise current with gain settings of 10^{12} and 10^{13} V/A was 2 fA. Part of the measurement setup, including a FEMTO amplifier, triaxial cable and probe manipulator are shown in Figure C.10.

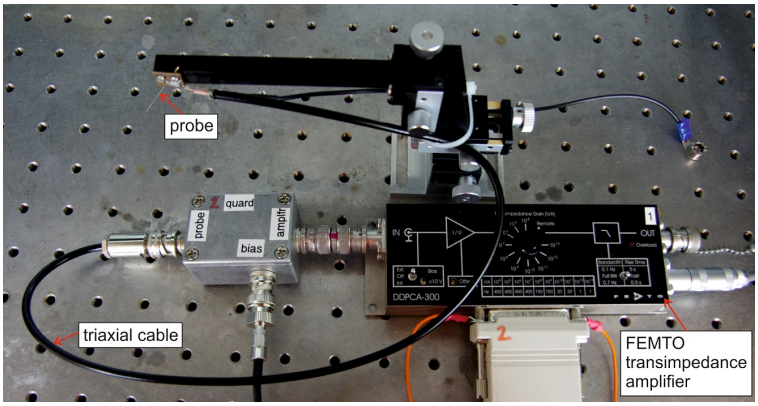

Figure C.10: Part of the measurement setup, including FEMTO amplifier, triaxial cable, probe manipulator and probe.

References

[1] Kelly, J. J. and de Minjer, C. H., An Electrochemical Study of Undercutting During Etching of Duplex Metal Films. *J. Electroche. Soc.*, **1975**, *122*, 931-936.

[2] Müller, K. P. and Pelka, J., Redeposition in Ion Milling, *Microelectron. Eng.*, **1987**, *7*, 91-101.

[3] Chapman, R. E, Redeposition: A Factor in Ion-Beam Etching Topography, *J. Mater. Sci.*, **1977**, *12*, 1125-1133.

[4] Kinoshita, K., Utsumi, H., Suemitsu, K., Hada, H. and Sugibayashi, T., Etching Magnetic Tunnel Junction with Metal Etchers, *Jpn. J. Appl. Phys.*, **2010**, *49*.

[5] Kollensperger, P. A., Karl, W. J., Ahmad, M. M., Pike, W. T. and Green, M., Patterning of Platinum (Pt) Thin Films by Chemical Wet Etching in Aqua Regia, *J. Micromech. Microeng.*, **2012**, *22*.

[6] Kim, M. J., Gruenke, L. A., Saia, R. J. and Cohen, S. S., Inhibition of Acid Etching of Pt by Pre-Exposure to Oxygen Plasma, *Appl. Phys. Lett.*, **1984**, *44*, 462-464.

[7] Schomburg, W. K.,*Introduction to microsystem design*, Springer: New York, **2011**, pp 41.

[8] Faßbender, F., Schmitt, G., Schöning, M. J., Lüth, H., Buß, G. and Schultze, J. W., Optimization of Passivation Layers for Corrosion Protection of Silicon-Based Microelectrode Arrays, *Sens. Actuators, B*, **2000**, *68*, 128-133.

[9] Schmitt, G., Schultze, J. W., Faßbender, F., Buß, G., Lüth, H. and Schöning, M. J., Passivation and Corrosion of Microelectrode Arrays, *Electrochim. Acta*, **1999**, *44*, 3865-3883.

[10] Zevenbergen, M. A. G., Singh, P. S., Goluch, E. D., Wolfrum, B. L. and Lemay, S. G., Stochastic Sensing of Single Molecules in a Nanofluidic Electrochemical Device, *Nano Lett.*, **2011**, *11*, 2881-2886.

[11] Keithley Application Note Series No. 2959.

Summary

This thesis presents results obtained during a research project aimed at realizing electrochemical single-molecule detection in water. By virtue of being inherently electrical in nature, electrochemical sensors are particularly well suited for integration with microelectronics compared to sensors based on other detection principles. They may thus enable cost effective, massively parallel analysis and diagnostics platforms. However, limited sensitivity and selectivity have been bottlenecks for years in the development of a wide range of bio-electrochemical sensors. In this project, a microfabricated nanogap device with significantly enhanced properties based on redox cycling is developed. With the ability to resolve single molecules, sensitivity is pushed to its most fundamental limit and selectivity can potentially be improved by distinguishing species *via* their single-molecule signatures.

In the opening part of the thesis, the development of microfabricated electrochemical systems is reviewed in order of increasing device complexity. Methods to fabricate micro/nanoelectrode and arrays, redox-cycling devices and compact systems integrated with microfluidics and CMOS electronics are introduced. Thanks to lithography-based technologies, not only arrays of sensing elements can be fabricated with high control and reproducibility, but also it is feasible to integrate multiple components with functions such as sensing, fluidic handling and signal processing onto a single chip.

The thesis then goes on to describe how optical lithography and standard microfabrication techniques were employed to fabricate nanogaps, which consist of two electrodes with a length in the range of 10 to 100 μm and a width of several microns embedded in the ceiling and floor of a nanofluidic channel with a height of $\sim$50 nm. Redox molecules enter the detection region defined by the two electrodes through entrance holes located at the two ends of the channel. With the electrodes biased at high over-potentials, the molecules are oxidized and reduced

repeatedly, generating an amplified current. Preliminary work to characterize and understand the behavior of the device, including how redox couples with different diffusion coefficients and reversible adsorption of analyte species influence its performance, are presented in Chapter 3-5. Small outer-sphere redox molecules such as ferrocene derivatives were found to adsorb reversibly to electrodes, especially in miniaturized systems with high surface-to-volume ratios. It was concluded that some device properties were dominated by adsorption, in particular sensor response times and single-molecule signal levels. In Chapter 5, results of more detailed investigations of adsorption with different analyte and electrolyte species at different temperatures are presented.

Based on a self-aligned fabrication scheme that minimizes the gap size and dead volume of the device, redox-cycling efficiency was further improved and electrochemical detection in aqueous solution with single-molecule resolution was achieved. This is demonstrated in Chapter 6 for three common redox mediators at physiological salt concentrations. The signal-to-noise ratio was improved by a factor of 2-3 when the temperature of the experimental system was increased from 22 °C to 37 °C as diffusion coefficient and dynamic adsorption of analyte molecules were increased and suppressed, respectively. This is the first reported electrochemical detection of single-molecules in water solution in a nanofluidic device. Further building on this approach, we also demonstrated the first study ever to characterize mass transport of individual redox molecules using an electrochemical method. Analysis of the distribution of first-passage times of single molecules suggests anomalous surface diffusion of adsorbed analyte molecules at ultra-low (10 pM) concentrations compared to measurements at high (μM to mM) concentrations.

Samenvatting

Dit proefschrift betreft onderzoek gericht op het realiseren van de elektrochemische detectie van enkele moleculen in waterige oplossingen. Vergeleken met andere detectiemethoden zijn elektrochemische sensoren inherent elektronisch van aard, en daardoor buitengewoon geschikt voor integratie met micro-elektronica. Hierdoor maken ze de ontwikkeling van kostenefficiënte, parallelle analytische en diagnostische platformen mogelijk. Echter, beperkingen in gevoeligheid en selectiviteit vormden al jaren het knelpunt in de brede ontwikkeling van bio-elektrochemische sensoren. In dit project is een verbeterd instrument met een microgefabriceerd nanokanaal ontwikkeld gebaseerd op 'redox cycling' (het herhaaldelijke oxideren en reduceren van een enkel molecuul). Dankzij de mogelijkheid om een enkel molecuul waar te nemen is de gevoeligheid gemaximaliseerd tot de fundamentele limiet. De selectiviteit kan verder worden verbeterd door verschillende soorten moleculen te onderscheiden aan de hand van het karakteristieke signaal van een enkel molecuul.

In het eerste deel van dit proefschrift is er een overzicht gegeven van microgefabriceerde elektrochemische systemen, in het volledige spectrum van ogenschijnlijk eenvoudige tot meer complexe instrumenten. Methoden voor het vervaardigen van micro- en nano-elektroden, redox cycling-instrumenten en compacte systemen met geïntegreerde microfluïdica en CMOS elektronica worden geïntroduceerd en besproken. Technieken gebaseerd op lithografische methoden maken het mogelijk om series van detectie-elementen met een hoge mate van beheersing en reproduceerbaarheid te fabriceren. Bovendien maakt deze techniek de integratie van meerdere componenten met verschillende functies zoals detectie, vloeistofmanipulatie en signaalverwerking op een enkele chip mogelijk.

Het volgende deel van dit proefschrift beschrijft hoe optische lithografie en gangbare microfabricatie technieken zijn gebruikt om nanokanalen te maken met daarin twee parallelle elektroden van 10-100 μm lang en enkele micrometers breed,

die van elkaar gescheiden zijn door een nanofluïdisch kanaal met een hoogte van ∼50 nm. Redox-actieve moleculen kunnen het detectiegebied tussen de twee elektroden binnentreden middels toegangspunten aan beide uiteindes van het kanaal. Wanneer de elektroden op een hoog overpotentiaal gehouden worden, worden de redox-actieve moleculen herhaaldelijk geoxideerd en gereduceerd, wat leidt tot een versterkte elektrische stroom aan de elektroden. Inleidend werk om de instrumenten te karakteriseren en te begrijpen is beschreven in Hoofstukken 3-5. Hierbij is onder meer gekeken naar redoxkoppels met verschillende diffussiecoefficiënten en naar de rol van omkeerbare adsorptie van het analiet. Voor kleine redox-actieve moleculen zoals ferroceen-derivaten is adsorptie aan elektroden omkeerbaar, vooral in geminiaturiseerde systemen met een hoge oppervlakte/volume verhouding. Er is geconcludeerd dat sommige systeemeigenschappen, zoals de detectietijd en de grootte van het signaal afkomstig van een enkel molecuul, in zeer grote mate bepaald wordt door adsorptie. De resultaten van een gedetailleerd onderzoek naar de rol van adsorptie met verschillende analieten en redox-actieve moleculen bij verschillende temperaturen zijn gepresenteerd in Hoofdstuk 5.

Door gebruik te maken van een zelfuitlijnend fabricageproces met als doel de hoogte van het kanaal en het dode volume van het systeem te minimaliseren werd de redox cyclingsefficiëntie dusdanig verhoogd dat het mogelijk was om een enkel molecuul in een waterige oplossing te detecteren. Het bewijs wordt geleverd in Hoofdstuk 6, voor drie veelgebruikte redox-actieve moleculen in oplossingen met fysiologische zoutconcentraties. De signaal/ruis verhouding kon verder verbeterd worden door de temperatuur te verhogen van 22 °C naar 37 °C, omdat de verhoogde temperatuur de diffusiecoefficient laat toenemen en de dynamische adsorptie van het analiet onderdrukt. Hiermee is voor eerste keer de elektrochemische detectie van enkele moleculen in een waterige oplossing waargenomen met behulp van een nanofluïdische instrument. Deze nanokanalen hebben het verder mogelijk gemaakt om voor de eerste keer ooit het massa-transport van enkele redox-actieve moleculen te karakteriseren met elektrochemische technieken. Verdere analyse van de eerste doorkomsttijd van enkele moleculen suggereert een afwijkend diffusiemechanisme langs het oppervlak van geadsorbeerde analiet moleculen bij ultralage analiet concentraties (10 pM) ten opzichte van metingen bij hogere (μM-mM) concentraties.

Acknowledgements

Lots of times on the bike suddenly I found I was thinking about how to write the acknowledgement, I guess that is because I enjoy these four years very much.

I was involved in a research project collaborating with several universities while working in the company before conducting this study, from which I saw the fun of working on this type of project and got to know Henri, a cheerful and inspiring person I had never met before. Two days after my first thought about starting a PhD study without speaking it out, Henri was asking 'when is your promotion?', ha, now I know the answer. Henri, thank you very much for guiding me returning to the university with your great kindness and sharpness, I would make this choice again. By the way, it is always great fun to go out with you and Yiping.

Before meeting Serge I was quite doubtful about myself since I was turned down in an earlier interview and also the project sounded quite theoretical for me, even though that is what I would like to learn. I was very much inspired while talking with Serge, whose eyes glow when talking about science, there is no way not to drop the doubts if being accepted. Serge, thank you very much for giving me the opportunity to step into science, I really appreciate it. You give absolute excellent scientific supervision, all the discussions, lectures, book clubs, seminars let me improved steadily. The large amount of time and effort you spend on helping students to develop the skills in writing and giving presentations are very much beneficial. On one hand I get used to default you as wikipedia, but on the other hand I keep on wondering how powerful your brain is and how can you have infinity patience and passion. You care about students and colleagues, and you are always trying to help, besides knowledge, it is very precious to learn from you the attitude to treat people and things in work and life. And of course, it is always enjoyable talking with you about whatever topics. Serge, thank you very much again for the supervision, I have learnt many precious things that will

influence me in the future. I am happy to see the brand new group now forms into a good shape and keeps growing, I wish everything goes well with the group and hope you, Claudia and little Marcel all the best.

After the first meeting with Serge I visited the group in Delft and met Marcel, Pradyumna, Bank, Edgar and Piotr, a group of enthusiastic people, I would like to thank them as the visit made me even more determined on joining the group. Marcel, it is nice to continue the project with the stairs you built up and it is great to see you talking about the project still with lots of passion after several years of your graduation.

Chief Naveen, it was great time starting up with you and together with the lab, we ordered beakers, stationeries, collected things from Delft, moved them from one temporary place to another and watched an empty space turning into a fully equipped lab. I'm glad that you found a proper project for your study, and I wish you very best luck. Chief Pradyumna, I learnt a lot about electrochemistry and experimental tips from you, and also how to use science to solve problems in life such as burnt pans and forgotten trash. I enjoy very much going out with you and Indu, it was always great fun, I wish you everything goes well in CA. Ingrid, thank you very much for the help along the years, as a foreign student, your warm heart and lovely smile made things much easier. And thanks a lot for organising the group activities, there are millions of good moments stored in the memory, especially the last Christmas dinner, very cozy, I wish you very best for the heart muscle strength training.

I learnt a lot of things while working together with Klaus and Dileep, they have endless smart and/or crazy ideas to make the experiments more exciting, and they are always ready to help PhD students with great patience. Klaus, I wish to see the world in a thousand years but I do not have the coverage to be frozen, wish you all the best for your new start in Chemnitz. Dileep, still remember you helped me to move the chips on the AFM holder with a micron-accuracy requirement? We said it has to be in the acknowledgement, and here it goes! It is difficult to see you not in peace, talking with you always make me relax and calm down. I wish you everything goes well with career and life.

Ab, thank you very much for making the magic black boxes work! Without your effort, maybe Chapter 6 and 7 would not exist in this book. And whenever going to you with questions and problems, you always give very fast and helpful response, once something in the lab goes wrong, I'm not nervous as I know Ab will manage to fix it, thank you for making the lab in a very good order. I wish Colette very best for her recovery.

At half way of the study, an Argentinian invaded the office, since then things changed a lot, magic started to take place. When experiments failed, an encouraging note or song would fly in, when good results arrived, a note with smiling face or a bar of chocolate would follow. And I do believe Santa Claus passes by

the office when someone works hard in Christmas! I appreciate very much to know this brilliant girl, always cheering, caring and looking for keys. There are endless beautiful and funny moments to recall, apple time, statistic physics time, yoga time, swimming time, movie time, beer time, hotpot time, magic cake time, story time, discussion time..... Cecilia, I enjoy very much working with you in the same office and sharing the feelings of life, it is very lucky of meeting you, learning from you and having tons of fun. I wish everything goes well with your project and all the best for you and Federico.

I was very happy to receive an AFM licence valid for 50 years from James, the chairman of nanoionics fussball organization. It is great fun to have you in meetings and discussions, in lunches, in pubs, though not living in UK, we do know lots of information about the situation there, and Shilpa, I enjoy a lot the wine night, it is very nice talking with mind opened, I wish you two good luck for the wedding and all the best in the future. Usually Jin doesn't talk much, but every time talking with him I was surprised by how much he knows about history and the society, I must say every time after these talks I learnt something new from this young guy. Jin thank you for being my paranymph and wish you good luck with the following study. Sahana, thanks a lot for organising the PhD getting together at your place, it was a nice dinner with lots of interesting topics. Stanley, thank you very much for the help with the summary, it is nice you drop by the office for coffee break, which helps a lot to refresh in the late afternoon. Natalia, you stayed in the group shortly but it was very nice meeting you, the meals we took at the Spanish Association are super. Jos and Zinaida, hope you have a good time in the group and good luck for your projects.

Thank you all again, with the group I have unforgettable scenes of bowling, skating, golfing, curling, painballing, karting, fussballing..... kept in my mind.

There were many nice discussions with the collaborators, I would like to thank Oguz and his team from Intel for exchanging ideas and helping with the trouble shootings. It is exciting to think how science could be used in industry to benefit people's life. I would like to thank MESA+ cleanroom staff with the help of device fabrication, which is a main part of this book. Hans, thanks a lot for taking good care of the machines and sorry for damaging the pocket in BAK. Mark and Henk, thanks a lot for the beautiful pictures you took which can always satisfy our curiosity. Also many thanks to the committee members for accepting the invitation and spending time on evaluating the thesis.

In these four years, the border between work and life, happiness and pain is less clear, some moments were very tough, thank godness to have the girls around to share laughter and tears together, you are treasures in my life, Jiejie, Chun, Xiaoxin, Pingping, Dizi, Juanzi, Qiezi, Ceci. Jiejie, I feel quite a pity that I did not spend enough time with you while you were in Tilburg, if time could go back, I would visit you more and plan more trips. I wish everything goes well with the baby, you and Pangduner, and looking forward very much meeting you again

soon. Chun and Xiaoxin, though you left the town when I started the PhD here, without you girls it was difficult to survive for the first couple of years, thank you very much for letting me feel settled down in Enschede. Pingping, swimming with you is really like swimming with a whale, it is great fun to go to the pool with you, very relaxing. I will remember that we survived together from an earthquake! Dizi, while you were in Enschede it was like the girls having an elder sister and all got good care of, and of course also the cats and the hamster. Juanzi and Qiezi, at my most stressed time, hanging out with you girls really helped me out, Juanzi's sofa has magic, once sitting on it, all the worries and concerns are gone. Qiezi, most of your ideas are too much crazy, but very inspiring, and one even worked. Ceci, you are not only my officemate, so I should not only thank you for protecting my little plant, but also for giving me wake up calls for early meetings. Girls, I know one day we will spread around everywhere on the earth, but I will always remember the wonderful time we spent together. Wish you all safe, healthy and happy.

I would also like to thank the friends with whom we shared nice moments in Enschede, Xiaodi, Laojin, Shuilingling, Gangtian, Wanxin, Songyue, Yifan, Lala, Lianghui, Jiwu, Chengwei, Jen-Hsuan, Wei-Shu. . . . . , having meals with you and the talks afterwards made weekend more interesting. And Joost, Yukiko, Bijoy, Giulia, Balaji, it is great pleasure to hang out with you, it is lovely the activity centre moved successfully from Enschede to Eindhoven and the getting together continues. Giulia, our trip in Santorini was really impressive, it was amazing to swim with fishes.

If we plot the overlap time of life with other people, probably the distribution has the same shape as that in Figure 7.3, only with few there is long overlap. To meet whom is random, but how long the durations are is not random, there are reasons behind it, such as binding force. Victor, chief editor, muchas gracias, if you are lost, reading Chapter 7 helps. I appreciate very much to have the chance of meeting the special you.

爸妈，谢谢你们教我善良，孝顺，宽厚，乐观，坚持。希望你们健康平安快乐。

Shuo

25 Feb. 2014

Enschede

Publications

1. **Shuo Kang**, Ab F. Nieuwenhuis, Klaus Mathwig, Dileep Mampallil, and Serge G. Lemay, Single-Molecule Electrochemistry in Nanochannels: Probing the First-Passage Time, to be submitted.

2. **Shuo Kang** and Serge G. Lemay, Microfabricated Electrochemical Systems, Chapter 16, *Nanoelectrochemistry*, Taylor & Francis. (Edited by S. Amemiya and M. V. Mirkin, to be published.)

3. Dileep Mampallil, Klaus Mathwig, **Shuo Kang** and Serge G. Lemay, Reversible Adsorption of Outer-Sphere Redox Molecules at Pt Electrodes, *J. Phys. Chem. Lett.*, 2014, 5 (3), 636–640.

4. **Shuo Kang**, Ab F. Nieuwenhuis, Klaus Mathwig, Dileep Mampallil, and Serge G. Lemay, Electrochemical Single-Molecule Detection in Aqueous Solution Using Self-Aligned Nanogap Transducers, *ACS Nano*, 2013, 7 (12), 10931–10937.

5. Dileep Mampallil, Klaus Mathwig, **Shuo Kang** and Serge G. Lemay, Redox Couples with Unequal Diffusion Coefficients: Effect on Redox Cycling, *Anal. Chem.*, 2013, 85 (12), 6053–6058.

6. Serge G. Lemay, **Shuo Kang**, Klaus Mathwig and Pradyumna S. Singh, Single-Molecule Electrochemistry: Present Status and Outlook, *Acc. Chem. Res.*, 2013, 46, 369-377.

7. Klaus Mathwig, Dileep Mampallil, **Shuo Kang** and Serge G. Lemay, Electrical Cross-Correlation Spectroscopy: Measuring Picoliter-Per-Mitue Flows in Nanochannels, *Phys. Rev. Lett.*, 2012, 109, 118302.

8. **Shuo Kang**, Klaus Mathwig and Serge G. Lemay, Response Time of Nanouidic Electrochemical Sensors, *Lab Chip*, 2012,12, 1262–1267.

9. Pradyumna S. Singh, Hui-Shan M. Chan, **Shuo Kang** and Serge G. Lemay,

Stochastic Amperometric Fluctuations as a Probe for Dynamic Adsorption in Nanofluidic Electrochemical Systems, *J. Am. Chem. Soc.*, 2011, 133, 18289-18295.